AD_____

Award Number: DAMD17-02-1-0516

TITLE: Time-Resolved Spectral Optical Breast Tomography

PRINCIPAL INVESTIGATOR: Min Xu, Ph.D.
Melvin Lax, Ph.D.

CONTRACTING ORGANIZATION: The Research Foundation of the City University of New York
New York, New York 10031

REPORT DATE: June 2003

TYPE OF REPORT: Annual Summary

PREPARED FOR: U.S. Army Medical Research and Materiel Command
Fort Detrick, Maryland 21702-5012

REPORT DOCUMENTATION PAGE

Form Approved
OMB No. 074-0188

1. AGENCY USE ONLY (Leave blank)	2. REPORT DATE	3. REPORT TYPE AND DATES COVERED
	June 2003	Annual Summary (15 May 2002 - 15 May 2003)

4. TITLE AND SUBTITLE
Time-Resolved Spectral Optical Breast Tomography

5. FUNDING NUMBERS
DAMD17-02-1-0516

6. AUTHOR(S)
Min Xu, Ph.D.
Melvin Lax, Ph.D.

7. PERFORMING ORGANIZATION NAME(S) AND ADDRESS(ES)
The Research Foundation of the City
University of New York
New York, New York 10031

E-Mail: minxu@sci.ccny.cuny.edu

8. PERFORMING ORGANIZATION REPORT NUMBER

9. SPONSORING / MONITORING AGENCY NAME(S) AND ADDRESS(ES)
U.S. Army Medical Research and Materiel Command
Fort Detrick, Maryland 21702-5012

10. SPONSORING / MONITORING AGENCY REPORT NUMBER

11. SUPPLEMENTARY NOTES
Original contains color plates: All DTIC reproductions will be in black and white.

12a. DISTRIBUTION / AVAILABILITY STATEMENT
Approved for Public Release; Distribution Unlimited

12b. DISTRIBUTION CODE

13. ABSTRACT (Maximum 200 Words)

The research carried out during the current reporting period i nvolved: (a) extending the cumulant solution of radiative transfer to planar geometries and comparing with Mont e Carlo simulations; (b) deve loping and enhancing the 3D tomographic image reconstruction algorithm by using the cumu lant transport model; (c) developing the criterion of the optimal regularization for image reconstruction dependent on the noise presented in measurements; and (d) deriving the nonlinear correction factor for optical imaging due to mu ltiple passages of an absorption inhomogeneity by a photon and providing a measure of the efficacy of linear inversion sch emes. The cumulant transport model was found to provide a more accurate model than the conventional diffusion model for image reconstruction in turbid media such as human breasts. The proper modeling of the noise and the appropriate regularization improves the quality of image reconstruction. The nonlinear effect of the multiple passages of an absorption site by a photon on optical imaging only becomes appreciable when the size of the inhomogeneity reaches about ten times of the transport mean free path or larger in human tissues. The theoretical formalism and computer algorithm for 3D tomographic image reconstr uction shows with simulated data the potential to provide fast 3D images of the scattering a nd absorption objects at various depths in turbid media.

14. SUBJECT TERMS
Medical and biological imaging; Optical mammography; Time-resolve Imaging; Image reconstruction techniques; spectroscopic imaging

15. NUMBER OF PAGES
76

16. PRICE CODE

17. SECURITY CLASSIFICATION OF REPORT	18. SECURITY CLASSIFICATION OF THIS PAGE	19. SECURITY CLASSIFICATION OF ABSTRACT	20. LIMITATION OF ABSTRACT
Unclassified	Unclassified	Unclassified	Unlimited

Table of Contents

Introduction

The "Time-resolved Spectral Optical Breast Tomography" research project aims to develop a near real-time three-dimensional (3D) spectral tomographic imaging algorithm with use of a transport model based on radiative transfer and light of multiple wavelengths. This project in the current reporting period involves the theoretical modeling of photon migration in tissue using the cumulant solution to radiative transfer and implementing an enhanced 3D tomographic image reconstruction algorithm. Significant advances in both fronts were made during the current reporting period.

Body

The tasks performed and the progress made during the current reporting period include the theoretical modeling of photon migration in tissue using the cumulant solution to radiative transfer and implementing enhanced 3D tomographic image reconstruction algorithms.

Theoretical modeling of photon migration in tissue

We extended the photon transport model for light migration in turbid media based on a cumulant approximation to radiative transfer to a bounded medium with planar geometries (Task 1.1). This extension makes the cumulant model more suitable in practical applications which always involve finite geometries. This cumulant model of photon migration was demonstrated to agree much better with the Monte Carlo simulation than the conventional diffusion approximation at early times while both approximations agree well with the Monte Carlo simulations at later times.[1]

We enhanced the 3D tomographic image reconstruction algorithms [2, 3] by using the new cumulant transport model (Task 1.2). By scanning a point source on the grids of the input plane of a slab and measuring light intensity on a detector array on the exit plane of the slab, a set of four-dimensional (4D) data is formed. A near real-time image reconstruction is obtained by performing a hybrid-dual-Fourier on the 4D data set.[4, 5, See Appendix 1 and 3] Improvement in the modeling accuracy was achieved.

To access the efficacy of a linear inversion scheme in image reconstruction of human breasts, we also studied the nonlinear effect of the multiple passages of an absorption inhomogeneity of finite size deep inside a turbid medium on optical imaging using the cumulant solution to radiative transfer (Task 1). We derived the analytical nonlinear correction factor which agrees excellently with the predictions from the Monte Carlo simulations. We concluded that the effect of the nonlinear multiple passages of an absorption site on optical imaging only becomes appreciable when the size of the inhomogeneity reaches $10l_t$ (ten times of mean free transport paths) or larger for human tissues. [6, See Appendix 4]

Implementing of the enhanced 3D tomographic image reconstruction algorithm

The non-iterative 3D tomographic reconstruction algorithm (hybrid-dual-Fourier tomography) was implemented (Task 1.2). The reconstruction uses fast Fourier transforms (FFT) and is fast. A complete reconstruction of $32 \times 32 \times 20$ voxels is within few minutes using 1GHz CPU.

We studied the relation between the appropriate regulation and the noise presented in measurement (Task 1.4). We found the regularization parameter is linked directly to the prior signal to noise ratio. We provided evidence that proper modeling of the noise and appropriate regularization improves the quality of image reconstruction.[7, See Appendix 5]

We are working on including of multiple wavelengths of probing light in our tomographic imaging algorithms.

Key Research Accomplishments

- Extended cumulant solution of radiative transfer to planar geometries making it more suitable for practical applications which involve finite boundaries.
- Developed and enhanced the 3D tomographic image reconstruction algorithm by using the cumulant transport model.
- Developed the criterion of the optimal regulati on parameter for inverse image reconstruction related to the noise presented in measurements.
- Derived the nonlinear correction factor of multiple passages of an absorption inhomogeneity by a photon for optical imaging and provided a measure of the efficacy of linear inversion schemes.

Reportable Outcomes

Journal Papers:

1. Cai, W., M. Xu, and R.R. Alfano. *Three dimensional radiative transfer tomography for turbid media*. in *IEEE JSTQE*. 2003 (to appear in press)
2. Xu, M., M. Lax, and R.R. Alfano, *Light anomalous diffraction using geometrical path statistics of rays and gaussian ray approximation.* Opt. Lett, 2003. **28**: p. 179-181.

Presentations and Proceeding Papers:

3. Xu, M., W. Cai, and R.R. Alfano, *Three dimensional Hybrid-Dual-Fourier tomography in turbid media using multiple sources and multiple detectors*, in *Third inter-institute workshops on diagnostic optical imaging and spectroscopy: the clinical adventure*. 2002: National Institute of Health, Bethesda, MD
4. Xu, M., W. Cai, and R.R. Alfano. *Nonlinear multiple passage effects on optical imaging of an absorption inhomogeneity in turbid media*. in *European Conference on Biomedical Optics: Photon migration and Diffuse-light imaging*. 2003

Manuscripts:

5. Xu, M., et al., *Prior information and noise in three-dimensional optical image reconstruction.*

Conclusions

The work carried out during the current reporting period builds on and affirms some of our earlier inferences and leads to the following conclusions. *First*, the cumulant transport model provides a more accurate model than the conventional diffusion model for the description of light propagation in turbid media such as human breasts. *Second*, the optimal regularization of image reconstruction depends on the noise presented in the measurements; proper modeli ng of the noise and appropriate regularization improves the quality of image reconstruction. *Third*, the nonlinear effect of the multiple passages of an absorption site by a photon on optical imaging only becomes appreciable when the size of the inhomogeneity reaches $10l_t$ or larger in human tissues. *Fourth*, the theoretical formalism and computer algorithm for 3D tomographic image reconstruction s hows (with simulated data) the potential to provide fast 3D images of the scattering and absorption objects at various depths in turbid media.

References

1. Xu, M., et al., *Photon migration in turbid media using a cumulant approximation to radiative transfer.* Phys. Rev. E, 2002. **65**: p. 066609.
2. Xu, M., et al., *Time sliced three dimensional inverse image reconstruction of objects in highly scattering media*, in *Optical tomography and spectroscopy of tissue III* . 1999. p. 2-4.

3. Xu, M., M. Lax, and R.R. Alfano, *Time-resolved Fourier optical diffuse tomography.* J. Opt. Soc. Am. A, 2001. **18**(7): p. 1535-1542.
4. Cai, W., M. Xu, and R.R. Alfano. *Three dimensional radiative transfer tomography for turbid media* . in *IEEE JSTQE*. 2003.
5. Xu, M., W. Cai, and R.R. Alfano, *Three dimensional Hybrid-Dual-Fourier tomography in turbid media using multiple sources and multiple detectors* , in *Third inter-institute workshops on diagnostic optical imaging and spectroscopy: the clinical adventure* . 2002: National Institute of Health, Bethesda, MD.
6. Xu, M., W. Cai, and R.R. Alfano. *Nonlinear multiple passage effects on optical imaging of an absorption inhomogeneity in turbid media* . in *European Conference on Biomedical Optics: Photon migration and Diffuse-light imaging* . 2003.
7. Xu, M., et al., *Prior information and noise in three-di mensional optical image reconstruction.* 2003.

Three dimensional radiative transfer tomography for turbid media

W. Cai , M. Xu, and R. R. Alfano

Institute for Ultrafast Spectroscopy and Lasers
New York State Center of Advanced Technology for Ultrafast Photonic Materials and Applications
Department of Physics
The City College and Graduate Center of City University of New York
New York, NY 10031

Abstract

The photon distribution, as a function of position, angle and time, is computed using the analytical cumulant solution of the Boltzmann radiative transfer equation (RTE). A linear forward model for light propagation in turbid media for three dimensional (3D) optical tomography is formed based on this solution. The model can be used with time resolved, CW, and frequency-domain measurements in parallel geometries. This cumulant forward model (CFM) is more accurate than that based on the diffusion approximation of RTE. An inverse algorithm that incorporates this CFM is developed, based on a fast 3D hybrid-dual-Fourier tomographic approach using multiple detectors and multiple sources in parallel geometries. The inverse algorithm can produce a 3D image of a turbid medium with more than 20,000 voxels in 1-2 minutes using a personal computer. A 3D image reconstructed from simulated data is presented.

Subject terms: photon migration; radiative transfer equation; forward model;
absorption and scattering; optical tomography; inverse algorithm.

Accepted by IEEE special issue JSTQE (Laser in medicine and biology) #1277

1. Introduction

Over the past decade, optical tomography has been investigated as a noninvasive imaging method that uses non-ionizing near-infrared (NIR) light to obtain images of the interior of the breast. Unlike X-ray, which is attenuated through media by ionizing the electrons at inner-orbits of atoms, NIR light uses the vibrational overtones for different molecular components in the structures of tumor. NIR light may be used to create image based on the molecular change, which may be used to improve sensitivity and specificity in the early diagnostics of breast cancer. Breast tissues scatter light strongly, and blur the direct shadow image of a tumor. A technique, known as inverse image reconstruction, has been investigated to overcome the problem of multiple scattering. Some obstacles in the development of optical tomography are inaccuracy of the commonly used diffusion forward model, and lack of a fast inverse algorithm able to realize a three dimensional (3D) image reconstruction of a breast for clinical use.

One critical issue is the forward model, which should correctly simulate photon propagation in the medium. The most commonly used forward models were built based on solution of the diffusion equation, which is the lowest approximation of the radiative transfer equation (RTE).[1-5] The forward models based on the diffusion approximation (DA) give a large error when the distance, d, between a voxel and a source is small. Furthermore, the photon distribution still maintains a strong anisotropy in a deeper region away from a source, which will be shown later in this paper. Unfortunately, contributions from near surface voxels to measured signals are often larger than contributions from the voxels deep inside the medium. Inaccuracy of DA based forward model may lead to a failure in image reconstruction, especially for small hidden objects deep inside the medium. The total weight matrix should be inverted. The large elements in the matrix, which play a more important role in inversion, are evaluated incorrectly in DA models. The shortcoming of DA is well recognized, but it is still broadly applied due to the difficulty in directly solving the radiative transfer equation. Hielscher et al [6] and Vihunen et al [7] developed numerical solutions of RTE for optical tomography.

Recently, we have developed an analytical solution of RTE, based on cumulant expansion, in an infinite uniform medium with an arbitrary phase function. [8,9] It provides an explicit analytical expression for photon distribution function $I(\mathbf{r}, \mathbf{s}, t)$, as a function of position $\mathbf{r}$, direction of light $\mathbf{s}$, and time t. The mean position and the half-width at half maximum height (HWHM) of the distribution are always exact. In this paper, the linear forward model based on the cumulant solution is described. This CFM may used with time-resolved, CW, and frequency-domain data, which are much more accurate than the DA models.

To obtain a 3D image one needs to investigate the inverse algorithms. For clinical applications, this requires an inversion technique, that is computationally fast, and stable in the presence of measurement noise. Recent algorithms to solve the inverse problem include Newton's least-square-based methods and gradient-descent methods.[1-5] These approaches use an iterative procedure, which requires a long computation time to solve a 3D inverse problem with large unknowns (the number of unknowns is the number of voxels). Furthermore, the iterative methods can not ensure that the result arrives at a "global minimum", and does not converge to a "local minimum", which is not a true image of the medium. The application of Fourier transform, which has been called "diffraction tomography", can greatly reduce computation time. Matson et al [10] and Li et al [11] have developed the diffraction optical tomographic methods to realize fast image reconstruction. However, their algorithms are limited to the use of a single light source with a 2D plane of detectors. This type of experimental setup acquires only a set of 2D data using CW or frequency-modulated light, that is not enough for a 3D image reconstruction. Recently, Schotland and Markel developed inverse inversion algorithms using diffusion tomography [12,13,14] based on the analytical form of the Green's function of frequency-domain diffusive waves, and point-like absorbers and scatterers. Data obtained by multiple sources with multiple detectors in parallel slab geometry are used in these approaches.

A fast hybrid-dual-Fourier (HDF) algorithm, which uses multiple sources and multiple detectors in parallel slab geometry, is described in this paper for reconstruction of a 3D image of an inhomogeneous medium. This approach uses a general 2D translation invariance of the Green's function in a homogeneous background slab medium, suitable for forward models based on solution of RTE, and various other forward models, in CW, frequency-domain, and time-resolved measurements. This inverse algorithm runs fast. It is shown that a 3D image of a turbid medium (for example, divided into 32x32x20=20480 voxels) can be reconstructed in 1-2 minutes using a personal computer. This algorithm can produce stable images in presence of relatively strong noises.

The forward model and the inverse algorithm discussed below can also be applied for image reconstruction in a cloudy environment for military use.

This paper is organized as follows: Section 2 presents the analytical solution of RTE, based on a cumulant expansion, in an infinite uniform medium and shows the photon distribution function computed using the cumulant analytical solution. Section 3 describes the forward models based on the analytical solution of RTE, considering the slab geometry, and a weak heterogeneity using a perturbative method. Section 4 describes the hybrid-dual-Fourier inverse algorithm for a reconstruction of a 3D image of an inhomogeneous medium. The 3D image using this algorithm is shown. A discussion is presented in Section 5.

2. Analytical cumulant solution of RTE

The photon propagation in a medium is described by the photon distribution function, $I(\mathbf{r}, \mathbf{s}, t)$, as a function of time t, position $\mathbf{r}$, and direction $\mathbf{s}$. The mathematical equation governing photon propagation is the well-known radiative transfer equation:

$$\partial I(\mathbf{r},\mathbf{s},t)/\partial t + c\mathbf{s}\cdot\nabla_{\mathbf{r}} I(\mathbf{r},\mathbf{s},t) + \mu_a(\mathbf{r})I(\mathbf{r},\mathbf{s},t) = \mu_s(\mathbf{r})\int P(\mathbf{s},\mathbf{s}',\mathbf{r})[I(\mathbf{r},\mathbf{s}',t) - I(\mathbf{r},\mathbf{s},t)]d\mathbf{s}' + \delta(\mathbf{r}-\mathbf{r}_0)\delta(\mathbf{s}-\mathbf{s}_0)\delta(t-0) \quad (1)$$

where the fundamental parameters are the scattering rate $\mu_s(\mathbf{r}) = c\rho\sigma_s$, the absorption rate $\mu_a(\mathbf{r}) = c\rho\sigma_a$, and the differential angular scattering rate $\mu_s(\mathbf{r})P(\mathbf{s}, \mathbf{s}', \mathbf{r})$, where σ_a and σ_s are the absorption and scattering cross sections respectively, ρ is density of scatterers, and c is the speed of light in the medium. In a uniform infinite medium, these parameters are position independent.

When the phase function depends only on the scattering angle, we can expand the phase function in Legendre polynomials with constant coefficients,

$$P(\mathbf{s},\mathbf{s}') = \frac{1}{4\pi}\sum_l a_l P_l[\cos(\mathbf{s}\cdot\mathbf{s}')] \quad (2)$$

Recently, we have developed a new approach to obtain an analytical solution of RTE, based on a cumulant expansion, in an infinite uniform medium, with an arbitrary phase function $P(\mathbf{s}, \mathbf{s}')$. [8,9]

We briefly review the concept of "cumulant" in a 1D case. Consider a random variable x, with a probability distribution function $f(x)$. Instead of using $f(x)$ to describe the distribution, we define the nth moment of x, $\langle x^n\rangle = \int x^n f(x)dx$, and correspondingly the nth cumulant $\langle x^n\rangle_c$ defined by $\exp(\sum_{n=1}^{\infty} \langle x^n \rangle_c (it)^n / n!) = \langle \exp(itx) \rangle = \sum_{n=0}^{\infty} \langle x^n \rangle (it)^n / n!$. The first cumulant $\langle x\rangle_c$ is the mean position of x. The second cumulant $\langle x^2\rangle_c$ represents the HWHM of the distribution. The higher cumulants are related to the detailed shape of the distribution. For example, $\langle x^3\rangle_c$ describes the skewness or asymmetry of the distribution, and $\langle x^4\rangle_c$ describes the "kurtosis" of the distribution, that is the extent to which it differs from the standard bell shape associated with the normal distribution function. The cumulants, hence, describe the distribution in an intrinsic way by subtracting off the effects of all lower order moments. In 3D case, the first cumulant has 3 components, the second cumulant has 6 components, and so on.

We derived an explicit algebraic expression of spatial cumulants at any angle and any time that is exact up to an arbitrarily high order n. [9] This means the distribution function $I(\mathbf{r}, \mathbf{s}, t)$ can be computed to any desired accuracy. At the second order, $n = 2$, an analytic, hence, useful explicit expression for distribution function $I(\mathbf{r}, \mathbf{s}, t)$ is obtained. [8] This distribution is Gaussian in position, which is accurate at later times, but only provides the exact mean position and the exact HWHM at early times. A weakness of the second order cumulant solution is that photons at the front edge of Gaussian distribution travel faster than light speed, thus violate causality, though to a much less extent than that in the diffusion approximation.

Fig.1 compares $I(\mathbf{r}, \mathbf{s}, t)$ obtained from the analytical cumulant solution and the Monte Calro simulation. In order to reduce the statistical deviation to an acceptable level, 10^9 events are counted in the Monte Carlo simulation. The figure shows that the solid curve (the 10th order cumulant solution) is located in the middle of data obtained by the Monte Carlo simulation. The solution for CW case can be obtained by an integration of $I(\mathbf{r}, \mathbf{s}, t)$ over time t. It is shown that even second order cumulant solution (the dotted curve) can provide an accurate CW solution, because this solution ensures that the mean position and the HWHM of distribution are always exact.

The plots in Fig. 1 indicates that a strong anisotropic angular distribution still exists at $z \sim 6\ l_{tr}$ (l_{tr} is the transport mean free path) from the source. The diffusion approximation is only valid when the angular distribution is nearly isotropic. The dominate s wave distribution $N(\mathbf{r}, t)/4\pi$ computed using the diffusion model (the thick dotted curve) has a large discrepancy with the Monte Carlo result.

The second order analytical cumulant solution is given by [8]

$$I(\mathbf{r},\mathbf{s},t) = \frac{F(\mathbf{s},\mathbf{s}_0,t)}{(4\pi)^{3/2}} \frac{1}{(\det B)^{1/2}} \exp\left[-\frac{1}{4}(B^{-1})_{\alpha\beta}(r-r^c)_\alpha (r-r^c)_\beta\right] \quad , \tag{3}$$

where

$$\begin{aligned} F(\mathbf{s},\mathbf{s}_0,t) &= \exp(-\mu_a t)\sum_l \frac{2l+1}{4\pi} \exp(-g_l t) P_l[\cos(\mathbf{s}\cdot\mathbf{s}_0)] \\ &= \exp(-\mu_a t)\sum_l \frac{2l+1}{4\pi} \exp(-g_l t) \sum_m Y_{lm}(\mathbf{s}) Y_{lm}^*(\mathbf{s}_0) \end{aligned} \tag{4}$$

In Eq. (4), $g_l = \mu_s[1 - a_l/(2l+1)]$, $Y_{lm}(\theta,\phi)=(-1)^m[(l-m)!/((l+m)!]^{1/2} P_l^{(m)}(\cos\theta)\exp(im\phi)$, where $P_l^{(m)}(\cos\theta)$ is the associated Legendre function, and $Y_{lm}(\mathbf{s})$ are spherical harmonics normalized to $4\pi/(2l+1)$.

In Eq. (3), the mean position of the distribution (first cumulant), when the source is located at $\mathbf{r}_0 = 0$ and the incident direction is along z, is given by:

$$r_z^c(\mathbf{s},t) = G\sum_l A_l P_l(\cos\theta)[(l+1)f(g_l - g_{l+1}) + lf(g_l - g_{l-1})] \quad , \tag{5.1}$$

$$r_x^c(\mathbf{s},t) = G\sum_l A_l P_l^{(1)}(\cos\theta)\cos\phi[f(g_l - g_{l-1}) - f(g_l - g_{l+1})] \quad , \tag{5.2}$$

where $G = c\exp(-\mu_a t)/F(\mathbf{s}, \mathbf{s}_0, t)$, $A_l = (1/4\pi)\exp(-g_l t)$, and

$$f(g) = [\exp(gt) - 1]/g \quad , \tag{6}$$

r_y^c is obtained by replacing $\cos\phi$ in Eq. (5.2) by $\sin\phi$.

The HWHM (second cumulant) is expressed as

$$B_{\alpha\beta}(\mathbf{s},t) = cG\Delta_{\alpha\beta} - r_\alpha^c r_\beta^c / 2 \ , \tag{7}$$

with

$$\Delta_{zz} = \sum_l A_l P_l(\cos\theta)\left[\frac{l(l-1)}{2l-1}E_l^{(1)} + \frac{(l+1)(l+2)}{2l+3}E_l^{(2)} + \frac{l^2}{2l-1}E_l^{(3)} + \frac{(l+1)^2}{2l+3}E_l^{(4)}\right] \ , \tag{8.1}$$

$$\Delta_{xx,yy} = \sum_l \frac{1}{2}A_l P_l(\cos\theta)\left[-\frac{l(l-1)}{2l-1}E_l^{(1)} - \frac{(l+1)(l+2)}{2l+3}E_l^{(2)} + \frac{l(l-1)}{2l-1}E_l^{(3)} + \frac{(l+1)(l+2)}{2l+3}E_l^{(4)}\right]$$

$$\pm \sum_l \frac{1}{2}A_l P_l^{(2)}(\cos\theta)\cos(2\phi)\left[\frac{1}{2l-1}E_l^{(1)} + \frac{1}{2l+3}E_l^{(2)} - \frac{1}{2l-1}E_l^{(3)} - \frac{1}{2l+3}E_l^{(4)}\right] \ , \tag{8.2}$$

where (+) corresponds to Δ_{xx} and (−) corresponds to Δ_{yy}.

$$\Delta_{xy} = \sum_l \frac{1}{2}A_l P_l^{(2)}(\cos\theta)\sin(2\phi)\left[\frac{1}{2l-1}E_l^{(1)} + \frac{1}{2l+3}E_l^{(2)} - \frac{1}{2l-1}E_l^{(3)} - \frac{1}{2l+3}E_l^{(4)}\right] , \tag{8.3}$$

$$\Delta_{xz} = \sum_l \frac{1}{2}A_l P_l^{(1)}(\cos\theta)\cos(\phi)\left[\frac{2(l-1)}{2l-1}E_l^{(1)} - \frac{2(l+2)}{2l+3}E_l^{(2)} + \frac{1}{2l-1}E_l^{(3)} + \frac{1}{2l+3}E_l^{(4)}\right] \tag{8.4}$$

Δ_{yz} is obtained by replacing cosϕ in Eq. (8.4) by sinϕ. In Eqs. (8.1- 8.4) $E_l^{(1\text{-}4)}$ are given by:

$$E_l^{(1)} = [f(g_l - g_{l-2}) - f(g_l - g_{l-1})]/(g_{l-1} - g_{l-2}) \ , \tag{9.1}$$

$$E_l^{(2)} = [f(g_l - g_{l+2}) - f(g_l - g_{l+1})]/(g_{l+1} - g_{l+2}) \ , \tag{9.2}$$

$$E_l^{(3)} = [f(g_l - g_{l-1}) - t]/(g_l - g_{l-1}) \ , \tag{9.3}$$

$$E_l^{(4)} = [f(g_l - g_{l+1}) - t]/(g_l - g_{l+1}) \ . \tag{9.4}$$

Figs. 2(a) and 2(b) show the light distribution as a function of time at different receiving angles in an infinite uniform medium, computed by the second cumulant solution, where detector is located, separately, at 5 l_{tr} (Fig. 2a) and 15 l_{tr} (Fig. 2b) from the source in the incident direction of the source. Fig. 2 shows the existence of the strong anisotropy of the light distribution at 5 l_{tr} from the source and the modest anisotropy at a distance of 15 l_{tr}. These types of distributions have been demonstrated by time-resolved experiments. [15]

One advantage of using the above analytical solution of RTE is that the distribution function can be computed very fast. The associated Legendre functions can be accurately computed using recurrence relations. It takes only a minute to compute 10^5 data of $I(\mathbf{r}, \mathbf{s}, t)$ on a personal computer.

The corresponding solution in the frequency-domain $I(\mathbf{r}, \mathbf{s}, \omega)$ can be obtained by making a Fourier transform $\int dt \exp(-i\omega t) I(\mathbf{r}, \mathbf{s}, t)$. The CW solution is obtained by taking ω= 0.

The photon density $N(\mathbf{r}, t)$ of the second cumulant solution is given by

$$N(\mathbf{r},t) = \frac{1}{(4\pi D_{zz}ct)^{1/2}} \frac{1}{4\pi D_{xx}ct} \exp\left[-\frac{(z-R_z)^2}{4D_{zz}ct}\right] \exp\left[-\frac{(x^2+y^2)}{4D_{xx}ct}\right] \exp(-\mu_a t) \ , \tag{10}$$

with the mean position $R_z = c[1-\exp(-g_1 t)]/g_1$. (11)

The corresponding time-dependent diffusion coefficients are:

$$D_{zz} = \frac{c}{3t}\left\{\frac{t}{g_1} + \frac{3g_1 - g_2}{g_1^2(g_1 - g_2)}[1-\exp(-g_1 t)] + \frac{2}{g_2(g_1 - g_2)}[1-\exp(-g_2 t)] - \frac{3}{2g_1^2}[1-\exp(-g_1 t)]^2\right\} \tag{12}$$

$$D_{xx} = D_{yy} = \frac{c}{3t}\left\{\frac{t}{g_1} + \frac{g_2}{g_1^2(g_1 - g_2)}[1-\exp(-g_1 t)] + \frac{1}{g_2(g_1 - g_2)}[1-\exp(-g_2 t)]\right\} \ . \tag{13}$$

As shown in Eqs. (11) - (13), the mean position of the distribution is moving, and the diffusion coefficients are time dependent. At $t \to 0$, the mean position of the photon density moves along z direction with speed c, and the

diffusion coefficients tend to zero, this result presents a clear picture of near ballistic motion. As time increases, the mean position motion slows down, and the diffusion coefficients increase from zero. This stage of photon migration is often called a snakelike mode. At long time, Eq. (10) tends to the center-moved (1 l_{tr}) diffusion model with the diffusion coefficient $l_{tr}/3$.

3. Forward model based on the cumulant solution of RTE

The linear forward models for scattering media are built in following three steps: (1) computation of a background Green's function in an infinite uniform medium; (2) extension of this Green's function to slab geometry; and (3) computation of the weight function using a perturbative method. These steps have been applied in building the linear forward models under DA.[2] We use these steps as well, but our approach is based on the cumulant solution of RTE, rather than the solution of the diffusion equation.

We use the second order cumulant solution for computing a background Green's function in an infinite uniform medium, since it is easy to use the explicit expressions in Eq. (3) – Eq. (9), that avoid complicated computations of higher order cumulants. The second order cumulant solution is accurate at later times, but only provides the correct mean position and the correct HWHM at early times. We notice that the width of the distribution at early times could be smaller than the size of a voxel, the average over the distributions at different points in a voxel smears the detail shape of the distribution. In the CW or frequency-domain cases, the shape of the distribution is further smeared by integration over time t. Therefore the second order cumulant solution can be a reasonable approximation in building forward models based on the RTE.

Since a detector usually collects emergent light within a wide range of angle of different directions, it is convenient to compute the Green's function related to a detector using photon density $N(\mathbf{r}_d, t)$ [Eqs. (10)-(13)], where $\mathbf{r}_d$ is the position of detector.

It is essential to include the boundary effect in the solution of the RTE when photons are injected into and spread out from a finite sized medium. A proper extension of the cumulant solution to slab geometry is an essential step for building a forward model.

A boundary condition is applied based on the following physical consideration. At early times, the center of photon distribution injected into medium, moves forward into medium. Then the distribution spreads out from the moving center with diffusion coefficients that gradually increase from zero. At early times, the number of photons leaking out of the boundary is negligible compared to the total number of the incident photons. The boundary condition plays a role at later times, when there are many photons leaking out of the boundary.

The approach known as an approximate "extrapolated" boundary condition [16], extrapolates the boundary by a distance $\xi = \alpha\, l_{tr}$, the extrapolation length, beyond the real boundaries with $\alpha \sim 0.7$, at which the photon density vanishes.

To apply this boundary condition for the cumulant solution in a semi-infinite geometry, a. virtual negative source, S_v, is added to the original source, S, as shown in Fig. 3. During the early period, the solution of the RTE in an infinite uniform medium automatically satisfied the boundary condition because the density is near zero at the boundary, and the virtual source does not play a role. After a time of approximately 4 l_{tr}/c, the center of photon density, C, has moved and stopped at a position 1 l_{tr} from the original source S and the center from virtual source, C_v, has moved in a similar way. Then, the arrangement shown in Fig. 3, produces a cancellation of contributions to the photon density from the original source and the virtual source on the extrapolated boundary.

Fig. 4 shows that the time-resolved backscattered photon distribution in a semi-infinite medium on the $z = 0$ surface, with the source-detector distance 1 l_{tr}, obtained using the second-order cumulant approximation and the extrapolated boundary condition, which agrees with the Monte-Carlo simulation much better than that of the DA.

For extending to the slab geometry, adding a series of pairs of virtual "image" sources at both sides of slab is a good approximation for satisfaction of the extrapolated boundary conditions on both sides of a slab. [17]

The heterogeneous structure of a highly scattering turbid medium can be characterized by the following optical parameters: the scattering rate $\mu_s(\mathbf{r})$, the absorption rate $\mu_a(\mathbf{r})$, and the differential angular scattering rate $\mu_s(\mathbf{r})P(\mathbf{s}, \mathbf{s}', \mathbf{r})$.

A perturbation method is used which takes the photon distribution function in a uniform background slab medium as the zero-order approximation. The change of the photon distribution function originates from the change of optical parameters compared to that in the uniform background slab medium. The change of scattering and absorption parameters are defined as follows:

$$\begin{aligned} \Delta\mu_s(\mathbf{r}) &= \mu_s(\mathbf{r}) - \mu_s^{(0)}, \\ \Delta\mu_a(\mathbf{r}) &= \mu_a(\mathbf{r}) - \mu_a^{(0)}, \\ \Delta[\mu_s P](\mathbf{s}, \mathbf{s}', \mathbf{r}) &= \mu_s(\mathbf{r})P(\mathbf{s}, \mathbf{s}', \mathbf{r}), - \mu_s^{(0)}P^{(0)}(\mathbf{s}, \mathbf{s}'), \end{aligned} \qquad (14)$$

where the quantities with super index (0) are the optical parameters in a uniform background slab medium. By expanding $\Delta[\mu_s P](\mathbf{s}, \mathbf{s}', \mathbf{r})$ in Legendre polynomials, we obtain

$$\Delta[\mu_s P](\mathbf{s},\mathbf{s}',\mathbf{r}) = \frac{1}{4\pi}\sum_l [\Delta\mu_s(\mathbf{r}) a_l^{(0)} + \mu_s^{(0)} \Delta a_l(\mathbf{r})] P_l[\cos(\mathbf{s}\cdot\mathbf{s}')] \quad , \tag{15}$$

with $\Delta a_0(\mathbf{r}) = 0$, since a_0 always equals to 1. The physical meaning is that the scattering parameters have no effect on the s ($l = 0$) component.

Making a perturbation expansion of Eq. (1) to the first-order Born approximation, the change in the photon distribution is given by

$$\begin{aligned}\Delta I(\mathbf{r}_d,\mathbf{s}_d,t \mid \mathbf{r}_s,\mathbf{s}_s) = \int dt' \int d\mathbf{r} \int d\mathbf{s}' I^{(0)}(\mathbf{r}_d,\mathbf{s}_d,t-t' \mid \mathbf{r},\mathbf{s}') \\ \{\int \Delta[\mu_s P](\mathbf{s},\mathbf{s}',\mathbf{r}) I^{(0)}(\mathbf{r},\mathbf{s},t' \mid \mathbf{r}_s,\mathbf{s}_s) d\mathbf{s} - [\Delta\mu_s(\mathbf{r}) + \Delta\mu_a(\mathbf{r})] I^{(0)}(\mathbf{r},\mathbf{s}',t' \mid \mathbf{r}_s,\mathbf{s}_s)\}\end{aligned} \quad , \tag{16}$$

where $\Delta I(\mathbf{r}_d,\mathbf{s}_d,t|\mathbf{r}_s,\mathbf{s}_s)$ is the change in the light intensity received by a detector located at $\mathbf{r}_d$, along the direction $\mathbf{s}_d$, and at time t, which is injected from a source located at $\mathbf{r}_s$, along a direction of $\mathbf{s}_s$, at time $t = 0$. "Change" refers to the difference in intensity compared to that received by the same detector, from the same source, when light passes through a uniform background slab medium. The term $I^{(0)}(\mathbf{r}_2,\mathbf{s}_2,t|\mathbf{r}_1,\mathbf{s}_1)$ is the intensity of light, calculated using the cumulant solution of RTE, at $\mathbf{r}_2$ along the direction $\mathbf{s}_2$ and at time t, when light is injected from a position $\mathbf{r}_1$ along a direction of $\mathbf{s}_1$ at time $t = 0$ migrating in a uniform background slab medium.

The background Green's functions in Eq. (16), obtained by cumulant solution, are expanded in spherical harmonics:

$$\begin{aligned} I^{(0)}(\mathbf{r},\mathbf{s},t' \mid \mathbf{r}_s,\mathbf{s}_s) &= \sum_{l,m} A_{lm}(\mathbf{r},\mathbf{r}_s,\mathbf{s}_s,t') Y_{lm}(\mathbf{s}), \\ I^{(0)}(\mathbf{r}_d,\mathbf{s}_d,t-t' \mid \mathbf{r},\mathbf{s}) &= \sum_{l,m} C_{lm}^*(\mathbf{r},\mathbf{r}_d,\mathbf{s}_d,t-t') Y_{lm}^*(\mathbf{s}) . \end{aligned} \tag{17}$$

The spherical transform is performed using a fast Fourier transform for the integral over ϕ, and a Clenshaw-Curtis quadrature for the integral over θ.

Using the orthogonality relation of the spherical function and the addition theorem: $\sum_m Y_{lm}(\mathbf{s}) Y_{lm}^*(\mathbf{s}') = P_l[\cos(\mathbf{s}\cdot\mathbf{s}')]$, the analytical integration over $\mathbf{s}$ and $\mathbf{s}'$ in Eq. (16) can be performed. For time resolved data, the contribution from an absorbing object located at $\mathbf{r}_k$ is given by

$$\Delta I(\mathbf{r}_d,\mathbf{s}_d,\mathbf{r}_s,\mathbf{s}_s,t \mid \mathbf{r}_k) = -\Delta\mu_a(\mathbf{r}_k)\delta V_k \int_0^t dt' \sum_{l=0}^{L} \frac{4\pi}{(2l+1)} \sum_m A_{lm}(\mathbf{r}_k,\mathbf{r}_s,\mathbf{s}_s,t') C_{lm}^*(\mathbf{r}_k,\mathbf{r}_d,\mathbf{s}_d,t-t') \tag{18}$$

where δV_k is the volume of k^{th} voxel, and L is the cut-off value in the Legendre expansion in Eq. (18). The contribution from a scattering object located at $\mathbf{r}_k$ is given by

$$\begin{aligned}\Delta I(\mathbf{r}_d,\mathbf{s}_d,\mathbf{r}_s,\mathbf{s}_s,t \mid \mathbf{r}_k) = \\ -\delta V_k \int_0^t dt' \sum_{l=1}^{L} \frac{4\pi}{(2l+1)} \left[\Delta\mu_s(\mathbf{r}_k)\left(1 - \frac{a_l^{(0)}}{2l+1}\right) - \mu_s^{(0)} \frac{\Delta a_l(\mathbf{r}_k)}{2l+1}\right] \sum_m A_{lm}(\mathbf{r}_k,\mathbf{r}_s,\mathbf{s}_s,t') C_{lm}^*(\mathbf{r}_k,\mathbf{r}_d,\mathbf{s}_d,t-t')\end{aligned} \tag{19}$$

For Frequency domain (or CW) data, the contribution from an absorbing object located at $\mathbf{r}_k$ is given by

$$\Delta I(\mathbf{r}_d,\mathbf{s}_d,\mathbf{r}_s,\mathbf{s}_s,\omega \mid \mathbf{r}_k) = -\Delta\mu_a(\mathbf{r}_k)\delta V_k \sum_{l=0}^{L} \frac{4\pi}{2l+1} \sum_m A_{lm}(\mathbf{r}_k,\mathbf{r}_s,\mathbf{s}_s,\omega) c_{lm}^*(\mathbf{r}_k,\mathbf{r}_d,\mathbf{s}_d,\omega), \tag{20}$$

and the contribution from a scattering object located at $\mathbf{r}_k$ is given by

$$\begin{aligned}\Delta I(\mathbf{r}_d,\mathbf{s}_d,\mathbf{r}_s,\mathbf{s}_s,\omega \mid \mathbf{r}_k) = \\ -\delta V_k \sum_{l=1}^{L} \frac{4\pi}{2l+1} \left[\Delta\mu_s(\mathbf{r}_k)\left(1 - \frac{a_l^{(0)}}{2l+1}\right) - \mu_s^{(0)} \frac{\Delta a_l(\mathbf{r}_k)}{2l+1}\right] \sum_m A_{lm}(\mathbf{r}_k,\mathbf{r}_s,\mathbf{s}_s,\omega) c_{lm}^*(\mathbf{r}_k,\mathbf{r}_d,\mathbf{s}_d,\omega).\end{aligned} \tag{21}$$

Comparing Eqs. (18)—(21) with the corresponding weight function commonly used in the diffusion approximation, [1,2] only *s* wave (l=0) for absorptive objects, and only *p* wave (l=1) for scattering objects are considered in the diffusion forward models. Besides, even for *s* wave and *p* wave, the diffusive solution is incorrect when voxels are located near the source, as discussed before.

Above formulae allow simulating the background Green's function and the change of optical parameters in detail. They are also applicable to the cases where only a few parameters of the medium are known, similar to that for the diffusion forward model. When only $\mu_s^{(0)}$, $\mu_a^{(0)}$, and *g*-factor for an uniform background medium are given, the Henyey-Greenstein phase function [18] is widely adopted as an approximate phase function:

$$P(\cos\theta) = \frac{1}{4\pi}\frac{1-g^2}{(1+g^2-2g\cos\theta)^{3/2}} = \frac{1}{4\pi}\sum_l (2l+1)g^l P_l(\cos\theta)\,. \qquad (22)$$

Although Eq. (22) uses a single parameter, *g*-factor, to describe a phase function, this description is much better than that used in the DA, which implies a phase function linear in $\cos\theta$.

If Δa_l (**r**) in Eq. (21), which represent the change of the phase function, is not considered, two optical parameters being imaged are $\Delta\mu_a(\mathbf{r})$ and $\Delta\mu_s(\mathbf{r})$. The reduced scattering coefficient $\Delta\mu_s(1-a_1^{(0)}/3)$ is directly related to ΔD (change of the diffusion coefficient) used in the DA models. The CFM, hence, can be applied to the experimental data in a similar fashion as that for the DA models, to obtain images of the optical parameters. In the CFM, however, all contributions from higher spherical waves are properly included.

The most time consuming part in computation of CFM using the above formulae is to build a database of A_{lm} and C^*_{lm}. Once it is built for a uniform background medium, the database can be applied for imaging of various heterogeneity cases. In parallel geometry, A_{lm} is a function of (x_k-x_s, y_k-y_s) due to the 2D translation invariance. Since position of source z_s and incident direction $\mathbf{s}_s$ are fixed, only a 3D (x_k-x_s, y_k-y_s, z_k) database is required. When $\mathbf{s}_s$ is taken along *z* direction (light is injected perpendicular to surface), the scale of database is reduced to 2D due to the *z* axis symmetry. Photons from different directions in a wide solid angle are received by a detector, as discussed before, photon density $N(\mathbf{r}_d-\mathbf{r}, \mathbf{s}, t)$ is used for computing the Green's function associated with detectors, which is independent of $\mathbf{s}_d$, and C^*_{lm} can be computed much easily. The database can be built in a reasonable computation time because the distribution function $I^{(0)}(\mathbf{r}_2,\mathbf{s}_2,t|\mathbf{r}_1,\mathbf{s}_1)$ can be rapidly calculated using the analytical expressions.

4. Fast 3D hybrid dual Fourier (HDF) inverse algorithm

We now outline an inverse algorithm to quickly reconstruct image of a medium from acquired measurements using the above CFM. The above model, neglecting the irrelevant parameters, can be briefly written as

$$Y(\vec{r}_d, \vec{r}_s, z_d, z_s) = \int d\vec{r}dz W(\vec{r}_d-\vec{r}, \vec{r}_s-\vec{r}, z, z_d, z_s)X(\vec{r}, z)\,, \qquad (23)$$

where $\vec{R} = (\vec{r}, z)$ is the position of a voxel inside turbid medium; $\vec{r}$ is (*x*, *y*) coordinates; $\vec{R}_s = (\vec{r}_s, z_s)$ is the position of a source; and $\vec{R}_d = (\vec{r}_d, z_d)$ is the position of a detector. In Eq. (23), $Y(\vec{r}_d, \vec{r}_s, z_d, z_s)$ is the measured change in light intensity received by a detector at $\vec{R}_d$ from a point source at $\vec{R}_s$. $X(\vec{r}, z)$ is the change of the optical parameters inside turbid medium. The weight function $W(\vec{r}_d-\vec{r}, \vec{r}_s-\vec{r}, z, z_d, z_s)$ is a function of $\vec{r}_d-\vec{r}$ and $\vec{r}_s-\vec{r}$ on (*x*, *y*) plane, because of parallel geometry, assuming an infinite sized area, and the 2D translation invariance of the Green's function in a background homogeneous slab. Here, the special form of the weight function is not relevant; the weight function can be calculated by the CFM or the DA models, using with CW, frequency, or time-resolved data. This approach is general and can also be used for inverse problems of non-optical measurements in parallel geometries.

A light source scans through a 2D array. Transmitted or backscattered light signals emerging from the medium are detected using a 2D array of detectors, such as a CCD camera (or time-gated CCD camera in the time resolved case). Each illumination of the light source provides a set of 2D data on the two-dimensional detector array. For CW or frequency-modulated light source, this arrangement can produce a set of 2Dx2D = 4D data in a relatively short acquisition time, because a CCD camera produces 2D data of the detectors at different positions simultaneously. When time-resolved or modulation at multiple frequencies are applied, a set of 5D data can be acquired. The inverse problems of 3D imaging, hence, are over-determined, which is necessary for obtaining an accurate 3D image.

When the translation invariance is satisfied, the Fourier transform approach is a powerful technique to achieve a fast inversion. In the Fourier space, the convolution of *W* and *X* becomes a product of *W* and *X*, and the weight

matrix W becomes diagonal. Hence, inversion can be performed much faster. Using this concept in the case of multiple sources and multiple detectors in parallel geometries a dual 2D Fourier transform $\int d\vec{r}_s d\vec{r}_d e^{i\vec{q}_s\vec{r}_s} e^{i\vec{q}_d\vec{r}_d}$ is performed on Eq. (23), to obtain

$$\int d\vec{r}_s d\vec{r}_d e^{i\vec{q}_s\vec{r}_s} e^{i\vec{q}_d\vec{r}_d} Y(\vec{r}_s,\vec{r}_d,z_s,z_d) =$$

$$\int dz \int d\vec{r} \int d(\vec{r}_s-\vec{r}) d(\vec{r}_d-\vec{r}) e^{i\vec{q}_s(\vec{r}_s-\vec{r})} e^{i\vec{q}_d(\vec{r}_d-\vec{r})} W(\vec{r}_s-\vec{r},\vec{r}_d-\vec{r},z_s,z_d,z) e^{i(\vec{q}_s+\vec{q}_d)\vec{r}} X(\vec{r},z)$$

which leads to

$$\hat{Y}(\vec{q}_d,\vec{q}_s,z_d,z_s) = \int dz \hat{W}(\vec{q}_d,\vec{q}_s,z,z_d,z_s)\hat{X}(\vec{q}_d+\vec{q}_s,z), \qquad (24)$$

where $\hat{Y}$, $\hat{X}$, and $\hat{W}$ are change in light intensity, change in optical parameters, and the weight function in the Fourier space respectively.

A similar form of this dual Fourier transform has been derived by Markel and Schotland [13,14] in a frequency-domain diffusion model.

Eq. (24) seems difficult to be used for performing the inverse reconstruction because of the argument mismatch $(\vec{q}_d+\vec{q}_s)$ in $\hat{X}$ and $(\vec{q}_s, \vec{q}_d)$ in $\hat{Y}$ and $\hat{W}$. This difficulty occurs because the weight function in Eq. (23) is related to three positions: $\vec{r}_d$, $\vec{r}_s$, and $\vec{r}$. To remove this complexity, the following linear hybrid transform is introduced:

$$\begin{aligned} \vec{u} &= \vec{q}_d + \vec{q}_s \\ \vec{v} &= \vec{q}_d - \vec{q}_s \end{aligned} \qquad (25)$$

This results in HDF formula:

$$\tilde{Y}(\vec{u},\vec{v},z_d,z_s) = \int dz \tilde{W}(\vec{u},\vec{v},z,z_d,z_s)\tilde{X}(\vec{u},z) \quad , \qquad (26)$$

where $\tilde{Y}$, $\tilde{X}$, and $\tilde{W}$ are, respectively, $\hat{Y}$, $\hat{X}$, and $\hat{W}$ as functions of $\vec{u}$ and $\vec{v}$.

While Eq. (25) is a relatively simple expression, it is essential to properly realize this hybrid transform in discrete lattices of the Fourier space. A procedure to quickly perform this transform from (q_d, q_s) coordinates to new (u, v) coordinates, separately, for x and y components, is explained in Fig. 5 using an example of a 6x6 lattice. The maximum value of u is taken as the maximum value of q_d or q_s, not the maximum value of $q_d + q_s$. The periodic property of lattice in the Fourier space is used, for example, $\tilde{Y}$ (u=2, v=4) = $\hat{Y}$ (q_d=3, q_s=5). This procedure builds a one-to-one correspondence between lattices in the two coordinate systems. Fig. 5 shows that $\tilde{Y}$ and $\tilde{W}$ at each node [circle in Fig. 5] in (u, v) coordinates are directly mapped from $\hat{Y}$ and $\hat{W}$, respectively, at the corresponding node in (q_d, q_s) coordinates without any algebraic manipulation.

In Eq. (26), a common 2D Fourier argument $\vec{u}$ appears in $\tilde{Y}$, $\tilde{X}$, and $\tilde{W}$. For each value of $\vec{u}$, Eq. (26) leads to an over-determined 1D problem for inverse reconstruction: $\tilde{Y}(\vec{v}) = \int dz \tilde{W}(\vec{v},z)\tilde{X}(z)$. In order to perform fast inversion, we invert the normal form of the forward model: $\tilde{Y}\,\tilde{W}^T = [\tilde{W}^T\tilde{W}]\,\tilde{X}$ for each $\vec{u}$, where $[\tilde{W}^T\tilde{W}]$ is a MxM matrix, with M the number of layers in z direction. The original W in Eq. (23) is a matrix with a large dimension. The inverse problem now is simplified to invert many (number of discrete value of $\vec{u}$) matrices, each with a small dimension M. The latter problem is much more computationally efficient compared to the original problem of Eq. (23). Once $\tilde{X}(\vec{u},z)$ are obtained for all $\vec{u}$, a 2D inverse Fourier transform produces $X(\vec{r},z)$, which is the 3D image of optical parameters of the medium. Markel and Schotland use different procedures for inversion. In [13] a Fourier-Laplace inversion is applied, hence, an analytic continuation of measured data to the complex plane is required for the inverse Laplace transform. In [14] an inverse procedure is performed in an argument space, similar to variables $\vec{v}$ here. Since $\vec{v}$ include 2D variables, inversion in $\vec{v}$ space could take longer time than that of inversion in z space.

As discussed before, matrices $\widetilde{W}$ and $[\widetilde{W}^T\widetilde{W}]$ for each $\vec{u}$ can be calculated in advance for a uniform background slab medium. Assuming that a group of experimental data has been acquired, the following steps are taken to produce a 3D image of the medium:

(1) Obtain "change" of intensities, $Y(\vec{r}_d, \vec{r}_s, z_d, z_s)$, by subtracting the intensity for a uniform background medium from the measured intensity;

(2) Extend the (x, y) area and padding zeros, to overcome the wraparound problem in discrete convolutions; [19]

(3) Perform a dual 2D fast Fourier transform (FFT) of $Y(\vec{r}_d, \vec{r}_s, z_d, z_s)$ in the extended area to produce $\hat{Y}(\vec{q}_d, \vec{q}_s, z_d, z_s)$;

(4) Determine $\widetilde{Y}(\vec{u}, \vec{v}, z_d, z_s)$ for each $\vec{u}$, using a mapping procedure explained in Fig. 5;

(5) Invert $\widetilde{Y}\ \widetilde{W}^T = [\widetilde{W}^T\widetilde{W}]\widetilde{X}$ for each $\vec{u}$, which is an inverse problem involving a MxM matrix, with M the number of layers along z direction. Proper regularization according to noise level needs to be taken into account. Regularization will be discussed later in the paper; and

(6) Finally, perform an inverse 2D FFT on $\widetilde{X}(\vec{u}, z)$ to produce $X(\vec{r}, z)$.

Our computational experiments show it takes only 1-2 minutes on a personal computer to perform an inverse reconstruction of a 3D image of a medium with a large number of voxels (for example, 32x32x20 voxels) using this HDF algorithm.

To demonstrate our concept of HDF tomography in 3D image reconstruction, an example using simulated CW data is presented. A slab turbid medium, with a transport mean free path l_{tr} = 1 mm, absorption length l_a = 300 mm, and thickness z_d = 40 mm, is divided into 20 layers. A CW light source, injected perpendicular to the z_s = 0 plane, scans by a 2D 32X32 array on the plane, with each pixel 3mmx3mm. A 2D array of detectors with the same spacing is located at z_d plane (transmission geometry). The medium, is divided into 32x32x20 voxels, each of dimension 3x3x2 mm^3. Two absorbing objects are located in the medium, each with a volume 3x3x2 mm^3. The first one located at (10, 10, 10) has an absorption difference of $\Delta\mu_a$ = 0.01 mm^{-1} with the background. The second one is located at (20, 20, 15) with an absorption difference of 0.007 mm^{-1}. The simulated data with noise level of 5% are obtained using the CFM. The tomographic images are shown in Fig. 6. As shown, the central positions of 3D image of the objects are correct, located at a voxel (10, 10, 10) with red color, and a voxel (20, 20, 15) with yellow color. The resolution of image is about ~ 6 mm in the transverse (x, y) plane and ~ 10 mm along z direction. In general, the axial resolution (along z direction) is poorer than the lateral resolution [on the (x, y) plane]. In transmission geometry, two Green's functions in the weight function compensate each other when the z position of the object changes, that leads to a poor sensitivity of the measured photon intensity to the z position of the object. The shapes of 3D image of two objects are ellipsoids with longer axis along z direction. The absorption difference has the maximum value at the center of ellipsoid, and decays gradually with increase distance from the center.

A cut-off in discrete lattices of $\vec{q}_s$ and $\vec{q}_d$ naturally introduces a kind of regularization. This regularization is very effective. Initial tests show that even adding 30% of fluctuations on simulated data of $Y(\vec{r}_d, \vec{r}_s, z_d, z_s)$, an image similar to that shown in Fig. 6 is still reconstructed. The reason for this is that noises come from fluctuations at different source and detector positions, which are mainly the high frequency components of $\vec{q}_s$ and $\vec{q}_d$. A cut-off in $\vec{q}_s$ and $\vec{q}_d$ naturally eliminates these high frequency noises, such that a stable image, especially in (x, y) plane, can be reconstructed in a strong noise level.

However, the inverse problem is still ill-posed, because contribution to the change of intensity from a small voxel deeply inside medium is weak, and is not sensitive to its z position in transmission case. A regularization procedure on inversion of $\widetilde{Y}\ \widetilde{W}^T = [\widetilde{W}^T\widetilde{W}]\widetilde{X}$ is still needed. The standard Tikhonov regularization approach [20] is applied and L-curve [21,22] method is used for determining the best regularization parameters.

This fast inverse algorithm produces a 3D image in a linear image regime. For nonlinear image reconstruction procedure, the reconstructed 3D image provides a good initial profile for further refining the 3D image taking the nonlinear effects into consideration.

The HDF inversion method can be extended to a cylindrical geometry, with an arbitrary shape of the (*x*, y) cross section, for 3D image reconstruction. In this geometry, an algorithm using a single Fourier inversion has been developed.[23] This algorithm is limited to the case that the sources and the detectors are located on a plane with same *z* coordinates. The hybrid-dual-Fourier inverse approach in cylindrical geometry removes this restriction, so more data can be acquired for 3D tomography. The linear forward model in cylindrical geometry is given by

$$Y(\vec{r}_d, \vec{r}_s, z_d, z_s) = \int d\vec{r} dz W(\vec{r}_d, \vec{r}_s, \vec{r}; z_d - z, z_s - z) X(\vec{r}, z) \ , \qquad (27)$$

where $W(\vec{r}_d, \vec{r}_s, \vec{r}; z_d - z, z_s - z)$ is the weight function, a function of $z_d - z$ and $z_s - z$ due to the 1D translation invariance of the Green's function in a homogeneous background medium in cylindrical geometry (assuming infinite *z* length). We make a dual 1D (along *z* direction) Fourier transform $\int dz_d dz_s e^{iq_d z_d} e^{iq_s z_s}$ on Eq. (27) to obtain

$$\hat{Y}(q_d, q_s, \vec{r}_d, \vec{r}_s) = \int dz \hat{W}(q_d, q_s, \vec{r}, \vec{r}_d, \vec{r}_s) \hat{X}(q_d + q_s, \vec{r}), \qquad (28)$$

where $\hat{Y}$, $\hat{X}$, and $\hat{W}$ are the Fourier space quantities corresponding that in Eq. (27).

The (1D) linear hybrid coordinate transforms, $u = q_d + q_s$, and $v = q_d - q_s$, for Eq. (28) leads to:

$$\tilde{Y}(u, v, \vec{r}_d, \vec{r}_s) = \int d\vec{r} \tilde{W}(u, v, \vec{r}_d, \vec{r}_s; \vec{r}) \tilde{X}(u, \vec{r}) \ , \qquad (29)$$

where $\tilde{Y}$, $\tilde{X}$, and $\tilde{W}$ are, respectively, $\hat{Y}$, $\hat{X}$, and $\hat{W}$ as functions of u and v. For each value of u, Eq. (29) is an over determined 2D problem for inverse reconstruction, namely, to determine a 2D unknown value of $\tilde{X}(u, \vec{r})$ from known 3D data of $\tilde{Y}(u, v, \vec{r}_d, \vec{r}_s)$ for each u. This 3D-2D determination enhances the accuracy of 3D image compared to 2D-2D determination in the single-Fourier transform inversion. After $\tilde{X}(u, \vec{r})$ are obtained for all u, a 1D inverse Fourier transform produces the image $X(\vec{r}, z)$.

5. Discussion

As shown in Eqs. (19) and (21), there is no contribution from *s* wave to the weight function for a scattering object. This result reflects a fact that no scattering effect exists for an isotropic angular distribution. In the regions far from sources, the weight function contributed from scattering objects is small because there is no contribution from the dominant *s* wave, as shown in many results based on the diffusion models.[1-5] This non-sensitivity of signals to the scattering objects deep inside the medium should be considered in optical tomography. A pure isotropic distribution is never achieved, otherwise, there will be no flux in any directions. In the diffusive model, a small *p* wave, $-(3/4\pi)D\mathbf{s} \cdot \nabla N$, exists which maintains the photons diffusing to the regions with fewer photons. The factor $-\nabla N$ represents this effect. However, this expression is valid only in the regions where the *p* wave is much smaller than *s* wave, $(1/4\pi)N$, and does not correctly describe the early photon propagation near sources. Since only the weight function for scattering objects close to sources plays an important role, but it was estimated using the formula valid in regions far from sources, substantial error introduced in the diffusion forward model for scattering objects is crucial.

For the weight function of absorbing objects, contributions from all spherical components, including *s* wave, are given in Eqs. (18) and (20). In commonly used diffusion formula the contribution from *p* wave was neglected. The diffusion coefficient originally derived in the DA is $D = 1/(3\mu_s' + \mu_a)$, that leads to $\Delta D = -D^{(0)2}(3\Delta\mu_s' + \Delta\mu_a)$. The contribution from *p* wave to the weight function for absorbing objects, hence, should exist. But in the later diffusion models ΔD is assigned only for scattering objects and only *s* wave for absorbing objects is taken. Eqs. (18) and (20) provide a quantitative estimation of weight function for absorbing objects in regions close to the source, as well as far from the source..

The CFM and the HDF inverse algorithm need further improvements in the following aspects. Further improvement should be considered without significantly increasing complexity in computation. First, the second cumulant solution is not accurate in the detailed shape of the distribution, especially, the front edge in the Gaussian distribution violates causality. An empirical distribution, which keeps the exact value of the first and second cumulants, while satisfies the causality, can be designed to replace the Gaussian distribution.

Second, the boundary condition is approximate. When a more accurate distribution $I(\mathbf{r}, \mathbf{s}, t)$ at early time is needed, the boundary condition for a semi-infinite geometry should be

$$I(x, y, z = 0; \theta, \phi, t) = 0 \ , \qquad \text{if } \cos\theta > 0 . \tag{30}$$

This type of the boundary condition was studied by Domke [24] for the steady state case. The solution is represented as a superposition of a solution describing a transport problem in an infinite medium, and a Fredholm integral term, which corrects this solution for the appropriate half-space boundary condition. This approach may be used for further development of the boundary problem.

Third, to consider the nonlinear effects, $I^{(0)}$'s in Eq. (16) should be replaced by the Green's function in a real heterogeneous medium. Among the high-order perturbative corrections of the Green's function, the "self-energy" diagram, which counts photon round trips through a position up to infinite times, plays an important role. Gandjbakhche et al [25] studied this effect using a random walk model. We find that a renormalization procedure for this nonlinear effect can be performed after image is obtained using a linear inversion process. This renormalization procedure can recover the optimal value of the optical parameters and can improve the resolution of image. The detailed results of the renormalization will be published elsewhere.

The translation invariance is valid for the parallel geometry assuming that the (x, y) area is infinite. We suppose that this assumption of the infinite area is reasonable. How much error arises due to the finite area of a sample will be studied in details.

Use of the simulated data mainly tests the validity of the inverse algorithm, does not test accuracy of the forward model. Experimental data from phantoms and in vivo measurements in human body will be performed for further testing of our approach.

In summary, we have developed a linear forward model of light propagation in a turbid medium based on an analytical cumulant solution of the radiative transfer equation for 3D optical tomography. The model can be used for CW, frequency-domain, and time-resolved measurements in parallel geometries. This forward model is more accurate than the forward model based on the diffusion approximation of RTE. An inverse algorithm is developed, based on a fast 3D hybrid-dual-Fourier tomographic approach using multiple detectors and multiple sources in parallel geometries. This inverse algorithm is computationally efficient and is suitable for clinical applications, such as beast cancer detection.

Acknowledgments

We are grateful to S. K. Gayen for careful reading this manuscript and useful discussion. This work was supported in part by the U.S. Department of the Army (grant DAMD17-02-1-0516). The US Army Medical Research Acquisition Activity, 820 Chandler Street, Fort Detrick, Maryland 21702-5014 is the awarding and administering acquisition office. Additional support is given by the US Army Medical Research and Materiels Command (Grant DAMD17-98-1-8147), NASA, and NYSTAR.

References

[1] A. G. Yodh, B. Tromberg, E. Sevick-Muraca, D. Pine, ed. "Diffusion photons in turbid media", a special issue of J. Opt. Soc. A. A vol. 14, 136 (1997).

[2] S. R. Arridge, "Optical tomography in medical imaging", Inverse Problems, vol 15, 41 (1999).

[3] N. Iftimia, H. Jiang, "Quantitative optical image reconstruction of turbid media using dc measurements", Appl. Opt. Vol 39, 5256 (2000).

[4] B. W. Pogue, S. P. Poplack, T. O. McBride, W. A. Wells, O.K.S., U. L. Osterberg, K. D. Paulsen, "Quantitative Hemoglobin Tomography with Diffuse Near Infrared Spectroscopy: Pilot Results in the breast", Radiology, Vol 218, 261(2001).

[5] J. C. Hebden, H. Veenstra, H. Dehghani, E. M. C. Hillman, M. Schweiger, S. R. Arridge, D. T. Delpy, "Three dimensional time-resolved optical tomography of a conical breast phantom" Appl. Opt. Vol. 40 3278 (2001).

[6] H. Hielscher, R. E. Alcouffe, B. L. Barbour, "Comparison of finite-difference transport and diffusion calculation for photon migration in homogeneous and heterogeneous tissues", Phys. Med. Biol. Vol 43, 1285 (1998).

[7] T. Vilhunen, M. Vanhkonen, V. Kolehmainen, J. P. Kaipio, " Linking the radiative transfer equation and the diffusion approximation", Digest of OSA Biomedical Topical Meeting, 12 (2002).

[8] W. Cai, M. Lax, R. R. Alfano, "Cumulant solution of the elastic Boltzmann transport equation in an infinite uniform medium", Phys. Rev. E. Vol. 61 3871 (2000).

[9] W. Cai, M. Lax, R. R. Alfano, "Analytical solution of the elastic Boltzmann transport Equation in an infinite uniform medium using cumulant expansion", J. Phys. Chem. Vol B104, 3996 (2000).

[10] C. L. Matson, N. Clark, L. McMackin, J. S. Fender, "Three-dimensional tumor localization in thick tissue with the use of diffuse photon-density waves", Appl. Opt. Vol. 36, 214 (1997).

[11] X. D. Li, T. Durduran, A. G. Yodh, B. Chance, D. N. Pattanayak, "Diffraction tomography for biochemical imaging with diffuse-photon density waves", Opt. Lett. Vol. 22, 573 (1997).
[12] J. C. Schotland, V. A. Markel, "Inverse scattering with diffusing wave", J. Opt. Soc. Am. A Vol. 18, 2767 (2001).
[13] V. A. Markel, J. C. Schotland, "Inverse problem in optical diffusion tomography. I Fourier-Laplace inversion formulas", J. Opt. Soc. Am. A Vol. 18, 1336 (2001).
[14] V. A. Markel, J. C. Schotland, "Inverse scattering for the diffusion equation with general boundary conditions", Phys. Rev. E Vol. 64, 035601 (2001).
[15] M. E. Zevallos, A. Ya Polischuck, B. B. Das, F. Liu, R. R. Alfano, "Time-resolved photon-scattering measurements from scattering media fitted to non-euclidean and conventional diffusion models", Phys. Rev. E Vol. 57, 7244 (1998).
[16] M. S. Patterson, B. Chance, B. C. Wilson, "Time-resolved reflectance and transmittance for the non-invasive measurement of tissue optical properties", Appl. Opt. Vol. 28, 2331 (1989).
[17] M. Xu, W. Cai, M. Lax, R. R. Alfano,"Photon migration in turbid media using a cumulant approximation to radiative transfer", Phys. Rev. E . Vol. 65, 066609 (2002).
[18] L.G. Henyey, J. L. Greenstein, "Diffuse radiation in the galaxy", Astrophys. J. Vol. 93, 70 (1941).
[19] W. H. Press, B. P. Flannery, S. A. Teukolsky, W. T. Vetterling, *Numerical Recipes*, Cambridge University Press, P407 (1986).
[20] A. N. Tikhonov, A. V. Groncharsky, eds., *Ill-posed problems in the natural sciences*, MIR, Moscow, (1987).
[21] P. Hansen, D. O'Leavy, "The use of the L-curve in the regularization of discret ill-posed problems", SIAM J. Sci. Comput. Vol. 14, 1487(1993).
[22] W. Cai, S. K. Gayen, M. Xu, M. Zevallos, M. Alrubaiee, M. Lax, and R. R. Alfano, "Optical tomographic image reconstruction from ultrafast time-sliced transmission measurements", Appl. Opt. Vol. 38, 4237 (1999).
[23] W. Cai, B. B. Das, F. Liu, F. A. Zeng, M. Lax, R. R. Alfano, "Three dimensional image reconstruction in highly scattering turbid media", Proc. SPIE 2979, 241 (1997).
[24] H. Domke, "Reduction of Radiative Transfer Problems in Semi-infinite Media to Linear Fredholm Integral Equations", J. Quant. Spectrosc. Radiat. Transfer. Vol. 16, 973 (1976).
[25] A. H. Gandjbakhche, R. F. Bonner, R. Nossal, and G. H. Weiss, "Absorptivity contrast in transillumination imaging of tissue abnormalities" Appl. Opt. Vol. 35, 1767 (1996).

Figure Captions

Fig. 1 Distribution function $I(\mathbf{r}, \mathbf{s}, t)$ in an infinite uniform scattering medium as a function of time t, using Henyey-Greenstein phase function with $g = 0.9$. The detector is located at $R = 6l_{tr} = 60\ l_s$ from the source front along direction of incident light, and the direction is along the incident direction. The solid curve is computed from approximation up to 10th order of cumulant; the dotted curve is computed from approximation up to the second order of cumulant, the discrete red dots are from the Monte Carlo simulation; the curve of thick dots is from the diffusion approximation (DA), $N(\mathrm{r}, t)/4\pi$.

Fig. 2 The light distribution in an infinite uniform medium as a function of time at different received angle, using second cumulant solution of radiative transfer equation, where detector is located, separately, at 10 mm (Fig. 2a) and 30 mm (Fig. 2b) from the source in the incident direction. The parameters for this calculation are: $l_{tr} = 2$ mm, $l_a =$ 300 mm, the phase function is computed using Mie theory for polystyrene spheres with diameter $d = 1.11$ μm in water and the wavelength of laser source $\lambda = 625$ nm, which gives the g-factor $g = 0.926$.

Fig. 3 A schematic diagram shows how to extend the cumulant solution of RTE from an infinite medium to a semi-infinite medium.

Fig. 4 Backscattered photon distribution $I(\mathbf{r}, \mathbf{s} = -\mathbf{z}, t)$ emerging from plane surface of a semi-infinite turbid medium, as a function of time, with the source-detector distance 1 l_{tr} on the surface $z = 0$ plane. The pulse source is located at $z = 0$, incident along z direction. The extrapolated boundary condition is used. The solid curve is obtained from cumulant approximation (CA), up to the second cumulant. The dashed curve is from diffusion approximation (DA). The cross points are obtained from Monte Carlo simulation (MC).

Fig. 5 An example of a 6x6 lattice for explaining the linear hybrid transform from (q_d, q_s) coordinates to (u, v) coordinates.

Fig. 6. A 3D image reconstructed using hybrid dual Fourier tomography. Two absorbing objects, each with the volume 3x3x2 mm^3, are located inside a turbid medium with volume 96x96x40 mm^3 divided into 32x32x20 voxels. The first one is located at position labeled (10, 10, 10) with absorption difference $\Delta\mu_a = 0.01$ mm^{-1}. The second one is located at position labeled (20, 20, 15) with absorption difference $\Delta\mu_a = 0.007$ mm^{-1}. A CW light source incident perpendicular to the $z_s = 0$ plane is scanned through a 2D 32X32 array at the plane, with each pixel 3mmx3mm. A same sized 2D array of detectors is located at z_d plane (transmission geometry). The simulated data are produced with noise 5%. A linear scale of color bar from the maximum value to minimum value of $\Delta\mu_a$ is used. The numbers labels the z layers counting form source to the detector, layers are separated by 2 mm.

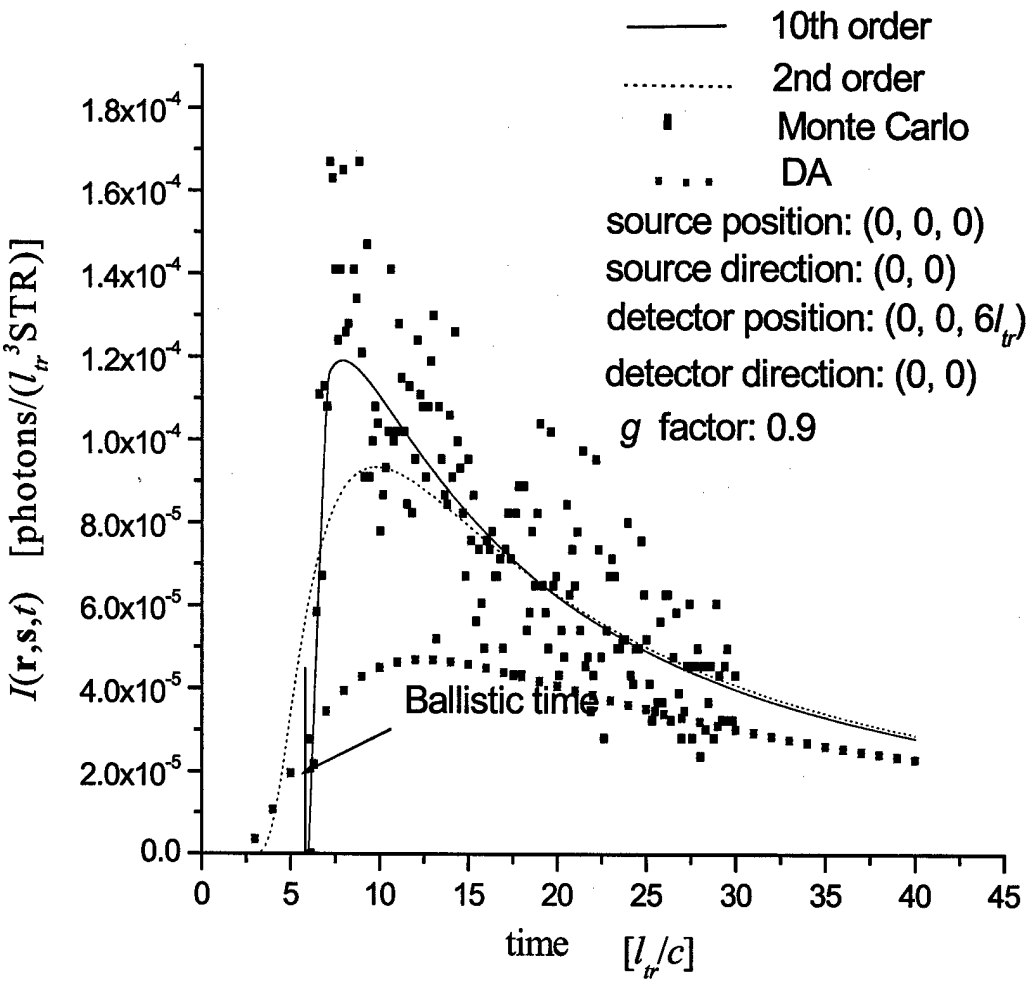
10th order
2nd order
Monte Carlo
DA
source position: (0, 0, 0)
source direction: (0, 0)
detector position: (0, 0, 6l_{tr})
detector direction: (0, 0)
g factor: 0.9
Ballistic time
$I(\mathbf{r},\mathbf{s},t)$ [photons/(l_{tr}^3STR)]
time $[l_{tr}/c]$
1.8x10^{-4}
1.6x10^{-4}
1.4x10^{-4}
1.2x10^{-4}
1.0x10^{-4}
8.0x10^{-5}
6.0x10^{-5}
4.0x10^{-5}
2.0x10^{-5}
0.0
0
5
10
15
20
25
30
35
40
45

Fig. 1

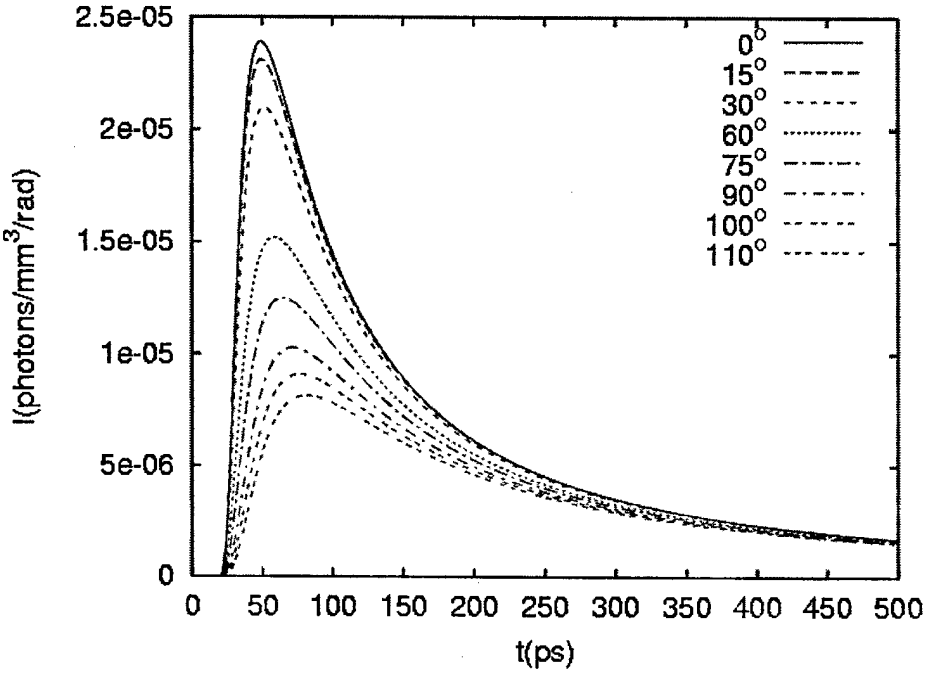
2.5e-05
2e-05
1.5e-05
1e-05
5e-06
0
I(photons/mm3/rad)
0 50 100 150 200 250 300 350 400 450 500
t(ps)
0°
15°
30°
60°
75°
90°
100°
110°

(a)

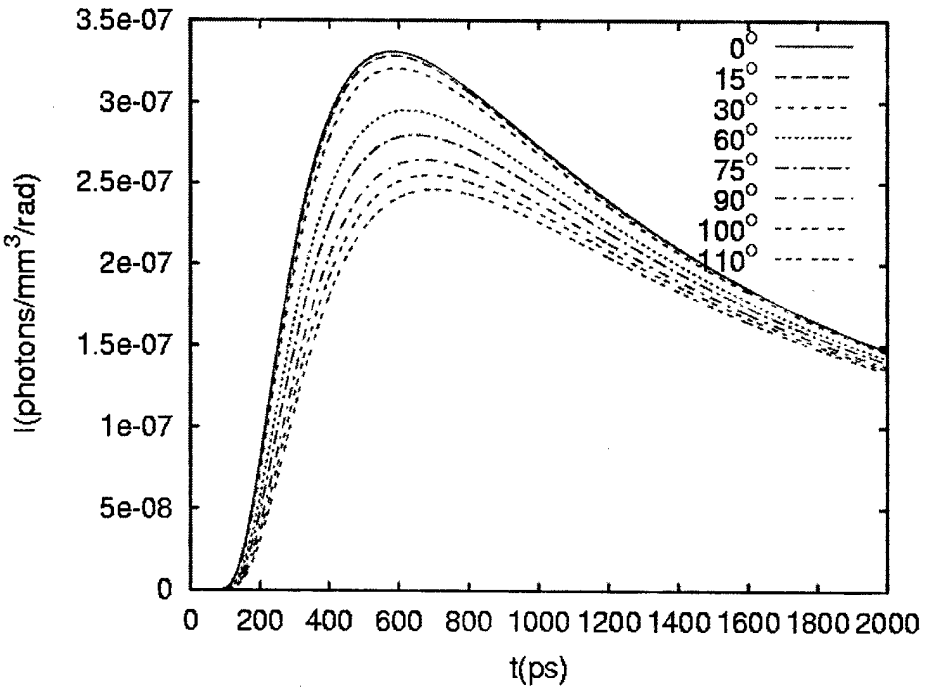
3.5e-07
3e-07
2.5e-07
2e-07
1.5e-07
1e-07
5e-08
0
I(photons/mm3/rad)
0 200 400 600 800 1000 1200 1400 1600 1800 2000
t(ps)
0°
15°
30°
60°
75°
90°
100°
110°

(b)

Fig. 2

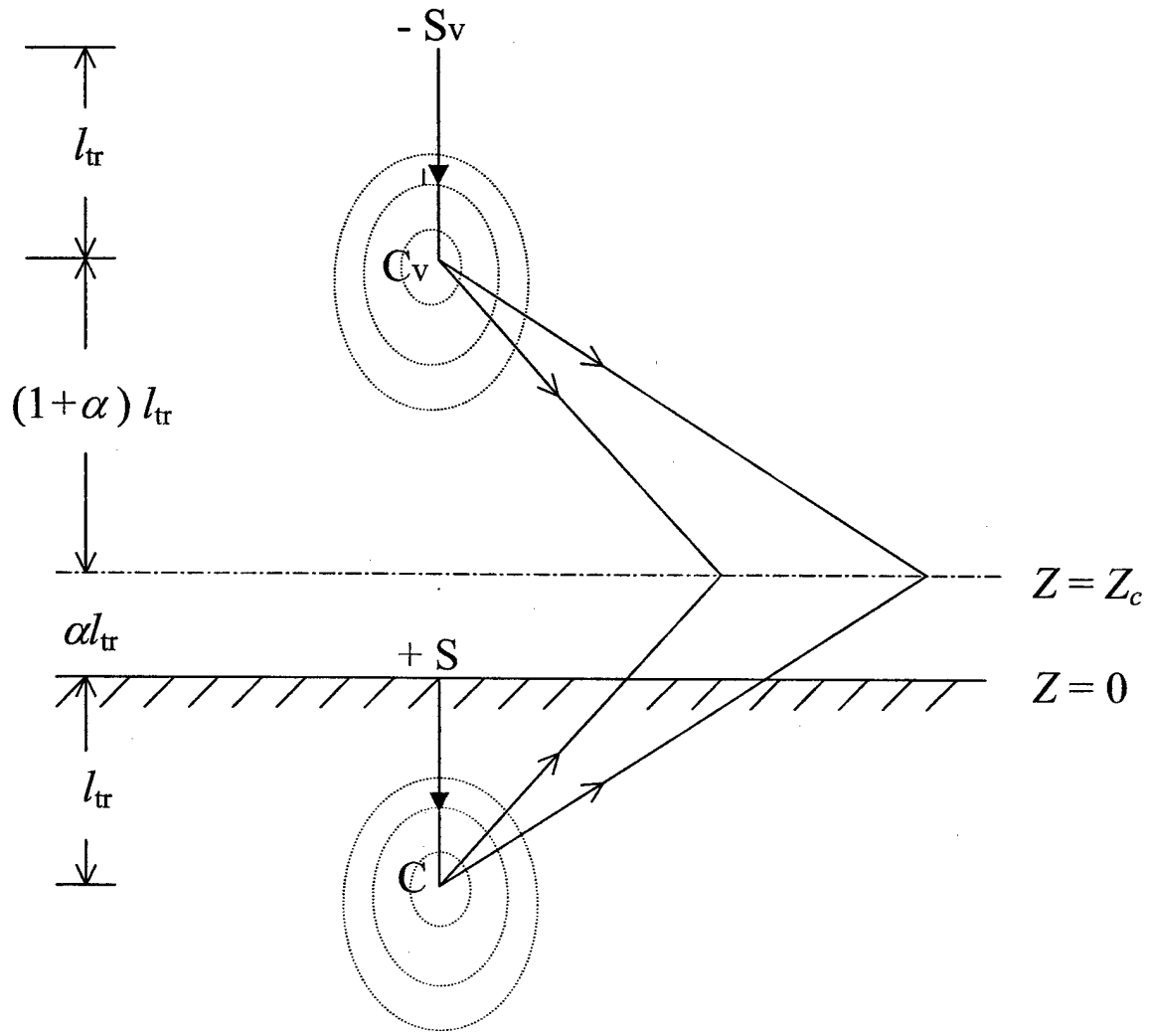

Fig. 3

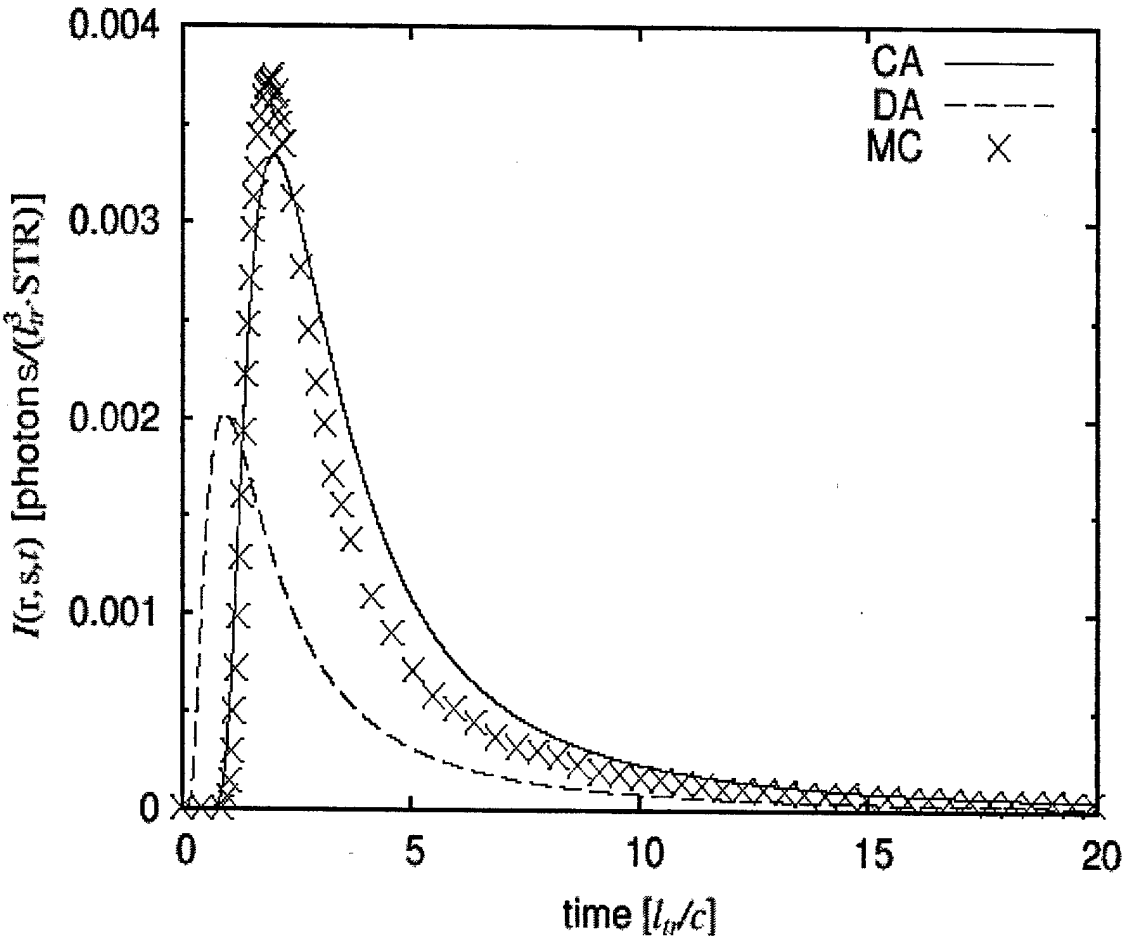
0.004
0.003
0.002
0.001
0
0
5
10
15
20
CA
DA
MC
I(r, s, t) [photons/(l_tr^3·STR)]
time [l_tr/c]

Fig. 4

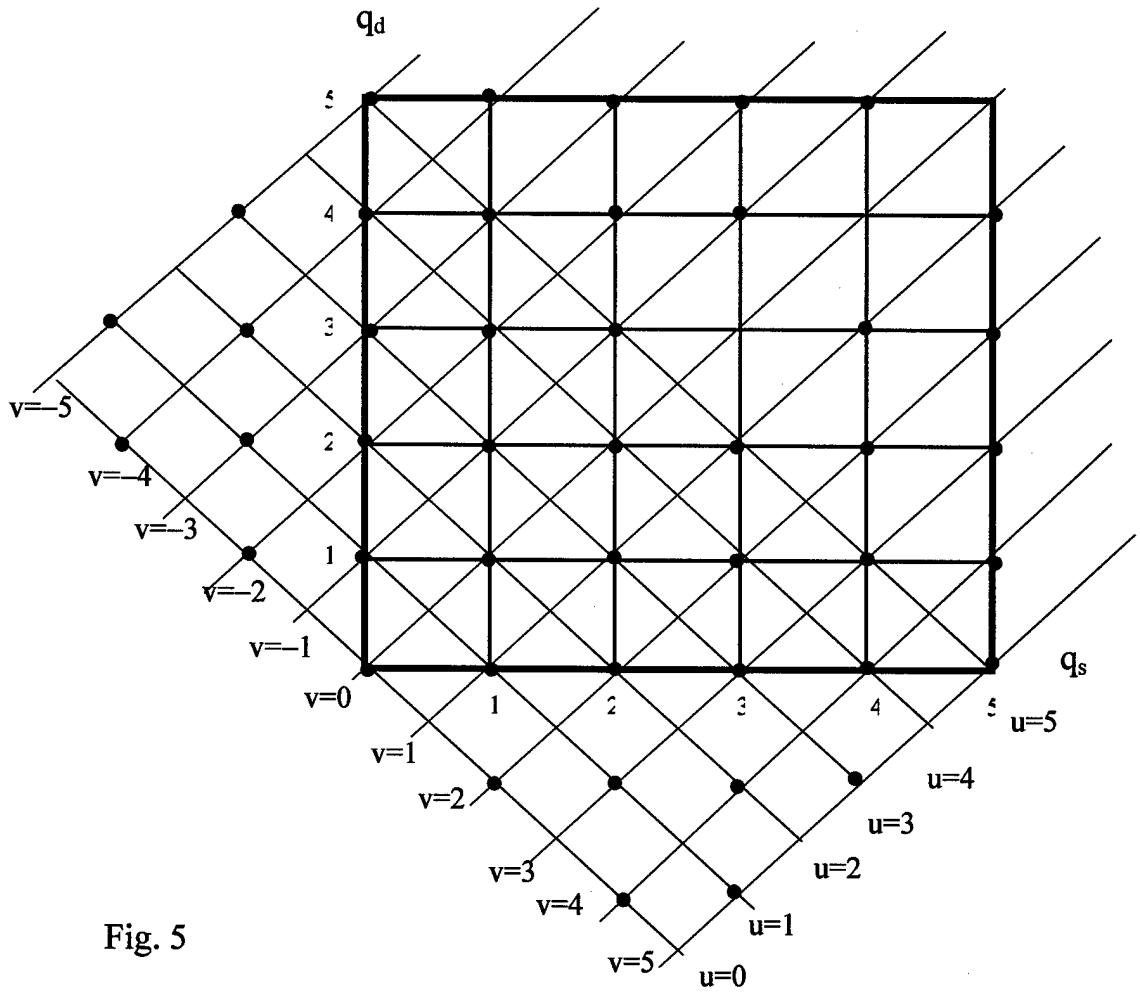

Fig. 5

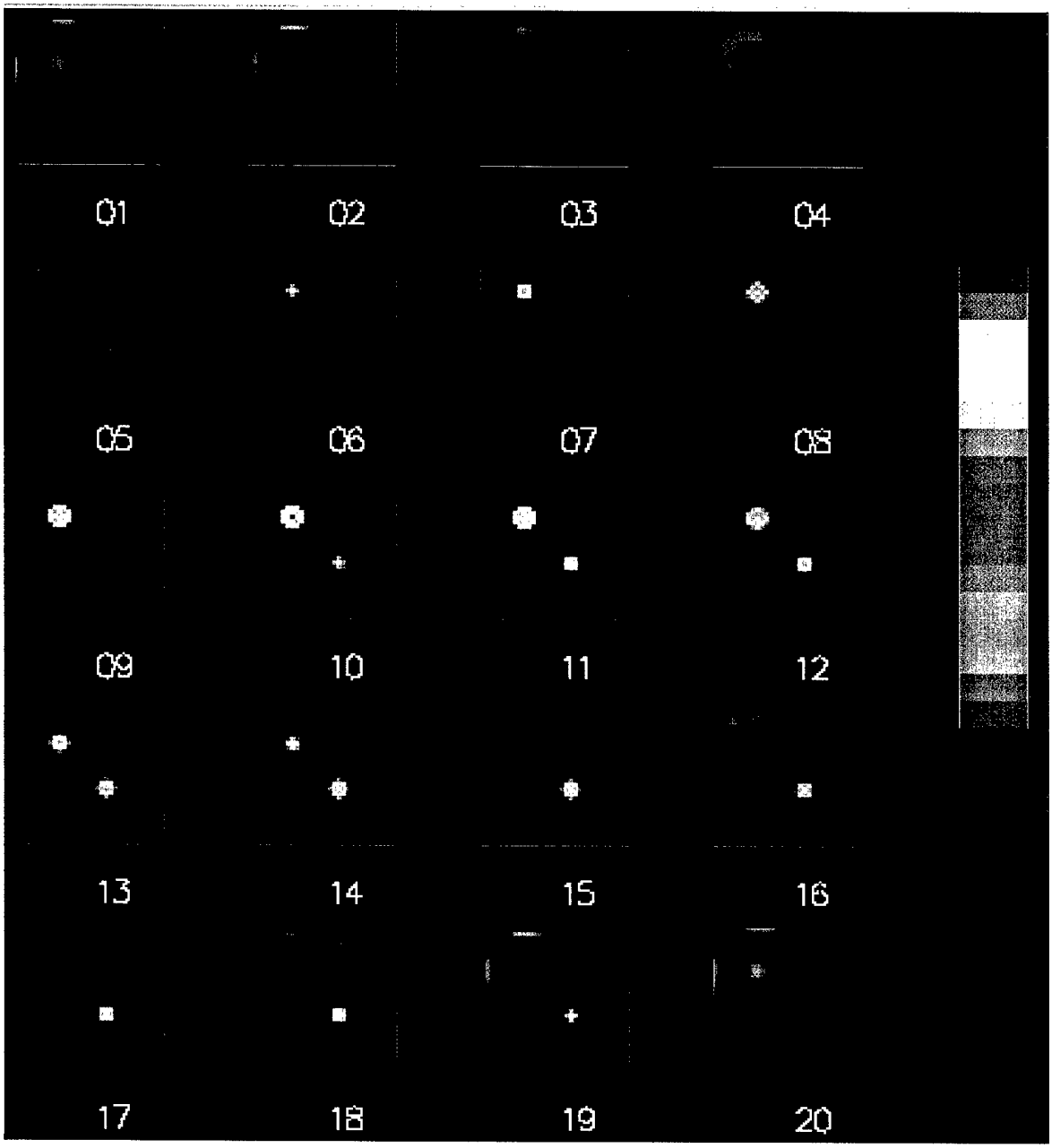

Fig. 6

Anomalous diffraction of light with geometrical path statistics of rays and a Gaussian ray approximation

M. Xu, M. Lax, and R. R. Alfano

Institute for Ultrafast Spectroscopy and Lasers, New York State Center of Advanced Technology for Ultrafast Photonic Materials and Applications and Department of Physics, The City College and Graduate Center of City University of New York, New York, New York 10031

Received August 13, 2002

The anomalous-diffraction theory (ADT) of extinction of light by soft particles is shown to be determined by a statistical distribution of the geometrical paths of individual rays inside the particles. Light extinction depends on the mean and the mean-squared geometrical paths of the rays. Analytical formulas for optical efficiencies from a Gaussian distribution of the geometrical paths of rays are derived. This Gaussian ray approximation reduces to the exact ADT in the intermediate case of light scattering for an arbitrary soft particle and describes well the extinction of light from a system of randomly oriented and (or) polydisperse particles. The implications for probing of the sizes and shapes of particles by light extinction are discussed. © 2003 Optical Society of America

OCIS codes: 290.2200, 290.5850, 290.4020, 280.1310.

Anomalous-diffraction theory (ADT) which was introduced by van de Hulst[1] for light extinction and scattering, is one of the simplest and most powerful approximations of the interaction of electromagnetic radiation with spherical and nonspherical soft particles. This approach has been used in remote sensing of cirrus clouds and climate research, in biophysical and biomedical research, and in other applications.[2] The anomalous-diffraction theory is based on the premise that the extinction of light by a particle is primarily a result of the interference between the rays that pass through the particle with those that do not.[3] This approximation is most applicable to so-called soft particles with the complex relative refractive index m near 1 ($|m - 1| \ll 1$) and with a characteristic dimension of size r exceeding wavelength λ of the incident radiation ($2\pi r/\lambda > 1$) to achieve a high degree of accuracy.[3–6] This accuracy has been observed to improve with softness and nonsphericity,[6] and with polydispersity of the particle.[3]

In this Letter we show that ADT has a statistical interpretation. The extinction of light by particles measures a probability distribution of the geometrical path of the individual rays inside the particles rather than the sizes and shapes of individual particles.

In the framework of ADT,[1] the extinction, absorption, and scattering efficiencies of a particle are given by

$$\begin{aligned} Q_{\text{ext}} &= \frac{2}{P}\,\Re \iint_P \{1 - \exp[-ikl(m_r - 1)] \\ &\quad \times \exp(-klm_i)\}\mathrm{d}P, \\ Q_{\text{abs}} &= \frac{1}{P} \iint_P [1 - \exp(-2klm_i)]\mathrm{d}P, \\ Q_{\text{sca}} &= Q_{\text{ext}} - Q_{\text{abs}}, \end{aligned} \tag{1}$$

where $\Re$ represents the real part, the wave number is $k = 2\pi/\lambda$ for wavelength λ, the complex relative refractive index is $m = m_r - im_i$, l is the geometrical path of an individual ray inside the particle, and P is the projected area of the particle in the plane perpendicular to the incident light over which the integration is performed. The optical efficiencies for a system of randomly oriented and (or) polydisperse particles are averaged over all the sizes and orientations of particles weighted by their projection areas, i.e.,

$$\overline{Q} = \frac{\sum PQ}{\sum P}. \tag{2}$$

The integration in Eq. (1) over the projected area for a single particle at a fixed orientation or the averaging in Eq. (2) over the combined projected area from all sizes and orientations of particles can be reinterpreted as an averaging over a distribution of the geometrical path l of rays. By dividing the (combined) projection area into equal-area elements and counting the resultant geometrical paths that correspond to each projection area element according to their lengths, one can find a probability function $p(l)\mathrm{d}l$ that describes the probability that geometrical path l from a ray is within $(l, l + \mathrm{d}l)$. The probability function is normalized to $\int p(l)\mathrm{d}l = 1$. By this interpretation, we can rewrite the optical efficiencies in Eq. (1) as expected values in accordance with probability distribution $p(l)$ of the geometrical paths of rays. The extinction and absorption efficiencies in Eq. (1) can be expressed as

$$\begin{aligned} Q_{\text{ext}} &= 2\Re \int \{1 - \exp[-ikl(m_r - 1)] \\ &\quad \times \exp(-klm_i)\}p(l)\,\mathrm{d}l, \\ Q_{\text{abs}} &= \int [1 - \exp(-2klm_i)]p(l)\,\mathrm{d}l. \end{aligned} \tag{3}$$

Assume that the geometrical path distribution of rays (in short, the ray distribution) for one particle with a unit size is $p_0(l)$; then the ray distribution for a particle with the same shape, orientation, and a different size L is given by $p(l) = (1/L)p_0(l/L)$ from scaling of

0146-9592/03/030179-03$15.00/0

length. Thus, a system of such particles whose size is distributed according to a probability-density function $n(x)$ has a ray distribution function

$$p_{\mathrm{pol}}(l) = \frac{\int (1/x) p_0(l/x) n(x) x^2 \, \mathrm{d}x}{\int n(x) x^2 \, \mathrm{d}x}, \tag{4}$$

weighted by the projection area of individual particles that is proportional to x^2. The subscript pol or rn is used to denote a polydispersed particle or one that is randomly oriented, respectively.

Let us consider a unit spheroid with a semisize $b = 1$ of the revolutional axis and an axial ratio ϵ and with an angle χ between the propagation direction of the incident beam and the revolutional axis of the spheroid. The geometrical length of a ray and the projection area for such a spheroid have been calculated.[5] The geometrical path distribution of the rays can then be found:

$$p_0(l) = \frac{1}{2}(\epsilon^{-2}\sin^2\chi + \cos^2\chi) l H(l) \times H\left[\frac{2}{(\epsilon^{-2}\sin^2\chi + \cos^2\chi)^{1/2}} - l\right], \tag{5}$$

where $H(x)$ is a Heaviside function. The ray distribution for a system of such spheroids at a fixed orientation χ with a log-normal size distribution,[7]

$$n(x) = \frac{1}{(2\pi)^{1/2}\sigma} r^{-1} \exp\left[-\frac{\ln^2(r/a_m)}{2\sigma^2}\right], \tag{6}$$

is given by

$$p_{\mathrm{pol}}(l) = \frac{(\epsilon^{-2}\sin^2\chi + \cos^2\chi) l}{4} \times \frac{\mathrm{erfc}\{(1/\sqrt{2}\,\sigma)\ln[(\epsilon^{-2}\sin^2\chi + \cos^2\chi)^{1/2} l/2a_m]\}}{{a_m}^2 \exp(2\sigma^2)} \tag{7}$$

from Eq. (4), where $\mathrm{erfc}(x)$ is the complementary error function. The ray distribution becomes

$$p_{\mathrm{pol,rn}}(l) = \frac{\int_0^1 p_{\mathrm{pol}}(l)\pi\epsilon^2(\epsilon^{-2}\sin^2\chi + \cos^2\chi)^{1/2}\mathrm{d}\cos\chi}{\int_0^1 \pi\epsilon^2(\epsilon^{-2}\sin^2\chi + \cos^2\chi)^{1/2}\mathrm{d}\cos\chi} \tag{8}$$

for such particles randomly oriented where the projection area of the cylinder is proportional to $\pi\epsilon^2(\epsilon^{-2}\sin^2\chi + \cos^2\chi)^{1/2}$.[5] It is worth noting here that the ray distribution for a simple spheroid at a fixed orientation [Eq. (5)] is triangular, regardless of the axial ratio of the spheroid. This fundamental geometrical characteristics facilitates a simple rescaling of the radius to calculate the optical efficiencies from a sphere for a spheroid.[5]

The ray distributions from a single spheroid, a single randomly oriented spheroid, a system of polydisperse spheroids at a fixed orientation, and a system of randomly oriented polydisperse spheroids are plotted in Fig. 1. It is clear from the figure that the shape characteristics of an individual particle are washed out by the averaging over the polydispersity and the orientation of the particle. The shape characteristics of an individual particle are expected to be further washed out if particles of different shapes are involved. Thus the ray distribution $p(l)$ of a system of particles such as a bacterial suspension, biological cells, or cirrus clouds where particles are polydisperse, randomly oriented, and (or) of multiple shapes approaches a probability-density function $p(l)$ that is characterized essentially by the mean geometrical path $\langle l\rangle = \int l p(l)\mathrm{d}l$ and the mean-squared geometrical path $\langle l^2\rangle = \int l^2 p(l)\,\mathrm{d}l$ of rays inside the particles. One natural choice of $p(l)$ here is the Gaussian probability-distribution function, which follows the same spirit as the well-known central-limit theorem.[8] We should point out that this choice does not satisfy $p(l < 0) = 0$, but the contribution from near the $l = 0$ region in the ray distribution is much smaller than that from other regions and hence can be ignored.

Let us now assume that the ray distribution is given by a Gaussian distribution:

$$p(x) = \frac{1}{\sqrt{2\pi}\,\sigma} \exp\left[-\frac{(x-\mu)^2}{2\sigma^2}\right]. \tag{9}$$

The extinction and scattering efficiencies are then given by

$$Q_{\mathrm{ext}} = 2 - 2\cos[k(m_r - 1)(\mu - k\sigma^2 m_i)] \times \exp\left[-k\mu m_i - \frac{k^2\sigma^2[(m_r-1)^2 - {m_i}^2]}{2}\right],$$
$$Q_{\mathrm{abs}} = 1 - \exp[-2km_i(\mu - km_i\sigma^2)] \tag{10}$$

from Eqs. (3) after a straightforward integration. The optical efficiencies [Eqs. (10)], in the intermediate case limit [$k(m_r - 1)l \ll 1$ and $km_i l \ll 1$, where l is the geometrical path],[9] reduce to

$$Q_{\mathrm{ext}} = 2km_i\langle l\rangle + k^2[(m_r-1)^2 - {m_i}^2]\langle l^2\rangle,$$
$$Q_{\mathrm{abs}} = 2km_i\langle l\rangle - 2k^2{m_i}^2\langle l^2\rangle,$$
$$Q_{\mathrm{sca}} = k^2|m-1|^2\langle l^2\rangle, \tag{11}$$

where the mean and the mean-squared geometrical paths are given by $\langle l\rangle = \mu$ and $\langle l^2\rangle = \mu^2 + \sigma^2$,

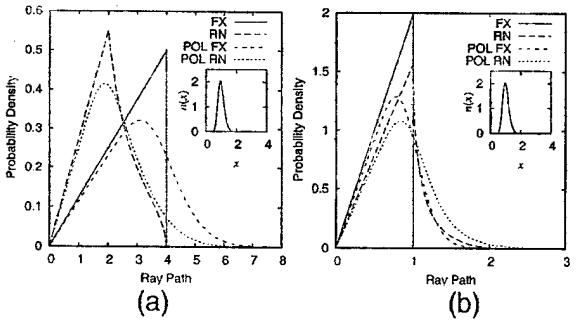

Fig. 1. Ray distributions for a spheroid at a fixed orientation $\chi = 0$ (FX), randomly oriented (RN), polydisperse at a fixed orientation (POL FX), and randomly oriented polydisperse (POL RN). The axial ratio of the spheroid is (a) $\epsilon = 2$ and (b) $\epsilon = 0.5$. Log-normal size distribution $n(x)$ with $a_m = 1$ and $\sigma = 0.2$ is also plotted as insets.

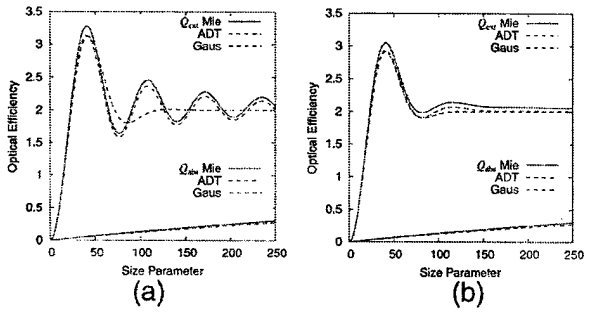

Fig. 2. Extinction and absorption efficiencies of (a) a sphere and (b) a polydisperse sphere with a log-normal radius distribution of $a_m = 1$ and $\sigma = 0.2$ calculated with Mie, ADT, and Gaussian ray approximations. Complex refractive index, $m = 1.05 - i0.0005$. The size distribution has already been shown as insets in Fig. 1.

respectively. These results agree exactly with those for the intermediate region over which the Rayleigh–Gans approximation and the anomalous-diffraction approximation of light scattering from small particles overlap.[1,9] This means that Eqs. (10) from our Gaussian ray approximation reduce to the exact ADT in the intermediate case.

Figure 2 compares the extinction and absorption efficiencies calculated by the exact Mie theory, the exact ADT [Eqs. (1) and (3)], and our Gaussian ray approximation [Eqs. (10)] for a weakly absorbing sphere and a system of the same spheres with a log-normal radius distribution [Eq. (6)] of $a_m = 1$ and $\sigma = 0.2$. Both our Gaussian ray approximation and the ADT, unlike the exact Mie calculation, tend to underestimate the optical efficiencies. This fact is well known.[10,11] The absorption efficiency from our Gaussian ray approximation agrees extremely well with the ADT; at most it differs by 2% from the exact Mie calculation in this comparison. The extinction efficiency agrees well with the exact Mie calculation in the intermediate region for both single spheres and polydisperse spheres, as expected. The Gaussian ray approximation for the polydisperse spheres approaches the exact ADT calculation with maximum relative errors of 3.5% compared to the ADT and of 7% compared to Mie theory.

From our statistical analysis of the anomalous-diffraction theory of light extinction, light extinction depends solely on the probability distribution of the geometrical paths of individual rays inside the particles rather than on the size or the shape of an individual particle. Thus the optical efficiency equivalence[12] can easily be achieved from different-shaped particles or particles of different size distributions as long as they share a common geometrical path distribution of rays.

The geometrical path distribution of rays can be approximated by a Gaussian probability distribution function for a system of particles in which the particles are randomly oriented, polydisperse, and (or) multiple shaped. For such a system of particles the light-extinction measurements essentially determine the mean and the mean-squared geometrical paths of rays from all particles in the system. The shape and size of an individual particle can be deduced only with *a priori* information on the shape and (or) the size distribution of the particles involved. The pursuit of the mean and the mean-squared paths from fitting Eqs. (10) to experimental data, or the general geometrical path distribution of rays $p(l)$ of particles from solving the inverse problem in Eqs. (3), provides an alternative approach to particle sizing and shaping. We note that we have restricted this study to extinction of light from particles of the same type (a common refractive index, m). This statistical interpretation of ADT opens a new way to calculate optical efficiencies of soft particles of different shapes by use of the probability distribution of the geometrical paths of individual rays inside particles.

We thank A. Katz for useful discussions on light scattering from bacterial suspensions. This study is supported in part by the U.S. Department of the Army (grant DAMD17-02-1-0516). The U.S. Army Medical Research Acquisition Activity, 820 Chandler Street, Fort Detrick, Maryland 21702-5014 is the awarding and administering acquisition office. Additional support is given by the U.S. Department of Defense (grants DAMD01-0084 and DAMD98-8147). M. Xu's e-mail address is minxu@sci.ccny.cuny.edu.

References

1. H. C. van de Hulst, *Light Scattering by Small Particles* (Dover, New York, 1981).
2. M. I. Mishchenko, J. W. Hovenier, and L. D. Travis, eds., *Light Scattering by Nonspherical Particles: Theory, Measurements, and Applications* (Academic, San Diego, Calif., 1999).
3. S. A. Ackerman and G. L. Stephens, J. Atmos. Sci.**44,** 1574 (1987).
4. W. A. Farone and M. J. I. Robinson, Appl. Opt.**7,** 643 (1968).
5. F. D. Bryant and P. Latimer, J. Colloid Interface Sci. **30,** 291 (1969).
6. Y. Liu, W. P. Arnott, and J. Hallett, Appl. Opt.**37,** 5019 (1998).
7. J. F. Hansen and L. D. Travis, Space Sci. Rev.**16,** 527 (1974).
8. M. G. Kendall, *Kendall's Advanced Theory of Statistics* (Oxford U. Press, Oxford, 1999).
9. P. Chýlek and J. Li, Opt. Commun.**117,** 389 (1995).
10. C. F. Bohren and D. R. Huffman, *Absorption and Scattering of Light by Small Particles* (Wiley, New York, 1983).
11. A. A. Kokhanovsky, *Optics of Light Scattering Media: Problems and Solutions* (Wiley, New York, 1999).
12. L. E. Paramonov, Opt. Spektrosk.**77,** 660 (1994).

Three dimensional hybrid-dual-Fourier tomography in turbid media using multiple sources and multiple detectors

M. Xu, W. Cai and R. R. Alfano

Institute for Ultrafast Spectroscopy and Lasers,

New York State Center of Advanced Technology for Ultrafast

Photonic Materials and Applications,

and Department of Physics,

The City College and Graduate Center of City University of New

York, New York, NY 10031

We have developed a hybrid-dual-Fourier tomographic algorithm for a fast 3D image reconstruction in turbid media using multiple sources and multiple detectors. This algorithm can be applied to different forward models based on a diffusion approximation[1] or a cumulant analytical solution of the radiative transfer equation[2,3] in CW, frequency-, and time-domains as long as the translational invariance in the lateral direction exists. It provides a general scheme of fast numerical three-dimensional image reconstruction using multiple sources and detectors and is different from previous diffraction tomography approaches.[1,4]

By scanning a point source on the grids of the input plane of a slab, the measured light intensity $I(\rho_d, \rho_s)$ on a detector array on the exit plane of the slab may form a 4D data set where ρ_d and ρ_s are the coordinates on the input and exit plane. An additional dimension of the data set may be added in frequency-modulated or time-resolved measurements.[4,5] Based on the general properties of the translational invariance along the lateral direction, a dual two dimensional Fourier transform on both lateral coordinates of the detector ρ_d and the source ρ_s is applied to the intensity data set.

A hybrid transform is then performed on the spatial frequencies to rotate the coordinate system in the Fourier space. This data rearrangement results in an inversion problem in the form of:

$$\Delta I(\mathbf{u}, \mathbf{v}, z_d, z_s) = \int dz W(\mathbf{u}, \mathbf{v}, z, z_d, z_s) X(\mathbf{u}, z) \tag{1}$$

in which ΔI is the change of intensity in the rotated Fourier space $(\mathbf{u}, \mathbf{v})$, W is the weight function and X is the Fourier quantity of the absorption and/or scattering deviation from the uniform background. The integral is performed on the axial coordinate z of the inhomogeneity, and z_d and z_s are the axial coordinates of the detector and the source.

The reconstruction is then performed for each fixed value of the spatial frequency $\mathbf{u}$ in Eq. (1). A series of such a one dimensional inversion over the axial coordinate z is carried out to obtain the Fourier quantity $X(\mathbf{u}, z)$ for each $\mathbf{u}$. The inverse Fourier transform of $X(\mathbf{u}, z)$ provides a three dimensional reconstruction of the inhomogeneities in the turbid medium.

The major advantage of this approach is its speed and tolerance to noise. The reduction of the image reconstruction to a series of one dimensional inverse problem of the dimension of the number of discrete divisions in the axial direction from our data rearrangement very much reduces the complexity of the image reconstruction problem. The number of operations required increases only linearly with the total number of detector-source pairs. A complete reconstruction of a $32 \times 32 \times 20$ volume is within few minutes using a 1GHz CPU. The tolerance to noise, in particular, the additive noise is achieved due to the different spatial frequency spectrum of the signal and the noise. It is straightforward in the Fourier space to filter out noise which usually appears in higher frequency components.

We will present the reconstruction results for a CW and a time-resolved reconstruction of a slab with a thickness of 40mm and a similar optical property of a human breast. We will also discuss in detail the reconstruction algorithm, especially, the choice of the regularization parameters for Eq. (1) from a statistical analysis of the reconstruction procedure. The merit of applying this algorithm to

CW, time- and frequency-domains for imaging will also be discussed.

This work is supported by US Army Medical Command. One of the author (M. Xu) thanks the support of the Department of the Army (Grant# DAMD17-02-0516).

References

1. X. D. Li, T. Durduran, and A. G. Yodh, "Diffraction tomography for biomedical imaging with diffuse-photon density waves," Opt. Lett. **22,** 573–575 (1997).

2. W. Cai, M. Lax, and R. R. Alfano, "Cumulant solution of the elastic Boltzmann transport equation in an infinite uniform medium," Phys. Rev. E **61,** 3871–3876 (2000).

3. M. Xu, W. Cai, M. Lax, and R. R. Alfano, "A photon transport forward model for imaging in turbid media," Opt. Lett. **26,** 1066–1068 (2001).

4. J. C. Schotland and V. A. Markel, "Inverse scattering with diffusing waves," J. Opt. Soc. Am. A **18,** 2767–2777 (2001).

5. M. Xu, M. Lax, and R. R. Alfano, "Time-resolved Fourier optical diffuse tomography," J. Opt. Soc. Am. A **18,** 1535–1542 (2001).

Nonlinear multiple passage effects on optical imaging of an absorption inhomogeneity in turbid media

M. Xu, W. Cai and R. R. Alfano

Institute for Ultrafast Spectroscopy and Lasers,
New York State Center of Advanced Technology for Ultrafast Photonic Materials and Applications,
and Department of Physics,
The City College and Graduate Center of City University of New York, New York, NY 10031

ABSTRACT

We report on the effect of the nonlinear multiple passage on optical imaging of an absorption inhomogeneity of finite size deep inside a turbid medium based on a cumulant solution to radiative transfer. An analytical expression for the nonlinear correction factor is derived. Comparison to Monte Carlo simulations reveals an excellent agreement. The implication on optical imaging is discussed.

Keywords: nonlinear correction, multiple passage, radiative transfer, optical imaging

1. INTRODUCTION

The principle of optical imaging of turbid media (such as tissues) is to locate and reconstruct the optical properties (absorption and scattering coefficients) of embedded inhomogeneities (such as tumor) in the hope of identification by inverting the difference in time-resolved or frequency-modulated photon transmittance due to the presence of the inhomogeneities through either iterative or noniterative methods. The key quantity involved is the weight function which quantifies the influence on the detected signal due to the change of the optical parameters of the medium. The diffusion approximation to radiative transfer provides an adequate model for the weight function (or Jacobian) for a small and weak absorption inhomogeneity far away from both the source and the detector. However, the weight function predicted by the linear perturbation approaches is no longer valid when the absorption strength is not small.[1] This can be attributed to the multiple passage of a photon through one single abnormal site.

The change of the light intensity ΔI at the detector $\mathbf{r}_d$ due to the presence of an absorption site at $\mathbf{r}$ from a modulated point source at $\mathbf{r}_s$ is expressed as

$$\Delta I = -\delta\mu_a V G(\mathbf{r}_d, \omega|\mathbf{r}) G(\mathbf{r}, \omega|\mathbf{r}_s) \tag{1}$$

to the first order of Born approximation where $\delta\mu_a$ is the excess absorption of the absorption site whose volume is V, ω is the modulation frequency of light, and G is the propagator of photon migration in the background medium. Here, the Green's function $G(\mathbf{r}_2, \omega|\mathbf{r}_1)$, in general, depends on the detail of light scattering inside the medium, and the incident and outgoing directions of light.

When the absorption strength is not small ($\delta\mu_a V \not\ll 1$), photon loss due to multiple passage of the absorption site is appreciable and can not be ignored. The expression for ΔI in Eq. (1) needs to be modified to include the contributions from multiple visits of the site by the photon. Fig. (1) illustrates the most important correction (a "self-energy" correction) which takes into account the repeated visits made by a photon to the site up to an infinite times.

Further author information: (Send correspondence to M. Xu)
M. Xu: Email: minxu@sci.ccny.cuny.edu

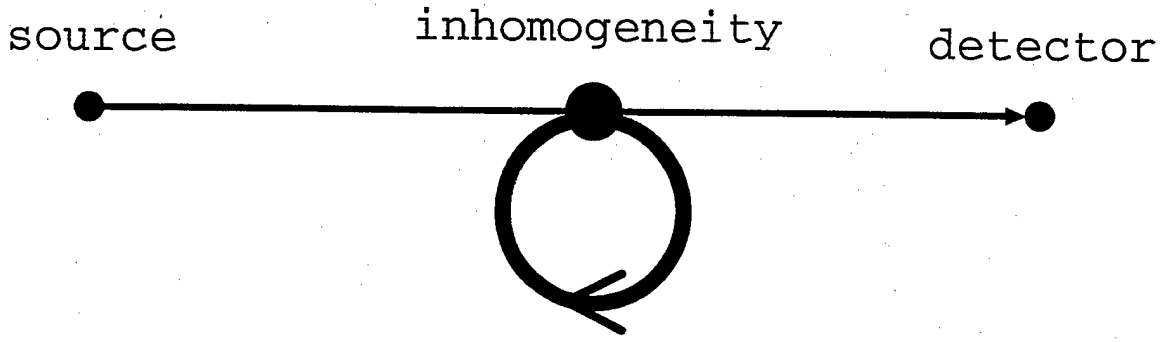

Figure 1. Self-energy correction to the multiple passage effect on light absorption.

Assuming that the center of the absorption site is located at $\bar{\mathbf{r}}$ and far away from both the source and the detector, the change of the detected light, ΔI, is now given by

$$\begin{aligned} \Delta I &= -G(\mathbf{r}_d,\omega|\bar{\mathbf{r}})V\delta\mu_a(\bar{\mathbf{r}})\sum_{n=0}^{\infty}\left[-\bar{N}_{\text{self}}(\omega;R)V\delta\mu_a(\bar{\mathbf{r}})\right]^n G(\bar{\mathbf{r}},\omega|\mathbf{r}_s) \\ &= -G(\mathbf{r}_d,\omega|\bar{\mathbf{r}})\frac{V\delta\mu_a(\bar{\mathbf{r}})}{1+\bar{N}_{\text{self}}(\omega;R)V\delta\mu_a(\bar{\mathbf{r}})}G(\bar{\mathbf{r}},\omega|\mathbf{r}_s) \end{aligned} \tag{2}$$

where

$$\bar{N}_{\text{self}}(\omega;R) = \frac{1}{V^2}\int_V\int_V G(\mathbf{r}_2,\omega|\mathbf{r}_1)d^3\mathbf{r}_2 d^3\mathbf{r}_1 \tag{3}$$

is the self-propagator which describes the probability that a photon revisits the volume V of size R. Here $G(\mathbf{r}_d,\omega|\bar{\mathbf{r}})$ and $G(\bar{\mathbf{r}},\omega|\mathbf{r}_s)$ are well modelled by the center-moved diffusion model as long as the separations $|\mathbf{r}_d-\bar{\mathbf{r}}|, |\mathbf{r}_s-\bar{\mathbf{r}}| \gg l_t$ where l_t is the transport mean free path of light in the medium.[2] However, the diffusion Green's function can not be used in Eq. (3) to evaluate $\bar{N}_{\text{self}}(\omega;R)$ where $\mathbf{r}_1$ is in the proximity of $\mathbf{r}_2$. By comparing Eq. (2) to Eq. (1), the nonlinear multiple passgage effect of an absorption site can be summarized by the nonlinear correction factor $\left[1+\bar{N}_{\text{self}}(\omega;R)V\delta\mu_a(\bar{\mathbf{r}})\right]^{-1}$. This factor serves as a universal measure of the nonlinear multiple passage effect as long as the absorption site is far away from both the source and the detector and its size is much smaller than its distance to both the source and the detector.

In this article, we will derive an analytical expression for the self-propagator to understand the nonlinear multiple passage effect on light absorption using our cumulant solution to radiative transfer. The nonlinear correction factor $\left[1+\bar{N}_{\text{self}}(\omega;R)V\delta\mu_a(\bar{\mathbf{r}})\right]^{-1}$ of our result is shown to be in an excellent agreement with the Monte Carlo simulations for continuous wave light.

2. THEORY

To take into account the higher order contributions from the absorption inhomogeneity, the behavior of the photon migration in a short distance must be considered. Although the photon distribution is almost isotropic at an absorption site deep inside the medium, the diffusion approximation is still not appropriate here. The separation between the two points $\mathbf{r}_1$ and $\mathbf{r}_2$ within the volume in Eq. (3) is small. The photon propagator $N(\mathbf{r}_2,t|\mathbf{r}_1,\mathbf{s})$, which represents the probability that a photon propagates

from position $\mathbf{r}_1$ with propagation direction $\mathbf{s}$ to position $\mathbf{r}_2$ in time t, when $\mathbf{r}_2$ is in the proximity of $\mathbf{r}_1$, is governed by the radiative transfer equation rather than the diffusion equation.

Recently we have shown that the propagation of photon inside a turbid medium (the radiative transfer equation) can be solved analytically using a cumulant expansion of the photon distribution function.[3] The propagation of photon was found to transform from an initial ballistic motion at early time and then gradually to a center-adjusted diffusion at later time. The propagator of photon density (the Green's function) in an infinite uniform medium is given by[4]

$$N(\mathbf{r},t|\mathbf{r}_0,\mathbf{s}_0) = \frac{1}{[4\pi D(t)t]^{3/2}} \exp\left[-\frac{(\mathbf{r}-\mathbf{r}_0-\mathbf{s}_0\Delta(t))^2}{4D(t)t} - \mu_a t\right] \tag{4}$$

ignoring the small difference in the diffusion coefficient along different directions where the absorption coefficient is μ_a, the time-dependent diffusion coefficient is

$$D(t) = \frac{l_t^2}{3t}\left\{\frac{ct}{l_t} - [1-\exp(-ct/l_t)] - \frac{1}{2}[1-\exp(-ct/l_t)]^2\right\} \tag{5}$$

and

$$\Delta(t) = l_t[1-\exp(-ct/l_t)] \tag{6}$$

is the average center of photons which moves with speed c initially and approaches the transport mean free path l_t in the long time limit. The Green's function for parallel geometries can be obtained by the method of image sources.[5]

2.1. Propagator of an isotropic point source

Let's now consider the propagator $N(\mathbf{r},t|\mathbf{r}_0,\mathbf{s}_0)$ at the inhomogeneity site $\mathbf{r}_0 = \mathbf{0}$ (the origin of space) deep inside the medium. The photon distribution at $\mathbf{r}_0$ is almost isotropic but is *anisotropic* scattering. The effective propagator can then be obtained by averaging (4) over the propagation direction $\mathbf{s}_0$ of light over the 4π solid angle, and is given by [see Appendix A]

$$\begin{aligned} N_{\text{eff}}(r,t) &= \frac{1}{4\pi}\int d^2\mathbf{s}_0 N(\mathbf{r},t|\mathbf{r}_0,\mathbf{s}_0) = \frac{\exp(-\mu_a t)}{(4\pi)^{3/2}(D(t)t)^{1/2}r\Delta(t)} \\ &\quad\times\left\{\exp\left[-\frac{(r-\Delta(t))^2}{4D(t)t}\right] - \exp\left[-\frac{(r+\Delta(t))^2}{4D(t)t}\right]\right\}. \end{aligned} \tag{7}$$

This reduces to

$$N_{\text{eff}}(r,t) = \frac{\exp(-\mu_a t)}{4\pi r^2}\delta(r-ct), \quad \text{for } t\to 0^+ \tag{8}$$

and

$$N_{\text{eff}}(r,t) = \frac{\exp(-\mu_a t)}{(4\pi)^{3/2}(D_\infty t)^{1/2}r l_t}\left\{\exp\left[-\frac{(r-l_t)^2}{4D_\infty t}\right] - \exp\left[-\frac{(r+l_t)^2}{4D_\infty t}\right]\right\}, \quad \text{for t} \gg 1 \tag{9}$$

in early and late time limits where $D_\infty \equiv l_t c/3$.

The temporal Fourier transforms of the asymptotic equations (8) and (9) are given by

$$N_{\text{eff}}(\mathbf{r},\omega) = \frac{1}{4\pi r^2 c}\exp\left[(i\omega-\mu_a)\frac{r}{c}\right] \tag{10}$$

and

$$N_{\text{eff}}(\mathbf{r},\omega) = \frac{1}{8\pi D r \kappa l_t}\left[\exp(-\kappa\,|r-l_t|) - \exp(-\kappa(r+l_t))\right] \tag{11}$$

respectively, where $\kappa \equiv \sqrt{3(\mu_a - i\omega)/l_t c}$ whose sign is chosen with a nonnegative real part. In the limit of small $\kappa \ll 1$, Eq. (11) simplifies to

$$\lim_{\kappa\to 0} N_{\text{eff}}(\mathbf{r},\omega) = \begin{cases} \frac{1}{4\pi D_\infty l_t} & r < l_t \\ \frac{1}{4\pi D_\infty r} & r \geq l_t \end{cases} . \tag{12}$$

This is the case, for example, that a continuous wave propagates in a nonabsorbing medium. The errornous divergence at the zero separation in the diffuse Green's function

$$G(r,\omega) = \frac{\exp(-\kappa r)}{4\pi D_\infty r} \tag{13}$$

is removed in our formulation of the propagation of an isotropic point source.

The asymptotic equation (11) from the late time limit provides a good approximation for $N_{\text{eff}}(r,\omega)$ when $r > l_t$ [see Fig. (2)]. The contribution to $N_{\text{eff}}(r,\omega)$ when $r < l_t$ is from either ballistic or diffusive photons, hence an improvement to Eq. (10) can be made

$$N_{\text{eff}}(r,\omega) \simeq \frac{1}{4\pi r^2 c}\exp\left[(i\omega - \mu_a)\frac{r}{c}\right] + \frac{\exp(-\kappa l_t)}{4\pi D_\infty r \kappa l_t}\sinh(\kappa r), \quad r < l_t \tag{14}$$

to include the contribution from diffusive photons. The effective propagator in temporal Fourier space $N_{\text{eff}}(r,\omega=0)$ and its asymptotic behaviors (10), (11) and (14) are shown in Fig. (2). The diffusion Green's function has a huge error for small r.

2.2. Self propagator for a finite volume

For an absorption site of a finite volume V deep inside the medium, say a sphere of radius $R \ll L$ where L is the dimension of the medium, the self-propagator $\bar{N}_{\text{self}}(t;R)$ for this volume which denotes a photon revisits the site in time t is written as:

$$\begin{aligned} \bar{N}_{\text{self}}(t;R) &= \frac{1}{V^2}\int_V\int_V N_{\text{eff}}(|\mathbf{r}_2 - \mathbf{r}_1|, t) d^3\mathbf{r}_1 d^3\mathbf{r}_2 \\ &= \frac{1}{V}\int_0^{2R} N_{\text{eff}}(r,t)\gamma_0(r) 4\pi r^2 dr \end{aligned} \tag{15}$$

where

$$\gamma_0(r) = 1 - \frac{3r}{4R} + \frac{1}{16}\left(\frac{r}{R}\right)^3 \tag{16}$$

is the characteristic function for a uniform sphere.[6–8] This characteristic function has a form of

$$\gamma_0(r) = 1 - (S/4V)r + \ldots \tag{17}$$

for an arbitrary particle where S is the surface area of the particle. This self propagator (15) for a finite volume is quite different from the self-propagator of a point, obtained by setting $r = 0$ in (4) or (7), i.e.,

$$N_{\text{eff}}(0,t) = \frac{\exp(-\mu_a t)}{(4\pi D(t)t)^{3/2}}\exp\left[-\frac{\Delta(t)^2}{4D(t)t}\right], \quad (t > 0). \tag{18}$$

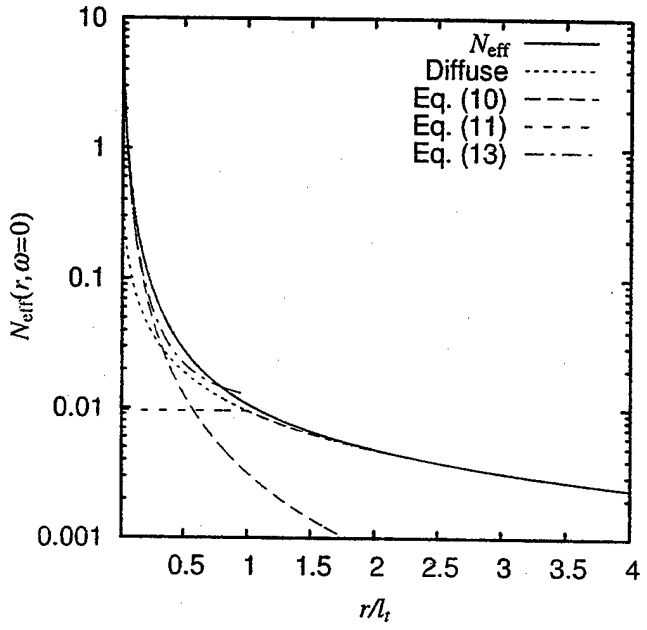

Figure 2. The effective propagator in temporal Fourier space $N_{\rm eff}(r,\omega=0)$ for photon migration in a nonabsorbing medium. Its approximations by (14) when $r < l_t$ and by Eq. (11) when $r > l_t$ are also plotted. The diffusion Green's function has a huge error for small r.

See Fig. (3). This difference comes from the fact that Eq. (15) includes the contribution from the ballistic motion of the photon when the photon flies across the site while Eq. (18) does not contain this effect. The former manifests itself in Fig. (3a) as the linear decay of $N_{\rm seff}(t;R)V$ in the form of $\gamma_0(ct)$ near the origin.

The self-propagator in temporal Fourier space is thus obtained by a temporal Fourier transform of (15):

$$\begin{aligned}\tilde{N}_{\rm self}(\omega;R) &= \int_{0+}^{+\infty} \tilde{N}_{\rm self}(t;R)\exp(i\omega t)dt \\ &= \frac{1}{V}\int_0^{2R} dr\gamma_0(r)4\pi r^2 \int_0^{+\infty} dt N_{\rm eff}(r,t)\exp(i\omega t) \\ &= \frac{1}{V}\int_0^{2R} N_{\rm eff}(r,\omega)\gamma_0(r)4\pi r^2 dr.\end{aligned} \tag{19}$$

The lower limit of integration is 0^+, emphasizing that $t=0$ should be excluded from integration. Note $\lim_{t\to 0+}\tilde{N}_{\rm eff}(r,t)=0$ for our cumulant photon density function. This is not the case for the diffusion Green's function. A numerical quadrature is generally required to compute this self propagator (19). A crude estimation of $\tilde{N}_{\rm self}(\omega;R)$ can be obtained from the asymptotic behavior (11) and (14) of $N_{\rm eff}(r,\omega)$, i.e.,

$$\begin{aligned}\tilde{N}_{\rm seff}(\omega;R) \simeq\ & \frac{1}{V}\int_0^{\min(2R,l_t)} \frac{1}{4\pi r^2 c}\exp\left[(i\omega-\mu_a)\frac{r}{c}\right]\gamma_0(r)4\pi r^2 dr \\ & +\frac{1}{V}\int_0^{2R}\frac{1}{8\pi D_\infty r\kappa l_t}\left[\exp(-\kappa|r-l_t|)-\exp(-\kappa(r+l_t))\right]\gamma_0(r)4\pi r^2 dr.\end{aligned} \tag{20}$$

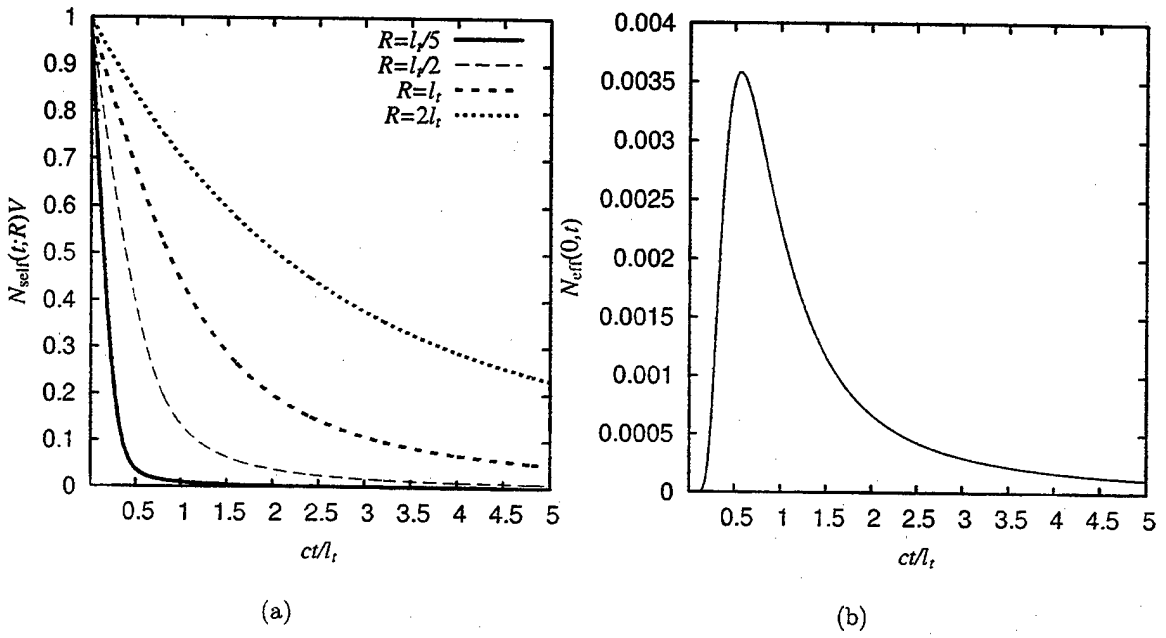

Figure 3. The self-propagators for a finite volume and a point: (a) $N_{\text{self}}(t;R)$ and (b) $N_{\text{eff}}(\mathbf{0},t)$.

This reduces to

$$\bar{N}_{\text{self}}(\omega=0;R)=\frac{1}{V}\begin{cases}\frac{3R}{4c}+\frac{R^3}{l_t^2c} & R\le l_t/2\\ \frac{384R^5+160l_t^2R^3-60l_t^3R^2+3l_t^5}{320R^3l_tc} & R>l_t/2\end{cases} \tag{21}$$

for a continuous wave propagating inside a nonabsorbing medium ($\omega=\mu_a=\kappa=0$). This estimation turns out to be amazingly good. Fig. (4) plots $\bar{N}_{\text{self}}(\omega=0;R)$ from numerical quadrature and the crude estimation (21).

3. RESULTS AND DISCUSSION

The multiple passage effect due to the absorption site can now be computed using the self-propagator Eq. (19) derived here. For large sites, the self-propagator $\bar{N}_{\text{self}}(\omega=0;R)$ increases inverse proportional to its size ($\bar{N}_{\text{self}}\propto R^{-1}$) from Eq. (21); hence the nonlinear correction factor has a form of

$$\frac{1}{1+\bar{N}_{\text{self}}(\omega;R)V\delta\mu_a(\bar{\mathbf{r}})}\simeq\left(1+\frac{6\delta\mu_a}{5l_tc}R^2\right)^{-1}, \tag{22}$$

dependent on the area of the absorption site for large R.

Monte Carlo methods have been extensively used in simulation of photon migration.[9,10] We perform Monte Carlo simulations on a uniform nonabsorbing and isotropic scattering slab (the anisotropic factor of scattering $g=0$). The units of length of time are chosen such that the mean scattering length $l_s=1/\mu_s=1$ and the speed of light $c=1$. The transport mean free path is hence $l_t=1$ and the thickness of the slab is assumed $L=80l_t$. An absorption spherical site is located at the center of the slab $(0,0,L/2)$ with radius R whose absorption and scattering coefficients are $\mu_{a2}=\delta\mu_a=0.01$

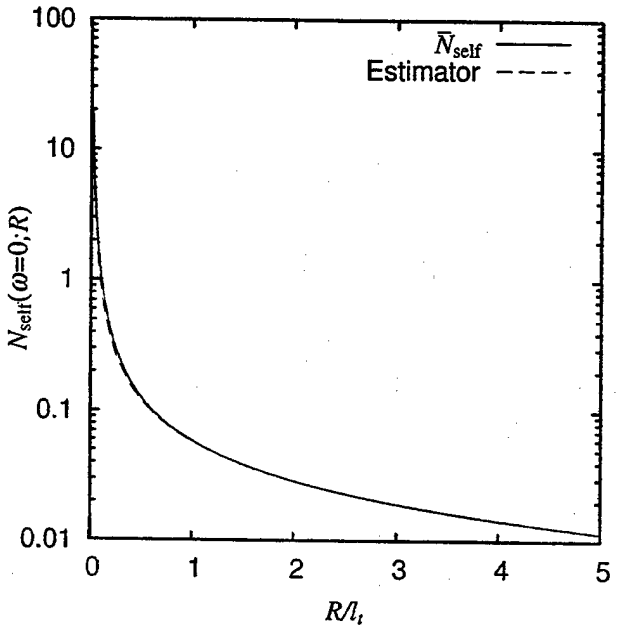

Figure 4. The self propagator $\bar{N}_{\rm self}(\omega = 0; R)$ and its estimator. The diffusion self-propagator for continuous waves is also plotted.

and $\mu_{s,2} = \mu_s$ respectively. The photon is incident at the origin on the left boundary of the slab $z = 0$ in the normal direction of the surface. Each photon is traced until it escapes the slab through either the left or the right boundary. The correlated sampling is used in simulation to reduce variance. A single simulation is used to compute the emitted photon density I_0 for the uniform background (nonabsorption slab) and I for the slab with the absorption site present.

The nonlinear correction factor $[1 + \bar{N}_{\rm self}(\omega; R)V\delta\mu_a(\bar{\mathbf{r}})]^{-1}$ in Eq. (22) can be extracted from the change of the detected light intensity due to the presence of the absorption site in Monte Carlo simulations according to Eq. (2). Fig. (5) plots the theoretical nonlinear correction factor and that from Monte Carlo simulations. "Back" and "Forward" denote the cases where light emits from the left (z=0) and the right ($z = L$) boundaries, respectively. The agreement between our theoretical result and Monte Carlo simulations is excellent except for extremely small sizes of inhomogeneities.

Figs. (6) and (7) plot the nonlinear correction factor versus the variation of the modulation frequency of light for a fixed absorption strength and versus the size of the absorption site with a fixed modulation frequency of light respectively. With the increase of the modulation frequency of light, the nonlinear correction becomes less accentuated. The dependence on the size of the inhomogeneity is no longer monotonic for modulated light while the nonlinear correction factor decreases monotonically with the increase of the size for continuous wave light. The phase delay is in the order of a few degrees in the cases investigated.

The typical value of the absorption coefficient of human tissues is around 0.001ps^{-1} while the scattering coefficient is about 1ps^{-1}. Hence the absorption and scattering ratio is in the order of 0.001. This should be compared to our results listed here where the corresponding ratio is 0.01 and one order of magnitude stronger. The nonlinear correction factor for absorption inhomogeneities such as tumors in human tissues is not appreciable unless the size of the inhomogeneity is $R \sim 5l_t$ or larger.

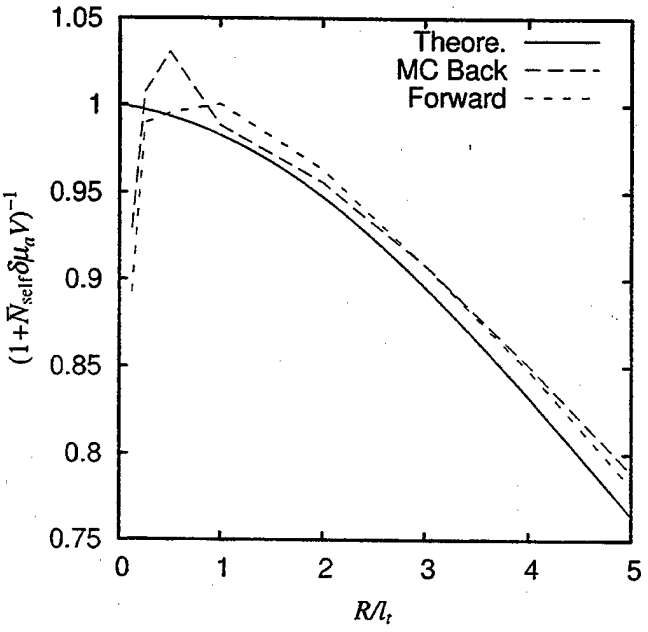

Figure 5. The nonlinear correction factor from the theoretical self-propagator Eq. (19) and Monte Carlo simulations. "Back" and "Forward" denote light emitting from the left (z=0)and the right ($z = L$) boundaries. The excess absorption is $\delta\mu_a = 0.01$.

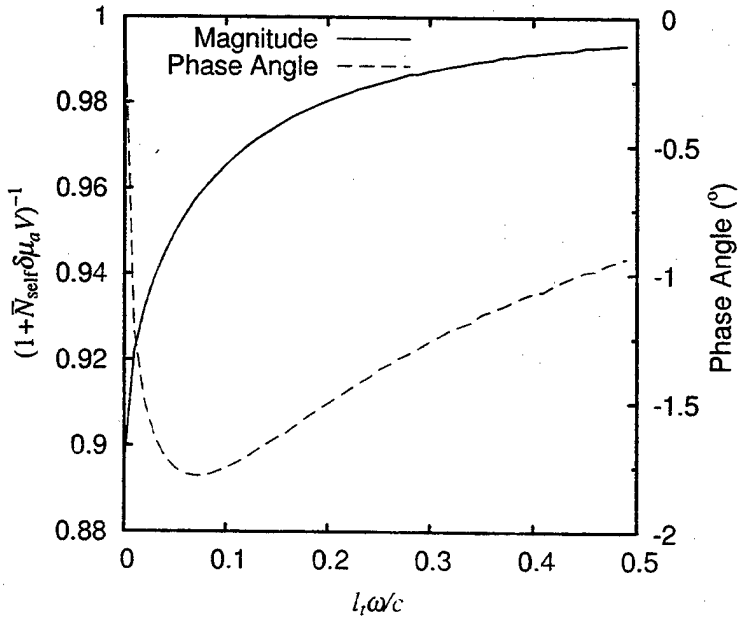

Figure 6. The nonlinear correction factor versus the variation of the modulation frequency of light. The size of the absorption sphere is $R = 3l_t$. The excess absorption is $\delta\mu_a = 0.01$.

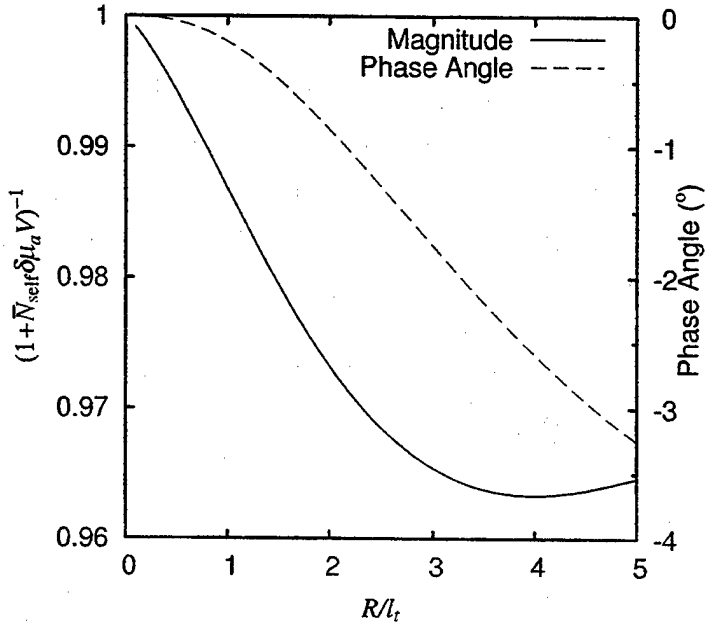

Figure 7. The nonlinear correction factor versus the variation of the size of the absorption site. The modulation frequency of light is $\omega = 0.1$. The excess absorption is $\delta\mu_a = 0.01$.

In conclusion, we have derived an analytical expression for the nonlinear correction factor which agrees well with Monte Carlo simulations. The effect of the nonlinear multiple passage of an absorption site on optical imaging only becomes appreciable when the size of the inhomogeneity is $5l_t$ or larger for human tissues.

APPENDIX A. DERIVATION OF $N_{\mathrm{EFF}}(R,T)$

The spatial Fourier transform of (4) is given by

$$N(\mathbf{k},t|\mathbf{r}_0,\mathbf{s}_0) = \int d^3\mathbf{r}\exp(-i\mathbf{k}\cdot\mathbf{r})N(\mathbf{r},t|\mathbf{r}_0,\mathbf{s}_0) = \exp\left(-k^2D(t)t - \mu_a t - i\mathbf{k}\cdot\mathbf{s}_0\Delta(t)\right). \quad (23)$$

Hence, the effective propagator in spatial Fourier space at $\mathbf{r}_0$ is expressed as

$$N_{\mathrm{eff}}(\mathbf{k},t) = \frac{1}{4\pi}\int d^2\mathbf{s}_0 N(\mathbf{k},t|\mathbf{r}_0,\mathbf{s}_0) = \exp\left(-k^2D(t)t - \mu_a t\right)\frac{\sin(k\Delta(t))}{k\Delta(t)} \quad (24)$$

by averaging (23) over the propagation direction $\mathbf{s}_0$ of light over the 4π solid angle. The effective propagator in real space is then obtained by an inverse spatial Fourier transform of (24):

$$\begin{aligned} N_{\mathrm{eff}}(\mathbf{r},t) &= \int \frac{d^3\mathbf{k}}{(2\pi)^3}\exp(i\mathbf{k}\cdot\mathbf{r})\exp\left(-k^2D(t)t - \mu_a t\right)\frac{\sin(k\Delta(t))}{k\Delta(t)} \\ &= \frac{\exp(-\mu_a t)}{(4\pi)^{3/2}(D(t)t)^{1/2}r\Delta(t)}\left\{\exp\left[-\frac{(r-\Delta(t))^2}{4D(t)t}\right] - \exp\left[-\frac{(r+\Delta(t))^2}{4D(t)t}\right]\right\} \\ &= \frac{2\exp(-\mu_a t)}{(4\pi)^{3/2}(D(t)t)^{1/2}r\Delta(t)}\exp\left[-\frac{r^2+\Delta(t)^2}{4D(t)t}\right]\sinh\frac{r\Delta(t)}{2D(t)t}. \end{aligned} \quad (25)$$

ACKNOWLEDGMENTS

This work is partly supported by US Army Medical Research and Materiels Command, NASA IRA, and CUNY organized research programs. One of the authors (M. Xu) thanks the support by the Department of Army (Grant# DAMD17-02-1-0516). The U. S. Army Medical Research Acquisition Activity, 820 Chandler Street, Fort Detrick MD 21702-5014 is the awarding and administering acquisition office.

REFERENCES

1. S. Carraresi, T. S. M. Shatir, F. Martelli, and G. Zaccanti, "Accuracy of a perturbation model to predict the effect of scattering and absorbing inhomogeneities on photon migration," *Appl. Opt.* **40**, pp. 4622–4632, Sept. 2001.
2. M. Xu, W. Cai, M. Lax, and R. R. Alfano, "A transport model for optical tomography in turbid media," in *Signal Recovery and Synthesis*, OSA, 2001.
3. W. Cai, M. Lax, and R. R. Alfano. "Cumulant solution of the elastic Boltzmann transport equation in an infinite uniform medium," *Phys. Rev. E* **61**(4-A), pp. 3871–3876, 2000.
4. M. Xu, W. Cai, M. Lax, and R. R. Alfano, "A photon transport forward model for imaging in turbid media," *Opt. Lett.* **26**(14), pp. 1066-1068, 2001.
5. M. Xu, W. Cai, M. Lax, and R. R. Alfano, "Photon migration in turbid media using a cumulant approximation to radiative transfer," *Phys. Rev. E* **65**, p. 066609, 2002.
6. G. Porod, "Die röntgenkleinwinkelstreuung von dichtgepackten kolloiden systemen i," *Kolloid-Z.* **124**, pp. 83–114, 1951.
7. G. Porod, "Die röntgenkleinwinkelstreuung von dichtgepackten kolloiden systemen ii," *Kolloid-Z.* **125**, pp. 51–57, 109–122, 1952.
8. A. Guinier, G. Fournet, C. B. Walker, and K. L.Yudowitch, *Small-angle scattering of X-rays*, John Wiley & Sons, New York, 1955.
9. A. Sassaroli, C. Blumetti, F. Martelli, L. Alianelli, D. Contini, A. Ismaelli, and G. Zaccanti, "Monte Carlo procedure for investigating light propagation and imaging of highly scattering media," *Appl. Opt.* **37**, pp. 7392-7400, Nov. 1998.
10. M. Testorf, U. sterberg, B. Pogue, and K. Paulsen, "Sampling of time- and frequency-domain signals in monte carlo simulations of photon migration," *Appl. Opt.* **38**, pp. 236–245, January 1999.

Noise Analysis and Image Reconstruction in Three-dimensional Optical Diffraction Tomography

M. Xu, W. Cai, and R. R. Alfano

Institute for Ultrafast Spectroscopy and Lasers,

New York State Center of Advanced Technology for Ultrafast Photonic Materials and Applications,

and Department of Physics,

The City College and Graduate Center of City University of New York, New York, NY 10031

minxu@sci.ccny.cuny.edu

Proper modeling of noise and appropriate regularization is required to stabilize optical image reconstruction for biomedical imaging and diagnostics. We consider the effect of the Poisson noise inherent in photon counts on image reconstruction using a generalized Tikhonov regularization formalism. An explicit regularized inversion formula to this problem is derived for a three-dimensional optical diffraction tomography using multiple sources and detectors. The regularization parameter is linked directly to the prior signal to noise ratio. Computer simulation results demonstrate improvement in the quality of reconstruction from our algorithm over algorithms not modeling the Poisson noise properly.

OCIS codes: 170.3010 170.3880 100.3190 170.6920 290.7050

IUSL#-2002-12 Appl. Opt. Special Issue on Biomedical Imaging

1. Introduction

Over the past decade, the study of optical image reconstruction for biomedical imaging and diagnostics has attracted considerable attention due to in part its potential for noninvasive clinical applications.[1–3] Near-infrared light can probe the internal structure (absorption and scattering coefficients) of a highly-scattering turbid medium such as human tissues by measuring scattered light around the medium. The propagation of light in turbid media is governed by the radiative transfer equation.[4] Approximations based on truncation in the spherical harmonic expansion[5] or cumulant expansion of the photon distribution function[6,7] are used in image reconstruction. However, the numerical reconstruction is extremely complicated and computational expensive even after approximation and linearization of the forward problem.

One of the recent developments in optical tomography is to apply Fourier technique to analyze the light propagation in turbid media (so called "optical diffraction tomography"). Diffraction tomography may be traced back to Emil Wolf's original work of determination of the spatial distribution of the refractive index from measurements of the intensity transmission functions of holograms.[8,9] Diffraction tomography has been extensively applied to imaging using ultrasound and microwave.[10–12] Recently there are considerable effort to apply this diffraction technique to tomographic imaging using diffuse photons;[13–15] in particular, Schotland and Markel's work.[16,17] The benefit of the diffraction formalism of optical imaging comes from the diagonalization of the point spread function (the Green's function) in the spatial Fourier space in presence of a translational invariance, yielding a significant simplification in

reconstruction.

Since light is highly scattered inside the turbid medium and very different spatial distributions of the optical property in the medium may result in indistinguishable observations, the reconstruction of the internal structure from scattered light based on a forward model formulated in either the real space or the Fourier space (diffraction tomography) is not unique and hence ill-posed.[18] The inevitable photon counting noise accentuates this problem further. A common practice is to add regularization to stabilize the inversion process.

One of the most popular regularization methods was proposed by Tikhonov.[19] Describe an imaging of a set of measurements $\mathbf{b}$ due to an internal structure $\mathbf{f}$ of a medium as:

$$A\mathbf{f} + \mathbf{n} = \mathbf{b} \tag{1}$$

in a framework of a linearized reconstruction where $\mathbf{n}$ is the noise involved in measurement. Tikhonov seeks a best possible solution to Eq. (1) by solving an optimization problem

$$\min_{\mathbf{f}} \left\{ \|A\mathbf{f} - \mathbf{b}\|^2 + \lambda^2 \|L\mathbf{f}\|^2 \right\} \tag{2}$$

which balances the goodness of fit (the first term) and the closeness to the prior information (the second term). Here, λ is the regularization parameter which determines the trade-off and L is a penalty operator which draws the solution toward its null space (chosen to approximate the prior information).[20]

An assumption of white noise in all the observations at one common level is implicit in Eq. (2) whereas the noise presented in photon counting tends to be Poisson

and position-dependent, proportional to the square root of light intensity at each detecting element in the shot-noise limit. Intuitively, regularization should consider both the noise presented in observation and the prior information of the object.

We will show in this paper a proper modeling of the noise improves the quality of reconstruction. A generalized Tikhonov regularization formalism is used in image reconstruction to incorporate both the prior information and the noise. Furthermore, the optimal regularization parameter will be shown linked directly to the prior signal to noise ratio (PSNR).

This paper is organized as following. We will first review the diffraction tomography using diffuse photons. We present an explicit regularized inversion formula for diffraction image reconstruction after discussion of a generalized Tikhonov regularization method. Computer simulation results are shown to demonstrate improvement of the quality of reconstruction by the new inversion formula using time-resolved data with realistic noise added for reconstruction of a planar geometry using multiple sources and detectors.

2. Theory

A. Optical diffuse diffraction tomography

The formalism for diffuse diffraction tomography has been given by various authors in time- and frequency- domains.[13,15–17] Follow the Dirac notation used by Markel and Schotland,[16] diffraction formalism of the optical imaging using diffuse photons is

reviewed here. The diffusion equation in time domain is

$$\partial_t |u(t)\rangle + H |u(t)\rangle = |S(t)\rangle \tag{3}$$

where $|u\rangle$ is the energy density, the Hamiltonian $H = -\nabla \cdot D(\mathbf{r})\nabla + \alpha(\mathbf{r})$, $D(\mathbf{r})$ and $\alpha(\mathbf{r})$ are the position-dependent diffusion and absorption coefficients, and $|S\rangle$ is the source power density. This is the Schrodinger equation in imaginary time where $\alpha(\mathbf{r})$ can be interpreted as the interaction potential and $D(\mathbf{r})$ as the inverse of the position-dependent mass. The evolution operator (the Green's function) is given by

$$G = \Theta(t) \exp(-Ht) \tag{4}$$

where $\Theta(t)$ is the Heaviside step function.

It is best to regard the diffusion equation (3) as an equation in a Hilbert space and a basis of position $\mathbf{r}$ and time t is used in Eq. (3). Some other commonly used basis include the temporal frequency ω and the lateral spatial frequency $\mathbf{q}$. The rotation from one basis to another can be facilitated using the following identities

$$\int |t\rangle\, dt\, \langle t| = \int |\omega\rangle \frac{d\omega}{2\pi} \langle\omega| = \int |\boldsymbol{\rho}\rangle\, d^2\boldsymbol{\rho}\, \langle\boldsymbol{\rho}| = \int |\mathbf{q}\rangle \frac{d^2\mathbf{q}}{(2\pi)^2} \langle\mathbf{q}| = 1 \tag{5}$$

$$\langle\omega|t\rangle = \exp(i\omega t), \quad \langle\mathbf{q}|\boldsymbol{\rho}\rangle = \exp(-i\mathbf{q}\cdot\boldsymbol{\rho})$$

due to the closure property of the respective basis.

In one class of problems, the position-dependent diffusion and absorption coeffi-

cients $D(\mathbf{r})$ and $\alpha(\mathbf{r})$ can be decomposed to $D(\mathbf{r}) = D_0 + \delta D(\mathbf{r})$ and $\alpha(\mathbf{r}) = \alpha_0 + \delta\alpha(\mathbf{r})$ where $\delta D(\mathbf{r})$ and $\delta\alpha(\mathbf{r})$ can be regarded as a perturbation to the values D_0 and α_0 of a uniform background. The scattered field, i.e., the perturbation of the energy density, due to the embedded inhomogeneities $\delta D(\mathbf{r})$ and $\delta\alpha(\mathbf{r})$, is given by

$$\phi_s = \phi - \phi_0 = G\,|u\rangle - G_0\,|u\rangle = -G_0 \Delta H G_0\,|u\rangle \tag{6}$$

to the first order Born approximation where ϕ_0 is the energy density from unperturbed uniform background, ϕ is the total energy density from the perturbed medium, and $\Delta H = -\nabla \cdot \delta D(\mathbf{r}) \nabla + \delta\alpha(\mathbf{r})$.

Let's restrict ourselves to a planar geometry which possesses a translational invariance along the lateral directions. The Green's function of a uniform planar geometry has a form of

$$\langle \boldsymbol{\rho} z t | G_0 | \boldsymbol{\rho}' z' t' \rangle = \Theta(t-t') \frac{1}{4\pi D_0 (t-t')} \exp\left[-\frac{(\boldsymbol{\rho} - \boldsymbol{\rho}')^2}{4 D_0 (t-t')} - \alpha_0 (t-t') \right] G_z(z, z', t-t') \tag{7}$$

where G_z is the axial component of the Green's function and dependent on the specific boundary condition. Its diffraction counterpart is given by

$$\begin{aligned} \langle \mathbf{q} z t | G_0 | \mathbf{q}' z' t' \rangle &= \int \langle \mathbf{q} | \boldsymbol{\rho} \rangle \, d^2\boldsymbol{\rho} \, \langle \boldsymbol{\rho} z' t | G_0 | \boldsymbol{\rho}' z' t' \rangle \, d^2\boldsymbol{\rho}' \, \langle \boldsymbol{\rho}' | \mathbf{q}' \rangle \\ &= \Theta(t-t') \exp\left[-(Dq^2 + \alpha)(t-t') \right] G_z(z, z', t-t') (2\pi)^2 \delta(\mathbf{q} - \mathbf{q}') \\ &\equiv G_0(\mathbf{q}, z, z', t-t') (2\pi)^2 \delta(\mathbf{q} - \mathbf{q}') \end{aligned} \tag{8}$$

by changing the basis $\boldsymbol{\rho}$ to $\mathbf{q}$ in time domain. The benefit of a diffraction formalism with the lateral spatial frequency $\mathbf{q}$ is now clear that the Green's function is diagonal with respect to the basis and has a most simple formulation.

The scattered field is then expressed as:

$$\phi_s(\mathbf{q}_d, \mathbf{q}_s, t-t_0) = -\int_{t_0}^{t} d\tau \int dz G_0(\mathbf{q}_d, z_d, z, t-\tau) \langle \mathbf{q}_d z\tau | \Delta H | \mathbf{q}_s z\tau \rangle G_0(\mathbf{q}_s, z, z_s, \tau - t_0) \tag{9}$$

from Eq. (6) using the identities (5) due to an incident "point" source $|\mathbf{q}_s z_s\rangle \, \delta(t-t_0)$. The operator $\langle \mathbf{q}_d z\tau | \Delta H | \mathbf{q}_s z\tau \rangle$ can be further evaluated in a similar fashion using (5). This results in[15]

$$\phi_s(\mathbf{q}_d, \mathbf{q}_s, t-t_0) = -\int dz \left[\kappa_A(\mathbf{q}_d, \mathbf{q}_s, z) \delta\alpha(\mathbf{q}_d - \mathbf{q}_s, z) + \kappa_D(\mathbf{q}_d, \mathbf{q}_s, z) \delta D(\mathbf{q}_d - \mathbf{q}_s, z) \right] \tag{10}$$

where the weight function for absorption and diffusion inhomogeneities is given by

$$\begin{aligned} \kappa_A &= \int_{t_0}^{t} d\tau G(\mathbf{q}_d, z_d, z, t-\tau) G(\mathbf{q}_s, z, z_s, \tau - t_0) \\ \kappa_D &= \int_{t_0}^{t} d\tau \left[\frac{\partial G(\mathbf{q}_d, z_d, z, t-\tau)}{\partial z} \frac{\partial G(\mathbf{q}_s, z, z_s, \tau - t_0)}{\partial z} \right. \\ &\quad \left. + \mathbf{q}_s \cdot \mathbf{q}_d G(\mathbf{q}_d, z_d, z, t-\tau) G(\mathbf{q}_s, z, z_s, \tau - t_0) \right]. \end{aligned} \tag{11}$$

After performing a variable change,

$$\begin{aligned} \mathbf{q}_d &= \mathbf{p} + \mathbf{q}/2 \\ \mathbf{q}_s &= \mathbf{p} - \mathbf{q}/2 \end{aligned} \tag{12}$$

the forward problem can be rewritten as an integral equation

$$\phi_s(\mathbf{p}+\mathbf{q}/2,\mathbf{p}-\mathbf{q}/2)=\int dz\,[\kappa_A(\mathbf{p},\mathbf{q},z)\delta\alpha(\mathbf{q},z)+\kappa_D(\mathbf{p},\mathbf{q},z)\delta D(\mathbf{q},z)] \qquad (13)$$

up to a constant multiplier (-1 here). The equation (13) defined an independent integral equation of $\delta\alpha(\mathbf{q},z)$ and $\delta D(\mathbf{q},z)$ for each fixed $\mathbf{q}$ in the form of Eq. (1). The corresponding result in frequency domain is obtained replacing the integral over time by a factor $2\pi\delta(\omega_d-\omega_s)$ and changing $t-\tau$ and $\tau-t_0$ to ω_d and ω_s respectively, which had been given in Markel and Schotland.[16]

The formal inversion formula for Eq. (13) with a fixed $\mathbf{q}$ is given by

$$\begin{aligned}\delta\alpha(\mathbf{q},z) &= \int d^2\mathbf{p}'dz'\,\langle z|T^{-1}(\mathbf{q})|z'\rangle\,\kappa_A^*(\mathbf{p}',\mathbf{q},z')\phi(\mathbf{p}'+\mathbf{q}/2,\mathbf{p}'-\mathbf{q}/2) \qquad (14)\\ \delta D(\mathbf{q},z) &= \int d^2\mathbf{p}'dz'\,\langle z|T^{-1}(\mathbf{q})|z'\rangle\,\kappa_D^*(\mathbf{p}',\mathbf{q},z')\phi(\mathbf{p}'+\mathbf{q}/2,\mathbf{p}'-\mathbf{q}/2)\end{aligned}$$

where

$$\langle z|T(\mathbf{q})|z'\rangle=\int d^2\mathbf{p}\,[\kappa_A^*(\mathbf{p},\mathbf{q},z)\kappa_A(\mathbf{p},\mathbf{q},z')+\kappa_D^*(\mathbf{p},\mathbf{q},z)\kappa_D(\mathbf{p},\mathbf{q},z')]\,. \qquad (15)$$

This can be verified by substitution of Eq. (14) into Eq. (13). This is the Moore-Penrose generalized inverse of the linear system (13).[21]

The incident Fourier "point" source $|\mathbf{q}_s z_s\rangle\,\delta(t-t_s)$ in time domain or $|\mathbf{q}_s z_s\omega_s\rangle$ in frequency domain can be generated from a spatially modulated mask under illumination of a plane wave, or by Fourier transform of an array of point sources.

A scheme is given in Fig. (1) where a point source scans grid by grid covering the input window and the emitted light on the exit window is captured by a CCD camera in a planar geometry.

We proceed to provide a regularized version of the above solution (14) after introduction of a generalized Tikhonov regularization method.

B. Generalized Tikhonov regularization

The inverse problem of the form of Eq. (1) is ubiquitous and regularization is usually required to stabilize the inverse process. As we have pointed out in the introduction, the standard Tikhonov regularization scheme assumes implicitly an uniform distribution of white noise in all observations which contradicts with the position-dependent noise of photon counting from detecting elements in optical imaging.

An intuitive way of dealing the inverse problem Eq. (1) is to regard $\mathbf{f}$, $\mathbf{n}$ and $\mathbf{b}$ as a realization of Gaussian weak random variables f, n and b in the Hilbert space $L^2(\mathbb{R})$.[22] A Gaussian weak random variable is uniquely determined by its mean element and covariance operator. Under the assumptions that f and n have zero mean and uncorrelated, and that the covariance operator R_{nn} has a bounded inverse, the best linear estimate of f, namely $C_0\mathbf{b}$, which minimizes the mean square error, was shown by Viano et. al.[23] as

$$C_0 = R_{ff}A^*(AR_{ff}A^* + R_{nn})^{-1} \tag{16}$$

where a superscript "$*$" means hermitian and the covariance is defined as $R_{xy} =$

$\mathrm{E}\{[x-\mathrm{E}(x)]\,[y-\mathrm{E}(y)]^*\}$. This formula is derived by minimizing the mean square error and closely connected with the Kalman filter theory.[24] It is easy to verify that C_0 can be rewritten in a more familiar form:

$$C_0 = (A^* R_{nn}^{-1} A + R_{ff}^{-1})^{-1} A^* R_{nn}^{-1}. \tag{17}$$

Let's introduce:

$$\begin{aligned} R_{nn} &= \sigma^2 V, \quad \mathrm{trace}(V) = 1 \\ R_{ff} &= \tau^2 (L^* L)^{-1}, \quad \mathrm{trace}((L^* L)^{-1}) = 1 \end{aligned} \tag{18}$$

where σ and τ can be interpreted as the magnitudes of the noise and the prior signal respectively. Eq. (17) yields

$$C_0 = (A^* V^{-1} A + \frac{\sigma^2}{\tau^2} L^* L)^{-1} A^* V^{-1}. \tag{19}$$

The linear estimate $C_0\mathbf{b}$ is now recognized as the solution of a generalized Tikhonov regularization problem:[25]

$$\underset{\mathbf{f}}{\mathrm{argmin}} \left\{ (A\mathbf{f}-\mathbf{b})^* V^{-1} (A\mathbf{f}-\mathbf{b}) + \frac{\sigma^2}{\tau^2} \|L\mathbf{f}\|^2 \right\}. \tag{20}$$

Moreover, the choice of the regularization parameter $\lambda = \sigma/\tau$ must be optimal for this inverse problem with the prescribed noise covariance and prior information (18) since $C_0\mathbf{b}$ is the best estimator. The standard Tikhonov regularization responds to

the case where $V = I$ where I is an identity matrix. The penalty term is commonly set also to an identity matrix in the standard Tikhonov regularization.[25]

This shows that the inverse of the optimal regularization parameter λ^*:

$$1/\lambda^* = \mathrm{PSNR} = \tau/\sigma = \sqrt{\frac{\mathrm{trace}\,(R_{ff})}{\mathrm{trace}\,(R_{nn})}} \tag{21}$$

is linked directly to the prior signal to noise ratio (PSNR). The value of the optimal regularization parameter is proportional to the magnitude of the noise and inverse proportional to the magnitude of the prior signal. Note PSNR is different from the conventional signal to noise ratio (SNR) which usually means the ratio of magnitudes of noiseless observation to noise.

C. Noise analysis and regularized diffraction reconstruction

Measurements captured by the CCD camera on the exit window is noise contaminated. The noise is Poisson with its variance given by $\mathrm{Var}\,[n(\boldsymbol{\rho}_d, \boldsymbol{\rho}_s)] = b(\boldsymbol{\rho}_d, \boldsymbol{\rho}_s)$ in the shot noise limit. Here we have assumed the detector element has a *unit* size one and $b(\boldsymbol{\rho}_d, \boldsymbol{\rho}_s)$ is the count of photons on the $\boldsymbol{\rho}_d$ detecting element from a point source at $\boldsymbol{\rho}_s$. The covariance of the noise in our Fourier space is thus

$$\begin{aligned} R_{n(\mathbf{q}_d,\mathbf{q}_s)n(\mathbf{q}'_d,\mathbf{q}'_s)} &= \mathrm{E}\left[\langle \mathbf{q}_d|n|\mathbf{q}_s\rangle\,\overline{\langle \mathbf{q}'_d|n|\mathbf{q}'_s\rangle}\right] - \mathrm{E}\left[\langle \mathbf{q}_d|n|\mathbf{q}_s\rangle\right]\mathrm{E}\left[\overline{\langle \mathbf{q}'_d|n|\mathbf{q}'_s\rangle}\right] \\ &= \int d^2\boldsymbol{\rho}_d d^2\boldsymbol{\rho}_s \exp\left[-i(\mathbf{q}_d - \mathbf{q}'_d)\cdot\boldsymbol{\rho}_d + i(\mathbf{q}_s - \mathbf{q}'_s)\cdot\boldsymbol{\rho}_s\right]\mathrm{Var}\left[n(\boldsymbol{\rho}_d, \boldsymbol{\rho}_s)\right] \\ &= \langle \mathbf{q}_d - \mathbf{q}'_d|b|\mathbf{q}_s - \mathbf{q}'_s\rangle\,, \end{aligned} \tag{22}$$

assuming that the noise at different pixels and from different sources is independent.

One important consequence of this noise covariance (22) is that the noise covariance

$$R_{nn}(\mathbf{q}) = R_{n(\mathbf{q}_d,\mathbf{q}_s)n(\mathbf{q}'_d,\mathbf{q}'_s)}, \quad \text{where } \mathbf{q}_d - \mathbf{q}_s = \mathbf{q}'_d - \mathbf{q}'_s = \mathbf{q} \tag{23}$$

in one subspace of a fixed $\mathbf{q}$ is circulant and symmetric. This yields

$$\langle \mathbf{p}|R_{nn}(\mathbf{q})|\mathbf{p}'\rangle = \int \langle \mathbf{p}|\boldsymbol{\rho}\rangle \, d^2\boldsymbol{\rho} \, \langle \boldsymbol{\rho}|\Lambda|\boldsymbol{\rho}'\rangle \, d^2\boldsymbol{\rho}' \, \langle \boldsymbol{\rho}'|\mathbf{p}'\rangle \tag{24}$$

where

$$\langle \boldsymbol{\rho}|\Lambda|\boldsymbol{\rho}'\rangle = Sb(\boldsymbol{\rho},\mathbf{0})\delta(\boldsymbol{\rho}-\boldsymbol{\rho}') \tag{25}$$

is diagonal. The inverse of $R_{nn}(\mathbf{q})$ is then simply given by

$$\langle \mathbf{p}|R^{-1}_{nn}(\mathbf{q})|\mathbf{p}'\rangle = \int \langle \mathbf{p}|\boldsymbol{\rho}\rangle \, d^2\boldsymbol{\rho} \, \langle \boldsymbol{\rho}|\Lambda^{-1}|\boldsymbol{\rho}'\rangle \, d^2\boldsymbol{\rho}' \, \langle \boldsymbol{\rho}'|\mathbf{p}'\rangle \tag{26}$$

where

$$\langle \boldsymbol{\rho}|\Lambda^{-1}|\boldsymbol{\rho}'\rangle = S^{-1}b^{-1}(\boldsymbol{\rho},\mathbf{0})\delta(\boldsymbol{\rho}-\boldsymbol{\rho}'). \tag{27}$$

This can be easily verified by evaluating $\int \langle \mathbf{p}|R_{nn}(\mathbf{q})|\mathbf{p}'\rangle \frac{d^2\mathbf{p}'}{(2\pi)^2} \langle \mathbf{p}'|R^{-1}_{nn}(\mathbf{q})|\mathbf{p}''\rangle = \langle \mathbf{p}|\mathbf{p}''\rangle$.

The generalized Tikhonov reconstruction of our formal solution (14) can now be

regularized to

$$\begin{aligned}
\delta\alpha(\mathbf{q},z) &= \int d^2\mathbf{p}'d^2\mathbf{p}''dz' \left\langle z|T_{\text{reg}}^{-1}(\mathbf{q})|z'\right\rangle \kappa_A^*(\mathbf{p}',\mathbf{q},z') \left\langle \mathbf{p}'|R_{nn}^{-1}(\mathbf{q})|\mathbf{p}''\right\rangle \phi(\mathbf{p}''+\mathbf{q}/2,\mathbf{p}''-\mathbf{q}/2) \\
\delta D(\mathbf{q},z) &= \int d^2\mathbf{p}'d^2\mathbf{p}''dz' \left\langle z|T_{\text{reg}}^{-1}(\mathbf{q})|z'\right\rangle \kappa_D^*(\mathbf{p}',\mathbf{q},z') \left\langle \mathbf{p}'|R_{nn}^{-1}(\mathbf{q})|\mathbf{p}''\right\rangle \phi(\mathbf{p}''+\mathbf{q}/2,\mathbf{p}''-\mathbf{q}/2)
\end{aligned} \tag{28}$$

from Eq. (19) where

$$\begin{aligned}
\left\langle z|T_{\text{reg}}(\mathbf{q})|z'\right\rangle = \int d^2\mathbf{p}d^2\mathbf{p}' \big[&\kappa_A^*(\mathbf{p},\mathbf{q},z) \left\langle \mathbf{p}|R_{nn}^{-1}(\mathbf{q})|\mathbf{p}'\right\rangle \kappa_A(\mathbf{p}',\mathbf{q},z') + \\
&\kappa_D^*(\mathbf{p},\mathbf{q},z) \left\langle \mathbf{p}|R_{nn}^{-1}(\mathbf{q})|\mathbf{p}'\right\rangle \kappa_D(\mathbf{p}',\mathbf{q},z')\big] + \left\langle z|R_{ff}^{-1}(\mathbf{q})|z'\right\rangle
\end{aligned} \tag{29}$$

and $\left\langle \mathbf{p}|R_{nn}^{-1}(\mathbf{q})|\mathbf{p}'\right\rangle$ is given by Eq. (26).

Image reconstruction is carried out by first obtaining $\delta\alpha(\mathbf{q},z)$ and $\delta D(\mathbf{q},z)$ for each $\mathbf{q}$ by Eq. (28) formulated in subspace $\mathbf{q}$. The perturbations in absorption and diffusion coefficients in real space are obtained from an inverse Fourier transform afterwards.

D. Prior information and regularization

The prior signal covariance R_{ff}, or equivalently, the penalty term L in Eq. (18), should be chosen according to the prior information. For simplicity, we will only consider the absorption inhomogeneity $\delta\alpha(\mathbf{r})$ here. If the prior signal $\delta\alpha(\mathbf{r})$ is assumed to be not correlated between different voxels in real space, corresponding to a choice of $L = I$ where I is an identity matrix, the prior signal covariance in the Fourier space is then

given by:

$$R_{\delta\alpha(\mathbf{q},z)\delta\alpha(\mathbf{q}',z')} = \delta(z-z')\int d^2\boldsymbol{\rho}\exp\left[-i(\mathbf{q}-\mathbf{q}')\cdot\boldsymbol{\rho}\right]\mathrm{Var}\left[\delta\alpha(\boldsymbol{\rho},z)\right], \quad (30)$$

analog to the derivation of the noise covariance (22). The prior signal to noise ratio in a subspace $\mathbf{q}$ is found to be

$$\mathrm{PSNR} = S^{-1}\sqrt{\frac{\int d^3\mathbf{r}\,\mathrm{Var}\left[\delta\alpha(\mathbf{r})\right]}{\int d^2\boldsymbol{\rho}\, b(\boldsymbol{\rho},\mathbf{0})}} \quad (31)$$

independent of $\mathbf{q}$ where S gives the dimensionality (the total number of values of $\mathbf{p}$) of the subspace.

This mandates a common regularization parameter to be used in all subspaces $\mathbf{q}$ from the optimal regularization criterion (21). As the magnitude of the prior signal is usually unknown, additional regularization parameter choice rules, such as the L-curve method,[26] must also be invoked. The regularization parameter in this paper is obtained by locating the L-corner of the global L-curve ($\sum_{\mathbf{q}}\|\rho(\mathbf{q})\|^2$ vs $\sum_{\mathbf{q}}\|\eta(\mathbf{q})\|^2$ where $\rho(\mathbf{q})$ and $\eta(\mathbf{q})$ are the residue of error and the size of solution respectively in the subspace $\mathbf{q}$).

The generalized Tikhonov regularization does not restrict the prior signal covariance (or the penalty term) to be an identity matrix. Some other forms of the penalty term is also commonly used, including a matrix of suitably weighted first or second order differences for a prior smooth signal[25] and spatial variant version.[27] In this paper, we will test both the identity and the first order differential penalty in image

reconstruction.

3. Results

To demonstrate our regularized solution, we perform computer simulations using a time-resolved scanning source scheme [see Fig. (1)]. Without losing generality, we will assume a uniform distribution of diffusion coefficient, i.e., $\delta D = 0$. In our simulations, the input and exit windows are divided into 21×21 grids and 20 grids along the axial direction. Each voxel has a volume of $3 \times 3 \times 1.5\text{mm}^3$. The distance between the input and exit windows of the slab is 30mm. The medium assumes a refractive index 1.38, an absorption coefficient 0.003mm^{-1} and transport mean free path 1.25mm, comparable to those found in a typical human breast.

Two absorptive inhomogeneities are located at $(14, 14, 10)$ voxel with 100% increase in absorption than that of background and at $(5, 5, 15)$ voxel with 50% increase in absorption than that of background. Poisson noise is added to the simulated photon counts. Note, the added noise is proportional to the square root of the total photon counts $\phi_0 + \phi_s$ with the absorbing objects embedded and *not* the scattered field ϕ_s. Only snapshots of photon counts at time delay of 400ps are used in the image reconstruction here as we are most interested to see the effect of modeling of noise on the quality of image reconstruction. Inclusion of different time delays is beneficial to the reconstruction.

To quantify the noise added in the simulation, we define the signal to noise ratio

(SNR) and the effective signal to noise ratio (SNR') in our simulation as

$$\begin{aligned} \mathrm{SNR(dB)} &= 10\log_{10}\frac{\sum_{\boldsymbol{\rho}_d}\sum_{\boldsymbol{\rho}_s}\|\phi_0(\boldsymbol{\rho}_d,\boldsymbol{\rho}_s)+\phi_s(\boldsymbol{\rho}_d,\boldsymbol{\rho}_s)\|^2}{\sum_{\boldsymbol{\rho}_d}\sum_{\boldsymbol{\rho}_s}\|n(\boldsymbol{\rho}_d,\boldsymbol{\rho}_s)\|^2} \\ \mathrm{SNR'(dB)} &= 10\log_{10}\frac{\sum_{\boldsymbol{\rho}_d}\sum_{\boldsymbol{\rho}_s}\|\phi_s(\boldsymbol{\rho}_d,\boldsymbol{\rho}_s)\|^2}{\sum_{\boldsymbol{\rho}_d}\sum_{\boldsymbol{\rho}_s}\|n(\boldsymbol{\rho}_d,\boldsymbol{\rho}_s)\|^2} \end{aligned} \tag{32}$$

where $\phi_0(\boldsymbol{\rho}_d,\boldsymbol{\rho}_s)$ is the noiseless observation at ρ_d from a point source at $\boldsymbol{\rho}_s$ in the uniform background and $\phi_s(\boldsymbol{\rho}_d,\boldsymbol{\rho}_s)$ is the perturbation of this observation due to the existence of the inhomogeneities. Our simulation is performed with SNR = 80dB, and an effective SNR$'$ = 4.4dB. This noise is significant as the total amount of the scattered field is less than that of noise. One sample profile is given in Fig. (2) to show the degree to which the scattered field ϕ_s is affected by the added Poisson noise.

The reconstruction result using the standard Tikhonov regularization is shown in the following figures. Fig. (3) gives the L-curve (the residue of error $\|\rho\|^2 = \|A\mathbf{x}-\mathbf{b}\|^2$ vs the size of solution $\|\eta\|^2 = \|\mathbf{x}\|^2$). The L corner suggests an optimal regularization parameter to be about 0.2. This turns out to agree with the inverse of the prior signal to noise ratio $\mathrm{PSNR}^{-1} = 0.2$ calculated using Eq. (31). The reconstruction result using this regularization parameter $\lambda = 0.2$ is given in Fig. (4). The two inhomogeneities at $(14, 14, 10)$ and $(5, 5, 15)$ are resolved with a correct central position and minimal blurring over the transversal direction. Their axial position, however, is not resolved as well as in the transversal direction. The axial central position of the first inhomogeneity $(14, 14, 10)$ is resolved to be on the right layer while the second one $(5, 5, 15)$ peaks on the layer 17 rather than the right one (layer 15). Both resolved in-

homogeneities expand considerably over the axial direction. As a result, the resolved absorption coefficients are only a fraction of the input values (100% and 50% are expected for the first and second inhomogeneities respectively).

The reconstruction result for the same data using the generalized Tikhonov regularization with an identity penalty ($L = I$) is shown in the following figures. Fig. (5) gives the L-curve (the residue of error $\|\rho\|^2 = (A\mathbf{x} - \mathbf{b})^* V^{-1}(A\mathbf{x} - \mathbf{b})$ vs the size of solution $\|\eta\|^2 = \|\mathbf{x}\|^2$). The optimal regularization parameter suggested by the L corner agrees with PSNR^{-1} again, both pointing to $\lambda = 0.2$. The reconstruction result using this optimal regularization parameter is given in Fig. (6). Comparing to the reconstruction given by the standard Tikhonov regularization in Fig. (4), noticeable improvement is observed in the resolution of the axial position of the second inhomogeneity which peaks now around layers 16 and 17. closer to the right value (layer 15). The ratio between the resolved absorption coefficients of the two inhomogeneities is also closer to that of the input values.

A second generalized Tikhonov reconstruction is performed with a first order differential operator penalty on the same data. Fig. (7) gives the L-curve (the residue of error $\|\rho\|^2 = (A\mathbf{x} - \mathbf{b})^* V^{-1}(A\mathbf{x} - \mathbf{b})$ vs the size of solution $\|\eta\|^2 = \|L\mathbf{x}\|^2$). This L-curve is not as well formed as the previous two other L-curves given in Figs. (3) and (5). The regularization parameter $\lambda = 0.2$ is shown on the L-curve figure which is now to the left of the L-corner. The reconstruction result using the regularization parameter $\lambda = 0.2$ is given in Fig. (8). The axial position of the two inhomogeneities is now correctly resolved. Narrower axial profiles are observed for both inhomogeneities (widths at half peak of 8 layers for both inhomogeneities compared to a width of

half peak of 12 layers for the first inhomogeneity and a half width of peak of 7 layers for the second inhomogeneity using the generalized Tikhonov regularization with an identity penalty). In addition, the resolved absorption coefficients are more closer to the input values (peak values of 0.115 and 0.108 are obtained for the two inhomogeneities respectively).

A "better" reconstruction can be obtained by using an aggressive regularization parameter $\lambda = 0.02$ at the expense of a degraded smoothness of the reconstruction [see Fig. (9)]. In addition to the correct resolution of the lateral and axial position of both inhomogeneities, the resolved absorption coefficients over that of the background $\delta\alpha/\alpha_0$ now approach 0.31 and 0.19 for the first and second inhomogeneities respectively, the best among all the reconstructions. These resolved peak values correspond to 31% and 38% of the input values respectively.

4. Discussion

Our results of computer simulation of reconstruction inside a planar geometry demonstrated the importance of modeling correctly the noise presented in measurements. With a proper modeling of the Poisson noise and an appropriate regularization, a better axial localization and optical property reconstruction is obtained in our simulation with realistic noise added.

The performance of the standard Tikhonov regularization is not as good as the generalized version but not so bad in the diffraction tomography thanks to the special form of the noise covariance $R_{nn}(\mathbf{q})$ in a subspace $\mathbf{q}$. The most significant elements of the noise covariance $R_{nn}(\mathbf{q})$ given in Eq. (24) is along the diagonal and of the same

value. The Fourier transform of the observation data in a diffraction tomography in effect whitens the noise. This hence allows an approximation of the noise covariance in the form of an identity matrix, which happens to be used by the standard Tikhonov regularization. Optical imaging using diffuse photons, in general, needs to consider the noise explicitly.

The appropriate regularization for an inverse problem is an art rather than science.[28] The linkage between the optimal regularization parameter and the prior signal to noise ratio (PSNR) may provide valuable guidance in the choice of the regularization parameters. The fact that the optimal regularization parameter is proportional to the noise magnitude and inverse proportional to the prior signal is consistent with intuitions. Even in the absence of known prior signal which is usually the case, this linkage helps to choose the optimal regularization parameter. In our computer simulation, all the regularization parameters in different subspace $\mathbf{q}$ are set to the same value according to this criterion. We have also observed that a first order differential penalty performs better than an identity penalty in the generalized Tikhonov regularization method for optical image reconstruction using diffuse photons.

The explicit inversion formula developed in this paper is different from that proposed by Markel and Schotland.[16] We formed our inversion formula based on a generalized Tikhonov regularization formula (19). We reduced the image reconstruction to a series of one dimensional inverse problem of the dimension of the number of discrete divisions in the axial direction, compared to a series of two dimensional inversion of a plane with a fixed axial location used in Ref. 16. The number of operations required increases only linearly with the total number of detector-source pairs in our

formulation and can be easily extended to use the cumulant approximation of photon migration in turbid media.[6,7] Another strength is the flexibility in choosing a suitable penalty term. We also want to point out that the inversion formula in Ref. 16 can be enhanced to include the noise and prior information terms using the best linear estimator given in Eq. (16), which will be studied later.

In summary, an explicit regularized inversion formula for a three-dimensional diffraction tomographic imaging using diffuse photons is derived. This approach incorporates both the prior information and the noise explicitly using a generalized Tikhonov regularization scheme in which the optimal regularization parameter links directly to the prior signal to noise ratio. Proper modeling of noise and appropriate regularization is shown to improve the quality of image reconstruction of the optical diffraction tomography.

This work is partly supported by US Army Medical Research and Materiels Command, NASA IRA, DOE Center for Laser Imaging and Cancer Diagnostics, and CUNY organized research programs. One of the authors (M. Xu) thanks the support by the Department of Army (Grant# DAMD17-02-1-0516).

References

1. R. R. Alfano, S. G. Demos, and S. K. Gayen, "Advances in optical imaging of biomedical media," Ann. N. Y. Acad. Sci. **820**. 248–271 (1997).
2. in *Diffusing photons in turbid media*, A. G. Yodh, B. Tromberg, E. Sevick-Muraca, and D. Pine, eds., (OSA, 1997), pp. 136–342, a special issue of J. Opt. Soc. Am. A. Vol. 14.

3. S. R. Arridge and J. C. Hebden, "Optical imaging in medicine: II. Modelling and reconstruction," Phys. Med. Biol. **42,** 841–853 (1997).

4. S. Chandrasekhar, *Radiation transfer* (Oxford, 1950).

5. A. Ishimaru, *Wave propagation and scattering in random media* (Academic, New York, 1978), Vol. Volume I and II.

6. W. Cai, M. Lax, and R. R. Alfano, "Analytical solution of the elastic Boltzmann transport equation in an infinite uniform medium using cumulant expansion," J. Phys. Chem. B **104,** 3996–4000 (2000).

7. M. Xu, W. Cai, M. Lax, and R. R. Alfano, "A photon transport forward model for imaging in turbid media," Opt. Lett. **26,** 1066–1068 (2001).

8. E. Wolf, "Three-dimensional structure determination of semi-transparent objects from holographic data," Opt. Commun. **1,** 153–6 (1969).

9. E. Wolf, "Determination of the Amplitude and the Phase of Scattered Fields by Holography," J. Opt. Soc. Am. **60,** 18–20 (1970).

10. A. J. Devaney, "A filtered backpropagation algorithm for diffraction tomography," Ultrsonic Imaging **4,** 336–350 (1982).

11. A. C. Kak and M. Slaney, *Principles of computerized tomographic imaging* (IEEE Press, 1988).

12. X. Pan, "Unified reconstruction theory for diffraction tomography, with consideration of noise control," J. Opt. Soc. Am. A **15,** 2312–2326 (1998).

13. C. L. Matson, "A diffraction tomographic model of the forward problem using diffuse photon density waves," Opt. Exp. **1,** 6–11 (1997).

14. X. D. Li, T. Durduran, and A. G. Yodh, "Diffraction tomography for biomedical imaging with diffuse-photon density waves," Opt. Lett. **22,** 573–575 (1997).

15. M. Xu, M. Lax, and R. R. Alfano, "Time-resolved Fourier optical diffuse tomography," J. Opt. Soc. Am. A **18,** 1535–1542 (2001).

16. V. A. Markel and J. C. Schotland, "Inverse scattering for the diffusion equation with general boundary conditions," Phys. Rev. E **64,** 035601 (2001).

17. J. C. Schotland and V. A. Markel, "Inverse scattering with diffusing waves," J. Opt. Soc. Am. A **18,** 2767–2777 (2001).

18. V. A. Morozov, *Methods for solving incorrectly posed problems* (Springer-Verlag, New York, 1984).

19. *Ill-posed problems in the natural sciences*, A. N. Tikhonov and A. V. Goncharsky, eds., (MIR, Moscow, 1987).

20. M. Vauhkonen, D. Vadász, P. A. Karjalainen, E. Somersalo, and J. P. Kaipio, "Tikhonov regularization and prior information in electrical impedance tomography," IEEE Trans. Med. Imag. **17,** 285–293 (1998), an intuitive paper, nice written.

21. in *Mathematical aspects of computerized tomography*, G. T. Herman and F. Natterer, eds., (Springer, 1980).

22. A. V. Balakrishnan, *Applied functional analysis* (Springer-Verlag, New York, 1976).

23. E. D. Micheli and G. A. Viano, "Probabilistic regularization in inverse optical imaging," J. Opt. Soc. Am. A **17,** 1942–1951 (2000).

24. E. Kalman, Rudolph, "A new approach to linear filtering and prediction problems," Transactions of the ASME–Journal of Basic Engineering **82,** 35–45 (1960).

25. M. Hanke and P. Hansen, "Regularization methods for large-scale problems," Surveys on Mathematics for Industry **3,** 253–315 (1993).

26. P. Hansen and D. O'Leary, "The use of the L-curve in the regularization of discrete ill-posed problems," SIAM J. Sci. Comput. **14,** 1487–503 (1993).

27. B. W. Pogue, T. O. McBride, J. Prewitt, U. L. Österberg, and K. D. Paulsen, "Spatially variant regularization improves diffuse optical tomography," Appl. Opt. **38,** 2950–2961 (1999).

28. J. M. Varah, "Pitfalls in the numerical solution of linear ill-posed problems," SIAM J. Sci. Stat. Comput. **4,** 164–176 (1983).

List of Figures

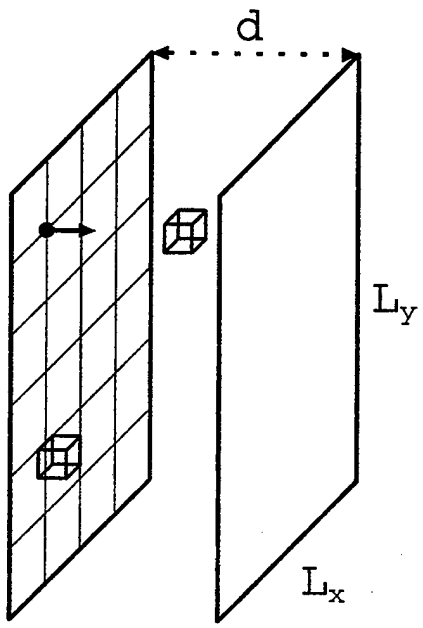

Figure 1. M. Xu et. al.

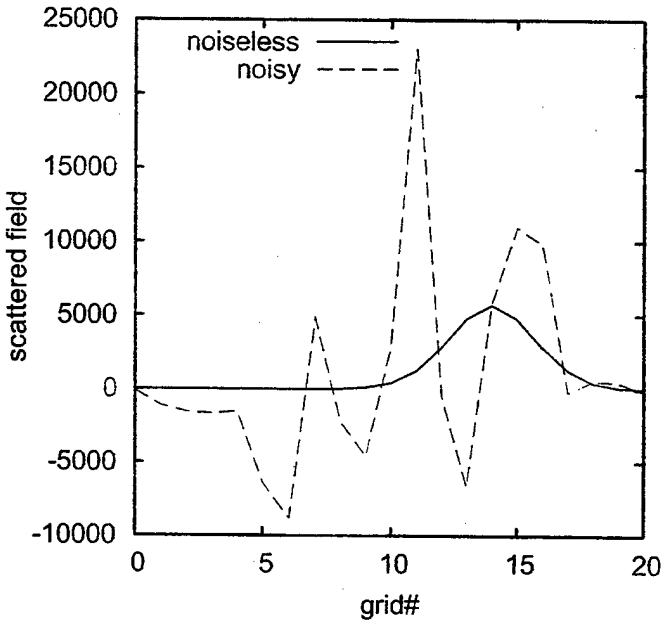

(a)

Figure 2. M. Xu et. al.

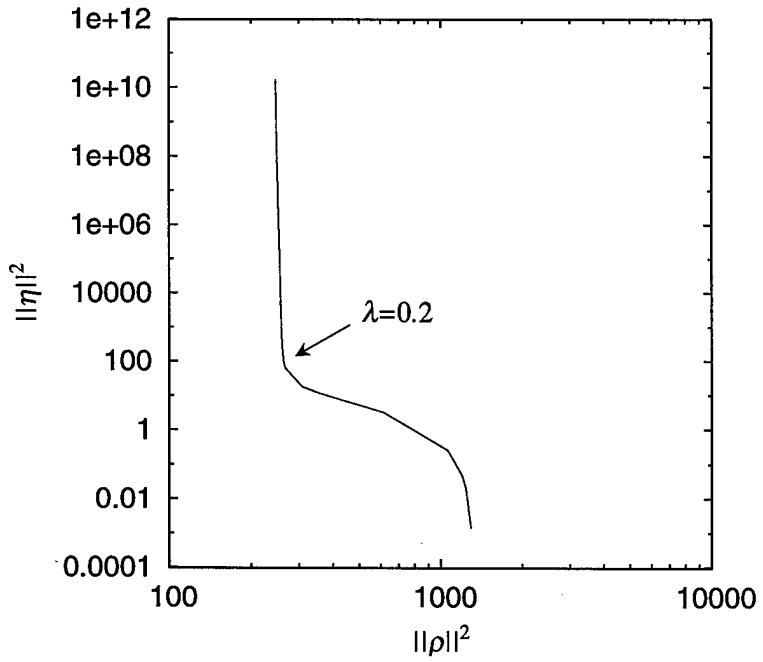

Figure 3. M. Xu et. al.

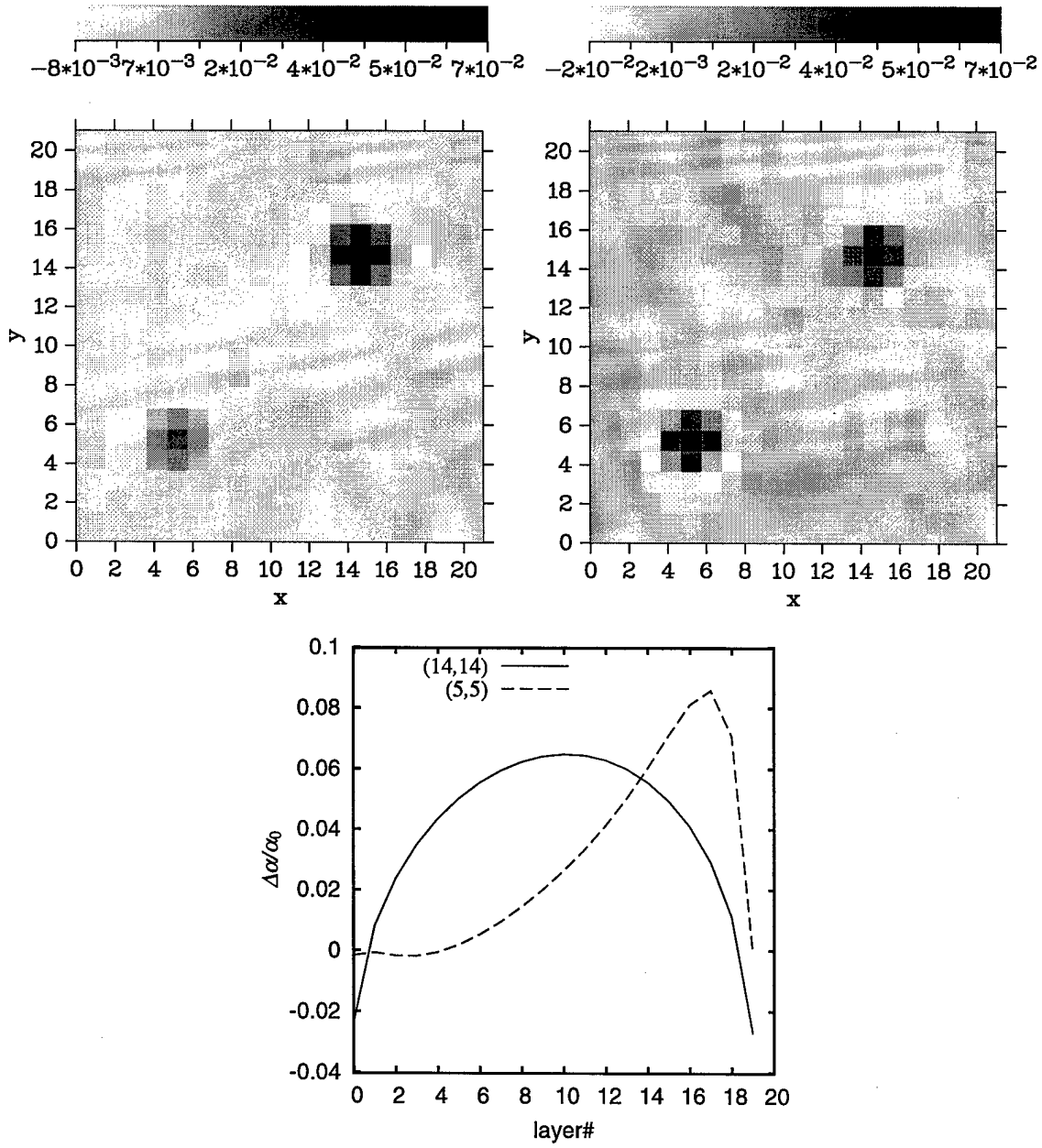

Figure 4. M. Xu et. al.

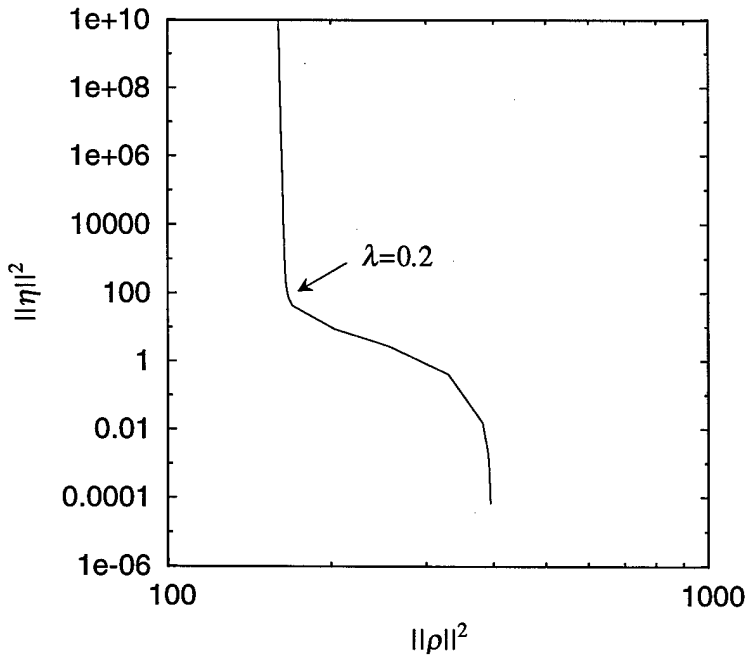

Figure 5. M. Xu et. al.

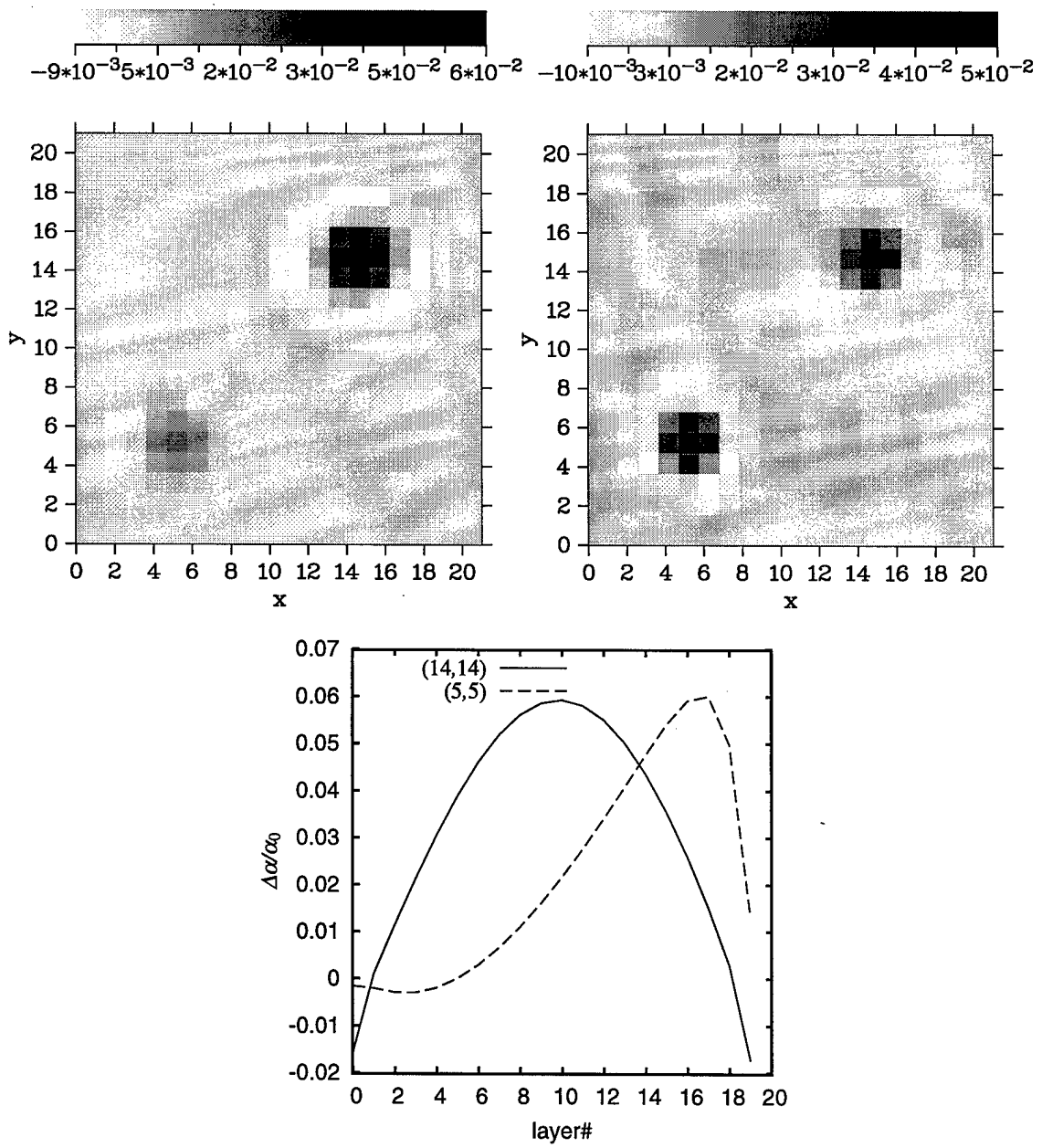

Figure 6. M. Xu et. al.

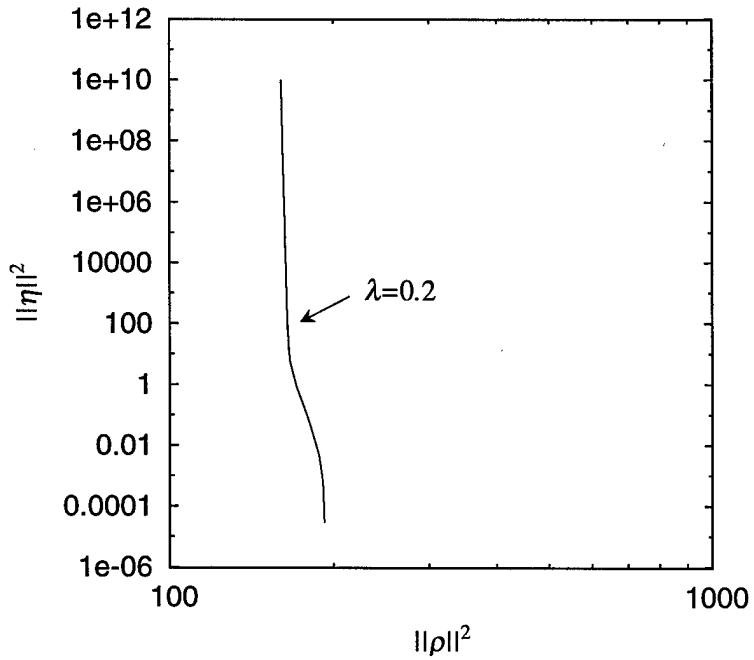

Figure 7. M. Xu et. al.

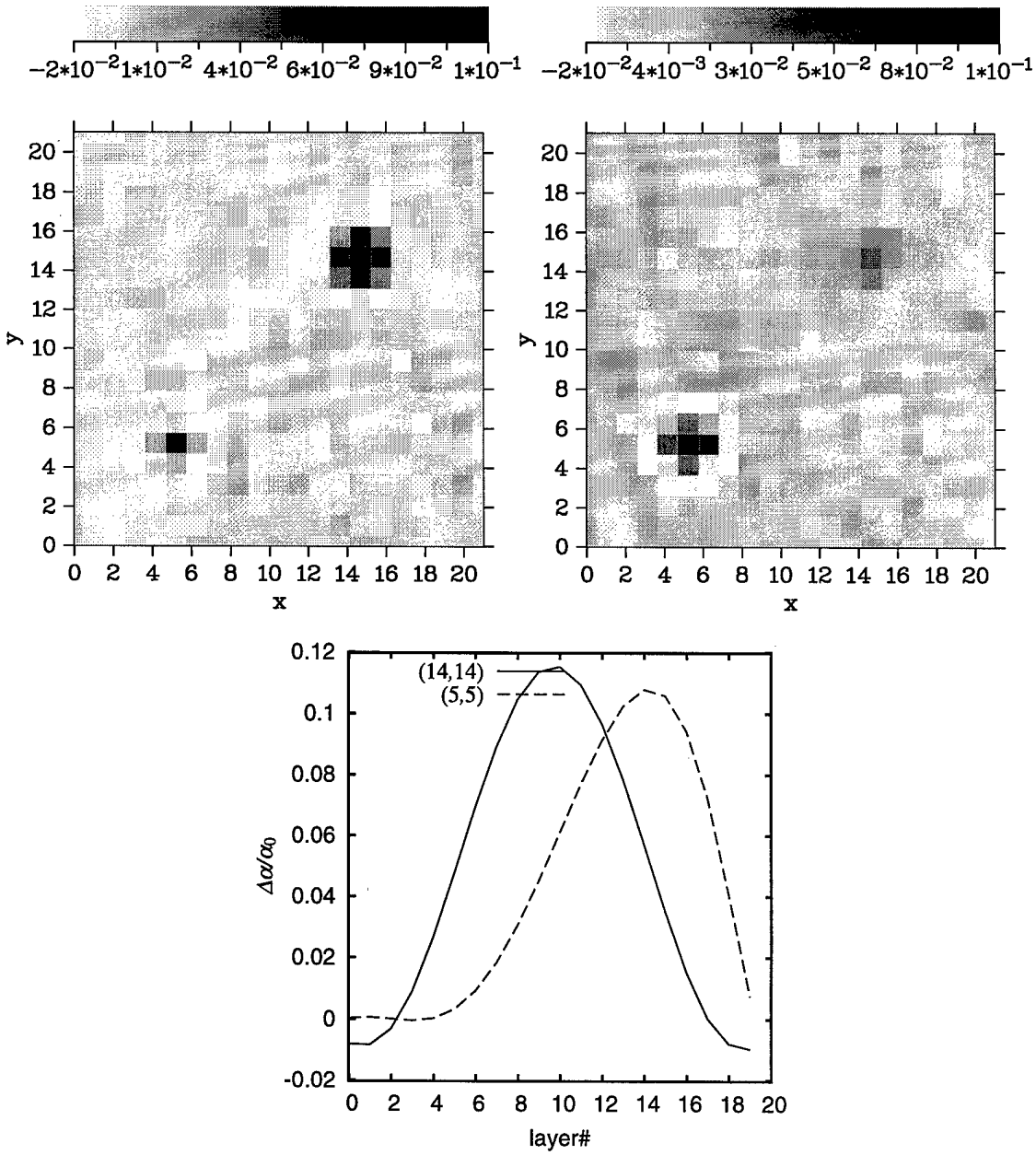

Figure 8. M. Xu et. al.

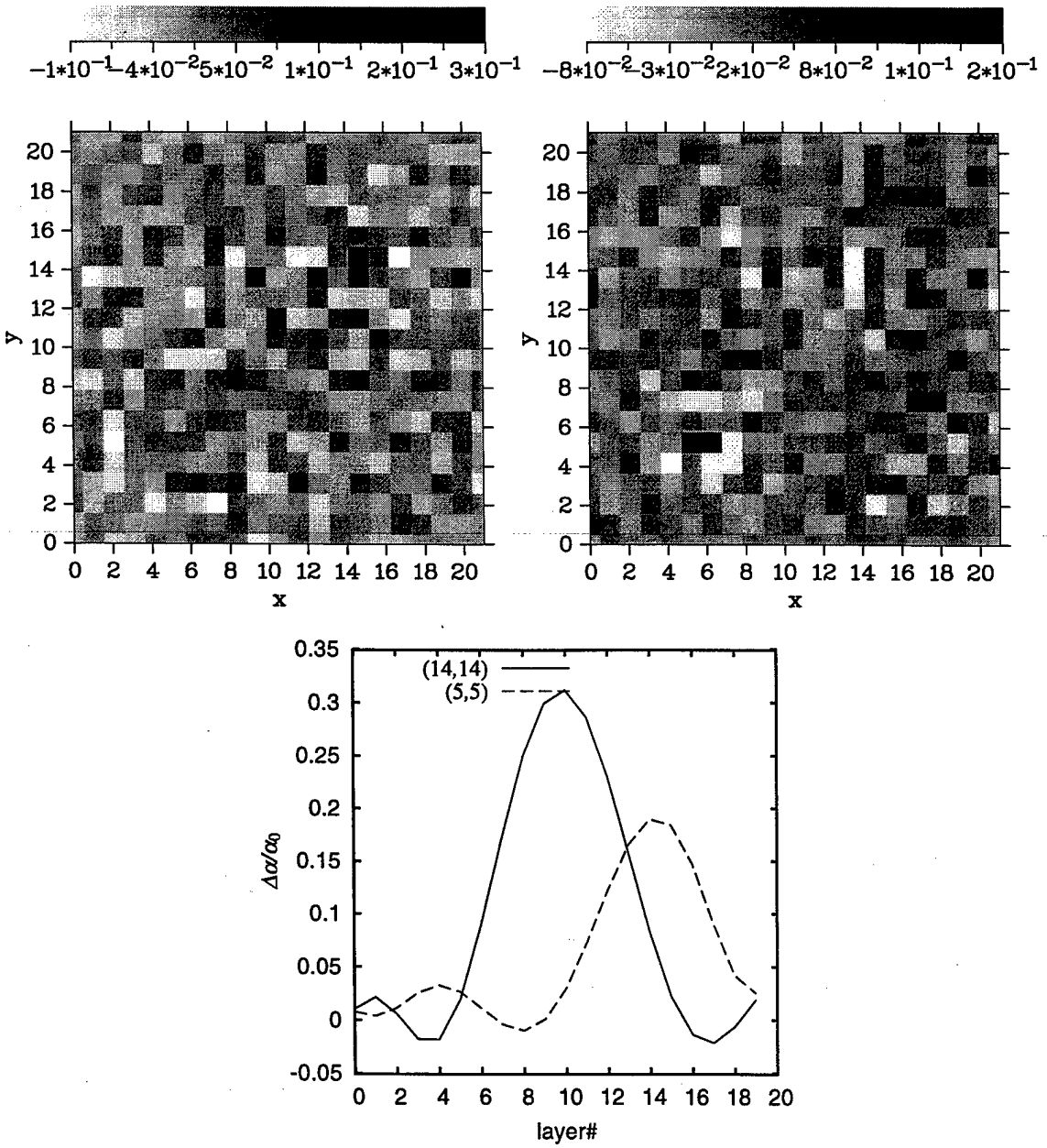

Figure 9. M. Xu et. al.